

GRAIN-GROWTH MECHANISMS
IN RAPIDLY SOLIDIFIED MATRIX STEELS

by

CHEN-YIH HSU

NATIONAL TAIPEI INSTITUTE OF TECHNOLOGY
(1972)

M.S., NEW MEXICO INSTITUTE OF MINING AND TECHNOLOGY
(1980)

SUBMITTED TO
THE DEPARTMENT OF MATERIALS SCIENCE AND ENGINEERING
IN PARTIAL FULFILLMENT OF THE REQUIREMENTS
FOR THE DEGREE OF

DOCTOR OF PHILOSOPHY

at the

MASSACHUSETTS INSTITUTE OF TECHNOLOGY

February 1984

© Massachusetts Institute of Technology, 1984

Signature of Author _____ **Signature redacted**

Department of Materials Science and Engineering
January 13, 1984

Certified by _____ **Signature redacted**
Professor Morris Cohen

Certified by _____ **Signature redacted**
Thesis Supervisor

Certified by _____ **Signature redacted**
Dr. Gregory B. Olson

Accepted by _____ **Signature redacted**
Professor Bernhardt J. Wuensch
Chairman, Department Committee

Archives
MASSACHUSETTS INSTITUTE
OF TECHNOLOGY

MAR 21 1984

LIBRARIES

GRAIN-GROWTH MECHANISMS IN
RAPIDLY SOLIDIFIED MATRIX STEELS

by

CHEN-YIH HSU

Submitted to the Department of Materials Science and Engineering on January 13, 1984, in partial fulfillment of the requirements for the Degree of Doctor of Philosophy in Metallurgy

ABSTRACT

M-2 and M-50 RSP matrix steels exhibit significant high-temperature grain-coarsening resistance even after carbides and simple sulfides have been dissolved. Isothermal grain-growth behavior suggests that particle-controlled grain growth prevails in these steels. High-resolution scanning transmission electron microscopy was used to identify and quantify the precipitate particles by energy-dispersive X-ray analysis employing a thin-window X-ray detector. Sulfides, oxides, oxysulfides, silicates and oxide-sulfides were found to be responsible for grain-boundary pinning. When associated with oxides, sulfides survive beyond their own dissolution temperature in austenite. Mg-bearing silicates were only found in the RSP M-2 matrix steel and probably resulted from the interaction between the melt and refractories during the atomizing process. A new grain-boundary pinning model which accounts for the observed grain-growth behavior in steels has been developed via modification of the previous approaches of Gladman and Hellman-Hillert. This model takes into account the distribution of particle sizes existing in the dispersion. It is confirmed that high-temperature grain-coarsening resistance in RSP steels is due to the fine dispersion of relatively insoluble second-phase particles.

The mechanical properties of both RSP matrix steels have been examined and compared with conventional matrix steels. The results indicate that the RSP M-2 matrix steel can be hardened at a higher-than-usual temperature (1140°C) to achieve higher hardness without detriment to the K_{IC} and CVN fracture toughness levels. For a given hardness, the CVN blunt-notch fracture toughness in both M-2 and M-50

RSP matrix steels is appreciably higher than in the conventional matrix steels, while the sharp-crack K_{IC} fracture toughness is not materially affected, consistent with the finer-grain structure. Lack of full density and defects associated with imperfect consolidation of the RSP powders may detract from the potential of improved mechanical behavior which may otherwise be attainable by RSP.

Thesis Supervisor: Dr. Morris Cohen
Title: Institute Professor, Emeritus

Thesis Supervisor: Dr. Gregory B. Olson
Title: Principal Research Associate

TABLE OF CONTENTS

	<u>Page</u>
Abstract	2
Table of Contents	4
List of Tables	6
List of Figures	7
Acknowledgements	10
1. INTRODUCTION.....	11
2. BACKGROUND AND LITERATURE SURVEY.....	13
2.1 Matrix Steels.....	13
2.2 Rapid Solidification Processing (RSP).....	14
2.3 Microstructure of As-Solidified RSP Steels.....	15.
2.4 Hot-Consolidated RSP Steels	16
2.5 Grain-Growth Inhibition By Second-Phase Particles.	17
2.6 Particle Coarsening and Phase Stability in γ -Fe..	24
2.7 Isothermal Grain Growth.....	26
2.8 Effect of Austenitizing Temperature on High-Strength Steels.....	27
3. MATERIALS AND EXPERIMENTAL PROCEDURES	29
3.1 Materials Processing	29
3.2 Heat Treatment	30
3.3 Metallography and Grain-Size Measurement	30
3.4 Determination of Volume Fraction of the Dispersed Phases.....	31
3.5 Identification of the Dispersed Phases	32
3.6 Hardness and CVN Tests	32
3.7 Plane-Strain Fracture Toughness Measurements....	33

	<u>Page</u>
4. RESULTS AND DISCUSSION	34
4.1 Second-Phase Dispersions.....	34
4.1.1 Size-Distribution of Second-Phase Particles.....	34
4.1.2 Identification of the Dispersed Phases.....	35
4.1.3 Volume Fraction of Second-Phase Dispersions.....	39
4.1.4 Morphology of Second-Phase Particles.....	40
4.2 Grain-Growth Characteristics.....	42
4.2.1 Isothermal Grain-Growth Characteristics.....	42
4.2.2 Prior Powder-Particle Boundaries.....	43
4.2.3 High-Temperature Grain-Coarsening Resistance.....	44
4.2.4 M-2 vs. M-50 Conventional Matrix Steels.....	47
4.3 Relation of Second-Phase Dispersions to Grain-Growth Characteristics.....	49
4.3.1 Relation of \bar{D} vs. \bar{d} / f_v	49
4.3.2 Grain-Boundary Pinning Theory.....	50
4.4 Mechanical Behavior.....	57
5. CONCLUSIONS.....	61
6. REFERENCES.....	63
Results of Tables.....	68
Results of Figures.....	80
7. SUGGESTIONS FOR FUTURE WORK.....	136
BIOGRAPHICAL NOTE.....	138

LIST OF TABLES

	<u>Page</u>
1. Chemical Composition of Steels Investigated (wt %).	68
2. Extrusion Data for RSP Powders.	69
3. Secondary Dendritic Arm Spacing of RSP Powders.	70
4. Dispersed Phases in RSP M-2 Matrix Steel After One-Hour Austenitizing at Indicated Temperatures. (STEM Analysis)	71
5. Dispersed Phases in Conventional (VAR) M-2 Matrix Steel After One-Hour Austenitizing at Indicated Temperatures. (STEM and SEM Analysis)	72
6. Dispersed Phases in RSP M-50 Matrix Steel After One-Hour Austenitizing at Indicated Temperatures. (STEM Analysis)	73
7. Dispersed Phases in Conventional (VAR) M-50 Matrix Steel After One-Hour Austenitizing at Indicated Temperatures. (STEM and SEM Analysis)	74
8. Comparison of Variables Considered in Existing Grain-Boundary Pinning Models.	75
9. Comparison of Measured and Calculated Austenitic Grain Size in RSP M-2 Matrix Steel; Equations (34) and (35).	76
10. Comparison of Measured and Calculated Austenitic Grain Size in RSP M-50 Matrix Steel; Equations (34) and (35).	77
11. K_{IC} Sharp-Crack Fracture Toughness of M-2 Matrix Steel.	78
12. K_{IC} Sharp-Crack Fracture Toughness of M-50 Matrix Steel.	79

LIST OF FIGURES

	<u>Page</u>
1. Optical Micrograph of As-Solidified RSP M-2 Matrix Steel Powders and SEM Electron Micrograph of AS-Solidified RSP M-50 Matrix Steel Powder.	80
2. Optical Micrograph of Hot-Consolidated RSP Matrix Steels (a) RSP M-2 Matrix Steel, (b) RSP M-50 Matrix Steel.	81
3. Geometry and Dimensions of Three-Point-Bend Fracture Toughness Specimen.	82
4. Typical Load-Displacement Curve for Hardened-and-Tempered M-2 and M-50 Matrix Steels.	83
5. Optical Micrograph of M-2 Matrix Steel, (a) VAR, 1180°C/1hr., (b) RSP, 1180°C/1hr., (c) VAR, 1220°C/1hr., (d) RSP, 1220°C/1hr.	84
6. Particle-Size Distribution of Second-Phase Precipitates in RSP M-2 Matrix Steel, Austenitized at 1180°C for One Hour.	86
7. Particle-Size Distribution of Second-Phase Precipitates in RSP M-2 Matrix Steel, Austenitized at 1220°C for One Hour.	87
8. Particle-Size Distribution of Second-Phase Precipitates in RSP M-2 Matrix Steel, Austenitized at 1260°C for One Hour.	88
9. Particle-Size Distribution of Second-Phase Precipitates in Conventional M-2 Matrix Steel, Austenitized at 1180°C for One Hour.	89
10. Particle-Size Distribution of Second-Phase Precipitates in Conventional M-2 Matrix steel, Austenitized at 1220°C for One Hour.	90
11. Particle-Size Distribution of Second-Phase Precipitates in Conventional M-2 Matrix Steel, Austenitized at 1260°C for One Hour.	91
12. Optical Micrograph of M-50 Matrix Steel, (a) VAR, 1180°C/1hr., (b) RSP, 1180°C/1hr., (c) VAR, 1220°C/1hr., (d) RSP, 1220°C/1hr.	92
13. Particle-Size Distribution of Second-Phase Precipitates in RSP M-50 Matrix Steel, Austenitized at 1180°C for One Hour.	94
14. Particle-Size Distribution of Second-Phase Precipitates in RSP M-50 Matrix Steel, Austenitized at 1220°C for One Hour.	95
15. Particle-Size Distribution of Second-Phase Precipitates in RSP M-50 Matrix Steel, Austenitized at 1260°C for One Hour.	96

	<u>Page</u>
16. Particle-Size Distribution of Second-Phase Precipitates in Conventional M-50 Matrix steel, Austenitized at 1180°C for One Hour.	97
17. Particle-Size Distribution of Second-Phase Precipitates in Conventional M-50 Matrix Steel, Austenitized at 1220°C for One Hour.	98
18. Particle-Size Distribution of Second-Phase Precipitates in Conventional M-50 Matrix Steel, Austenitized at 1260°C for One Hour.	99
19. EDAX Spectrum of (a) MnS, (b) VS, (c) SiO ₂ , (d) MgO-SiO ₂ .	100
20. EDAX Spectrum of (a) Al ₂ O ₃ , (b) Aluminum Oxysulfide, (c) Al ₂ O ₃ -SiO ₂ , (d) MnS-Al ₂ O ₃ , and (e) ² VS-Al ₂ O ₃ .	102
21. Volume Fraction of Dispersed Phase in RSP M-2 Matrix Steel as a Function of Austenitizing Temperature (1hr. treatment).	105
22. Volume Fraction / Particle-Size Distribution in RSP M-2 Matrix Steel, Austenitized (a) at 1180°C for One Hour, (b) at 1220°C for One Hour, (c) at 1260°C for One Hour.	106
23. Volume Fraction of Dispersed Phases in RSP M-50 Matrix Steel as a Function of Austenitizing Temperature (1hr. treatment)	109
24. Volume Fraction / Particle-Size Distribution in RSP M-50 Matrix Steel, Austenitized (a) 1180°C for One Hour, (b) at 1220°C for One Hour, (c) at 1260°C for One Hour.	110
25. Electron Micrograph of the RSP M-2 Matrix Steel, (a) TEM, 1220°C/1hr., (b) SEM, 1100°C/15min.	113
26. TEM Electron Micrograph of the RSP M-50 Matrix Steel, Austenitized at 1220°C for One Hour.	114
27. Scanning Electron Micrograph of the Morphology of Vanadium-rich Coarse Carbides, (V,W,Mo,Cr) C, in the Conventional M-2 Matrix Steel, Austenitized at 1220°C for One Hour.	115
28. Scanning Electron Micrograph of the MnS Morphology in the Conventional Matrix Steels, Austenitized at 1180°C for One Hour.	116
29. Scanning Electron Micrograph of the SiO ₂ Morphology in the Conventional (VAR) Matrix Steels, Austenitized at 1260°C for One Hour.	117
30. Isothermal Grain-Growth Behavior of the RSP M-2 Matrix Steel.	118
31. Isothermal Grain-Growth Behavior of VAR M-2 Matrix Steel.	119
32. Isothermal Grain-Growth Behavior of the RSP M-50 Matrix Steel.	120
33. Isothermal Grain-Growth Behavior of VAR M-50 Matrix Steel.	121

	<u>Page</u>
34. Optical Micrograph of the Prior Powder-Particle Boundaries in the RSP M-2 Matrix Steel, Austenitized at 1100°C for 15 Minutes.	122
35. Austenitic Grain Growth of VAR and RSP M-2 Matrix Steels, Austenitized at Various Temperatures for One Hour.	123
36. Austenitic Grain Growth of the VAR and RSP M-50 Matrix Steels, Austenitized at Various Temperatures for One Hour.	124
37. Comparison of Grain-Growth Behavior Between the Conventional M-2 and M-50 Matrix Steels at Various Austenitizing Temperatures for One Hour.	125
38. Linear Relationship Between \bar{D} and \bar{d}/f_v in the RSP M-2 Matrix and M-50 Matrix Steels, Austenitized at 1180°C, 1220°C, and 1260°C for One Hour.	126
39. Relationship Between \bar{D} and \bar{d}/f_v in the VAR M-2 and M-50 Matrix Steels, Austenitized at 1180°C, 1220°C, and 1260°C for One Hour.	127
40. The Discrepancy Between The Current Grain-Boundary Pining Models and Experimental Results.	128
41. Comparison of Proposed Model and Experimental Results.	129
42. Comparison of Mechanical Properties of VAR and RSP M-2 Matrix Steels after One-Hour Austenitizing and Double Tempering at 565°C for 2 + 2 Hrs.	130
43. Comparison of Mechanical Properties of VAR and RSP M-50 Matrix Steels after One-Hour Austenitizing and Triple Tempering at 540°C for 2+2+2 Hrs.	131
44. Fractograph of the VAR M-50 Matrix Steel, Austenitized at 1100°C for One Hour and then Triple Tempered at 540°C for 2+2+2 Hours.	132
45. Fractograph of the RSP M-50 Matrix Steel (After HIPping at 1100°C/3hrs., 30Ksi), Austenitized at 1100°C for One Hour and then Triple Tempered at 540°C for 2+2+2 Hours.	133
46. K_{IC} Sharp-Crack Fracture Toughness vs. Hardness in the Tempered Martensitic Steels.	134
47. Comparison of Blunt-Notch Fracture Toughness (CVN Energy) vs. Hardness for VAR and RSP Matrix Steels.	135

ACKNOWLEDGEMENTS

I would like to express my sincere appreciation to my thesis advisors, Professor Morris Cohen and Dr. Gregory B. Olson. It was their leadership and insightful advice that guided the work to fruition. Their constant support has made my time at M.I.T. very rewarding.

Professors Merton C. Flemings and John B. Vander Sande served on my thesis committee. I am deeply indebted to them for their interest and helpful discussion concerning my research, as well as for their constructive criticism of my thesis.

Marge Meyer, as secretary, "floor mother", and friend was often the first person sought for information and counsel. Mim Rich provided considerable assistance in the laboratory and dark room. Dennis Haezebrouck kindly reviewed the thesis manuscript. Charlie Parker provided helpful comments. Special thanks to all of these people for their constant assistance and memorable friendship.

Many friends and colleagues, Tom Kelly, Ricardo Leal, Mica Grujicic, Paul Fleyshman, John J.S. Liu, Men Glenn Chu, Dyi-Chung Hu, and other graduate students have made being at M.I.T. pleasant and rewarding.

I would like to extend my gratitude to the West Palm Beach Plant of Pratt & Whitney for processing the RSP powders, to the Air Force Materials Laboratory for conducting the hot-consolidation of the RSP powders, to the Army Materials and Mechanic Research Center for performing upset hot-forging, and to the Industrial Materials Technology Inc. for conducting HIPping.

A special thank goes to Dr. A.R. Johnson of Climax Molybdenum Laboratory for providing materials and conducting chemical analysis. This research was performed under an AMAX Foundation Fellowship, for which I am particularly appreciative.

I dedicate this thesis to my delightful wife, Joyce, my parents and my in-laws; their love and support made it possible for me to earn this degree.

1. INTRODUCTION

The application of rapid solidification processing (RSP) to crystalline alloys can provide a refined microstructure and minimize the microsegregation that usually occurs during conventional solidification. Previous work has shown that RSP steels also possess remarkable resistance to grain coarsening at high austenitizing temperatures up to about 1200°C.

There are indications that an extremely fine dispersion of relatively insoluble precipitates (such as MnS) is obtained by rapid solidification, which may act to pin grain boundaries effectively at very high temperatures. Other potential grain-growth inhibitors may also play a role in RSP steels, but a complete understanding of grain-growth mechanisms in RSP steels is currently lacking. The noteworthy grain-coarsening resistance at high austenitizing temperatures prior to martensitic hardening might be used to improve the mechanical properties of high-strength steels. Therefore, this study of grain-growth mechanisms in RSP steels was undertaken.

Two matrix steels were investigated in this program : M-2 matrix (VASCO-MA) steel and M-50 matrix steel. The matrix steels are specially designed alloy steels in which the chemical compositions are derived from the matrix compositions (1-4) of high speed steels when austenitized according to industrial practice. The purpose is to achieve high strength and eliminate the fracture-initiation potential of the brittle, excess carbides. However, these carbides normally act as grain-growth inhibitors. Thus, one disadvantage of this development is that the matrix steels have to be underhardened in order to leave some of the carbides out of solution to avoid excessive grain growth. In the present investigation, the steels

were rapidly solidified and consolidated into appropriate bar stock.

The main objective of the study is to obtain a more complete understanding of grain-growth mechanisms during the high-austenitizing treatment of RSP steels. This may lead to an alternative approach to alloy design by controlling precipitates and grain size based on RSP. Attention was directed to the effects of any potential grain-coarsening inhibitors when the excess carbides are completely dissolved and their grain-boundary pinning effect is lost. The scanning transmission electron microscope (STEM) equipped with a thin-window X-ray detector was used to identify and quantify the undissolved dispersed phases. Quantitative relationships between grain size and the dispersed phases were examined and compared with theoretical models. These models fail to give a satisfactory estimation of the grain growth inhibition in RSP steels and thus a new grain-boundary pinning model is proposed.

Some promising benefits of RSP have been demonstrated for improving mechanical properties, corrosion resistance and other properties of alloys. Both matrix steels were used as prototype materials to explore the potential of improved mechanical properties through rapid solidification processing.

2. BACKGROUND AND LITERATURE SURVEY

2.1 Matrix Steels

The physical metallurgy of high-speed and other tool steels has been described by Roberts, Hamaker and Johnson (5). High-speed steels are usually hardened at high temperatures from 1150°C to 1230°C. During austenitizing treatment, primary carbides dissolve in the matrix enriching it with alloy elements essential for secondary hardening on subsequent tempering. The microstructure of as-quenched high-speed steels consists of untempered martensite, retained austenite, and primary carbides, plus a minor amount of proeutectoid carbides which may precipitate during cooling. Immediately after quenching, high-speed steels are invariably double or multiple tempered in the temperature range of 520-620°C to undergo secondary hardening.

The M-2 matrix steel (commercial VASCO-MA) derives its chemical composition from the matrix composition of hardened M-2, which was determined by Kayser and Cohen (1). The commercial hardening temperature for M-2 matrix steel is 1105-1120°C, much lower than the hardening temperatures used for M-2, 1205-1230°C. The fracture toughness of M-2 matrix steel has been investigated (6,7), but no systematic study of grain growth has been conducted on this steel.

Rescalvo and Averbach (4) determined the fracture toughness of AISI M-50 high-speed steels. The composition of the martensite was determined (for the optimum hardening temperature) corresponding to the composition of the M-50 matrix steel examined here. This is a newly designed alloy

steel. Its mechanical properties and grain-growth characteristics were examined for the first time in this program.

2.2 Rapid Solidification Processing (RSP)

Rapid solidification of crystalline alloys has received considerable attention during recent years (8-10). Several rapid solidification processes have been developed. Melt spinning and self-quenching techniques can provide RSP products in thin-layer form. Gas atomization and centrifugal atomization can generate powders from small droplets, and so require later consolidation for producing bulk shapes. The most common methods of consolidation of RSP powders are hot isostatic pressing, hot extrusion, and hot isothermal forging.

The microstructural characteristics of RSP crystalline alloys are summarized (11-17) as follows :

- (a) Extension of solid-state solubilities;
- (b) Formation of metastable phases;
- (c) Microstructural refinement;
- (d) Reduced microsegregation.

During hot consolidation, (a) and (b) are often eliminated and some coarsening of precipitates may occur.

The secondary dendritic arm spacing of as-solidified metals shows a close relation to the cooling rate (18). The resulting potential improvement of mechanical properties and material performance is of

great interest. Inclusions such as sulfides, oxides, carbides, or nitrides in steels normally have a deleterious effect on fracture toughness and fatigue strength. However, RSP can produce a fine dispersion of such particles to a point where they are less harmful to mechanical properties and may, indeed, be beneficial.

2.3 Microstructure of As-Solidified RSP Steels

Kelly et al. (19) used STEM to investigate the microstructure of RSP austenitic stainless steel powders. No large ($>0.2\ \mu\text{m}$) precipitates were formed. Smaller ($100\text{--}500\ \text{\AA}$) equiaxed precipitates were often observed throughout the intracellular regions of the as-solidified structure. Most of the powder particles had a non-regular cellular structure within the confines of small ($\leq 5\ \mu\text{m}$) grains. The grain structure of RSP particles was found to be dependent on the solidification mode.

Recently, the effect of cooling rate on the microstructure of as-solidified high-speed tool steels has been investigated, and will be briefly summarized here (20-24).

As the cooling rate is increased to the rapid solidification range, the austenite and eventually ferrite become increasingly stabilized. At a cooling rate of $10^8\ \text{Ks}^{-1}$, the structure is almost entirely ferrite. At $10^6\text{--}10^7\ \text{Ks}^{-1}$, ferritic regions are retained to room temperature, but are surrounded by austenite and carbides. At $10^5\ \text{Ks}^{-1}$, the microstructure contains austenite with possibly some martensite. At $10^3\ \text{Ks}^{-1}$, martensite predominates with a few regions of retained austenite and a

large quantity of carbides. For RSP T-1 steel (nominally 18W-4Cr-1V), a larger secondary hardening peak is observed on tempering at 650°C; the peak hardness is 1050 K_gmm⁻² compared to the conventional peak of 950 K_gmm⁻² after tempering at 530°C. The increase in peak hardness is probably the result of high supersaturation and/or a much finer scale of precipitation.

2.4 Hot-Consolidated RSP Steels

Goss (25) studied precipitation strengthening in RSP Mo steels with a carbon content of 0.25%. He found that RSP has little effect on the secondary hardening of these steels after hot consolidation, but they exhibited unusual austenitic grain-growth resistance even at 1200°C. The grain growth was influenced by the powder-particle size, with the smaller particles having a finer grain size when austenitized at 1200°C. These steels did not contain any of the usual grain refiners such as Al, Nb, or V. With electron microscopy, a fine dispersion of MnS particles was commonly observed throughout the RSP materials.

Suga et al. (26) studied grain-growth characteristics in hot-consolidated RSP 9Ni-4Co steels with carbon levels from 0.2% to 0.8%. Similar results were found in all cases, and the grain growth behavior was not significantly influenced by carbon content. Kelly and Vander Sande (19) reported that the hot-consolidated RSP high-sulfur 303 stainless steel retained a fine grain size at 1200°C compared to conventional steels. A very uniform dispersion of small MnS precipitates (100-500Å) was noted in the RSP case, while no small precipitates (≤2000Å) were

observed in the conventionally processed steels. Fleishman (27) also found high-temperature grain-coarsening resistance in both hot-extruded and hot-pressed RSP 9Ni-4Co-0.2C steels.

Thus far, the indications are that a fine dispersion of MnS particles is obtained during rapid solidification processing. Because of their relative insolubility, these particles may pin austenitic grain boundaries effectively at high temperatures. Nevertheless, a detailed understanding of the grain-coarsening resistance in RSP steels is still lacking.

2.5 Grain-Growth Inhibition by Second-Phase Particles

In polycrystalline metals, grain-boundary migration can occur at high temperatures even without stored strain energy or chemical driving force. The driving force is provided by the overall reduction of grain-boundary energy. The grain-boundary migration rate is generally regarded as proportional to the driving force and the boundary mobility. It follows that any structural feature which reduces either of these parameters will reduce the rate of overall grain-boundary migration and thereby retard the grain growth.

There are two basic types of grain growth, one is "normal" grain growth (or continuous grain growth); the other is "abnormal" grain growth (discontinuous grain growth or secondary recrystallization). The grain-size distribution is relatively uniform during normal grain growth. On the other hand, there are marked differences in the grain size distribution during abnormal grain growth; grain sizes more than ten times the

average grain size are commonly observed during abnormal grain growth.

It was found that normal grain growth can be specifically inhibited by dispersed second-phase particles, by a free surface, by solute atoms, by gas bubbles or voids, and by a pronounced preferred orientation texture (28). Previous studies have indicated that high-temperature grain-coarsening resistance is due to particle-induced pinning of grain boundaries. These effects, except the first, were not significant factors in the present program.

The presence of second-phase particles can reduce the specific interfacial energy of a grain boundary and thereby reduce the overall rate of grain growth. Zener (29) showed that the restraining force of a second-phase particle in contact with an isolated grain boundary of the matrix is $\sigma \pi r \sin 2\theta$, where θ is an angle which depends on the relative position of the boundary to the particle. Hence, the maximum restraining force of a second-phase particle is $\sigma \pi r$ when $\theta = 45^\circ$. Considering particles of a uniform size, r , the net restraining effect of all second-phase particles in a unit area of the boundary is :

$$\begin{aligned} F_p &= \sigma \pi \sum r \\ &= \sigma \pi N_v r^2 = \sigma \frac{3}{4} \frac{f_v}{r} \end{aligned} \quad (1)$$

where N_v is the number of particles per unit volume.

By equilibrating the driving force (σ / R_0) and the total restraining force of pinning particle on grain boundary, he obtained a condition for inhibition of boundary movement :

$$\sigma \pi \cdot 3 f_v / 4 \pi r = \sigma / R_0 \quad (2)$$

or

$$2 R_0 = \frac{8}{3} \frac{r}{f_v} \quad (3)$$

where σ is the specific energy of the grain boundary, R_0 is the average grain radius, and f_v is the volume fraction of the particles.

Hellman and Hillert (30) developed a growth-rate equation appropriate for the presence of second-phase particles :

$$\frac{dR}{dt} = \sigma M \left(\frac{1}{R_{cr}} - \frac{1}{R} + Q \right) \quad (4)$$

Where R is the grain radius, M is the mobility of the grain boundary, the quantity σQ is the net restraining force due to the second-phase particles, and R_{cr} is closely related to the average grain radius R_0 . The Q term will always act against the movement of the boundaries. The positive sign holds for a shrinking grain, while the negative sign holds for an expanding grain. They found that Zener's treatment gave a larger equilibrium grain size than is observed. Hellman and Hillert (30) considered the effect of the macroscopic curvature and the position of grain

boundary by relating the angle θ to the position for various values of boundary radius of curvature ρ . They demonstrated by calculation that the ratio between the macroscopic curvature of the boundary and particle size, ρ/r , has a strong influence on the ability of the boundary to stay in contact with the particle. The boundary can stay in contact with a particle over a larger distance, as ρ/r increases. They pointed out that Zener's treatment might yield an increasing under-estimation of the number of particles in contact with the boundary with increasing ρ/r . They suggested that the net pinning force should be multiplied by a correction factor β , where $\beta = 0.125 \ln \left(40 \frac{\rho}{r} \right)$.

Also Hellmen-Hillert obtained an estimate for the pinning force of a distribution of particles by summing the effect of particles of discrete size classes. The restraining force, σQ , is modified based on Zener's treatment :

$$\sigma Q = \sigma \pi \sum \beta_i r_i = \sigma \pi \sum \beta_i n_i r_i^2 = \sigma \frac{3}{4} \sum \frac{\beta_i f_i}{r_i} \quad (5)$$

For a uniform particle size, r , the restraining force is :

$$\sigma Q = \sigma \frac{3}{4} \frac{\beta f_v}{r} \quad (6)$$

Hillert (31) developed a model which predicted that normal grain growth should stop at $R_0 = 1/3Q$ and the inhibited grain growth in austenite was given as :

$$2R_0 = \frac{8}{9\beta} \frac{r}{f_v} \quad (7)$$

Gladman (32,33) considered the energy change accompanying the pinning of a planar boundary by a spherical particle, and obtained the maximum rate of change of energy as follows :

$$\frac{(d \Delta E)}{(d \Delta R)_{\max}} = 3.960 \mathcal{G} r = 4 \mathcal{G} r \quad (8)$$

where ΔE is the change in interfacial energy, and ΔR is the grain-boundary displacement. During grain growth, the net reduction in grain-boundary interfacial energy, ΔE_g , per unit boundary area is :

$$\Delta E_g = \frac{\Delta R}{R_0} \left(\frac{2}{Z} - \frac{3}{2} \right) \quad (9)$$

where $Z = R/R_0$ with R the radius of the growing grain. This equation indicates that only those grains whose radius is larger than four-thirds of R_0 can grow at the expense of smaller grains. The net change in interfacial energy per particle, ΔE_p , is :

$$\Delta E_p = \Delta E_g / N_s \quad (10)$$

where N_s is the number of particles contacting the boundary per unit area of grain boundary. Gladman assumed that the effective interaction distance between the boundary and particle is $\frac{1}{2} r$ and thus $N_s = 2 r N_v$. The net change in interfacial energy per particle ΔE_p is :

$$\Delta E_p = \frac{\Delta E_g}{2 r N_v} \quad (11)$$

where r is the particle radius and N_V is the number of particles per unit volume. Using

$$f_V = \frac{4}{3} \pi r^3 N_V, \quad (12)$$

equation (11) becomes :

$$\Delta E_P = \frac{2 \sigma \pi r^2 \Delta R}{3 R_0 f_V} \left(\frac{2}{Z} - \frac{3}{2} \right) \quad (13)$$

or,

$$\frac{d\Delta E_P}{d\Delta R} = \frac{2 \sigma \pi r^2}{3 R_0 f_V} \left(\frac{2}{Z} - \frac{3}{2} \right) \quad (14)$$

A limiting grain size is obtained by equating

$$\left(\frac{d\Delta E}{d\Delta R} \right)_{\max.} = - \left(\frac{d\Delta E_P}{d\Delta R} \right) = 4 \sigma r \quad (15)$$

and then

$$2 R_0 = \frac{\pi r}{3 f_V} \left(\frac{3}{2} - \frac{2}{Z} \right) \quad (16)$$

The above-mentioned equations indicate that the grain diameter, \bar{D} , is proportional to the ratio of \bar{d}/f_V and can be expressed as :

$$\bar{D} = K \frac{\bar{d}}{f_V} \quad (17)$$

where K is a constant. Clearly, the pinning particles should be finely dispersed in order to obtain a small grain size. The validity of this theoretical treatment has been confirmed by successfully predicting the grain-coarsening temperature of aluminum- and niobium-treated steels (32,33).

Carbides can be very effective grain-growth inhibitors but tend to dissolve or readily coarsen at high temperatures (34). VN, AlN, and NbN have been observed in steels at high temperatures (32-36). Although some other potential grain-growth inhibitors were considered in the present program, the following survey focusses on the effect of MnS and SiO₂ particles on grain growth.

May and Turnbull (37,38) observed that the normal grain growth in ordinary silicon iron and in high-purity silicon iron with addition of MnS was much slower than that in high-purity silicon iron. They concluded that the inhibition of normal grain growth was caused by the dispersed MnS phase ; the resulting small grain size can provide the driving force for secondary recrystallization. Banerjee et al.(39) studied grain growth in 3.2 % Si steel with varying sulfur content. They observed a dispersed MnS impurity phase which was believed to pin grain boundaries and inhibit grain growth. Fiedler (40,41) concluded that MnS is capable of restraining grain growth and the restraining ability of inclusions is dependent on their size and distribution. The desired uniform dispersion of many small inclusions can be obtained by controlling the cooling rate from the solution

temperature of the inclusions or by drastic quenching from the solution temperature followed by heat treating at lower temperature. Howard (42) achieved a refinement of grain size upon sintering by adding fine particle silicon (ie. -200 mesh). Silica was formed during the heating to the sintering temperature. He found that only sufficiently finely dispersed SiO_2 can inhibit normal grain growth in sintered silicon iron. Flowers and Karas (43) used transmission electron microscopy to study the MnS phase dispersion and the resulting grain size in 3 % silicon iron. The sulfide particle sizes were measured as a function of annealing temperature. Sulfides coalesced as the annealing temperature increased. The average grain size was found to be a function of the average particle size.

Particle-inhibited grain growth has also been well established in nonferrous metals (44). It should also be noted that particle-inhibited grain growth may occur in alloys containing more than one type of dispersed phase, but the second-phase particles tend to coalesce and dissolve at sufficiently high temperatures. This tendency may remove the retarding effect of such inclusions on grain growth.

2.6 Particle Coarsening And Phase Stability In γ -Fe

The initial precipitates formed in RSP powders may coarsen during hot consolidation and subsequent heat treatment. This will reduce their effectiveness in retarding grain growth. Hence in order to maintain a small grain size at very high temperatures, the second-phase particles must be stable to resist coalescence as well as dissolution in the

matrix phase. The volume diffusion-controlled coarsening of precipitates in the matrix can be expressed as (45,46) :

$$\bar{r}^3 - \bar{r}_0^3 = \frac{8 D C}{9 R_g T} \sigma V_m^2 t \quad (18)$$

where \bar{r} is the mean precipitate radius at time t ,

\bar{r}_0 is the initial mean precipitate radius,

D is the diffusivity of the rate-controlling species in the matrix,

C is the solubility concentration of the rate-controlling species in the matrix,

R_g is the gas constant,

V_m is the molar volume of the precipitate phase,

T is the absolute temperature,

σ is the specific interfacial energy.

In order to maintain a small grain size at high temperatures, the initial precipitate size and the temperature-sensitive product DC should be small. For a stable second-phase particle MX , the particle coarsening is controlled by $D_X C_X$ if $D_X C_X < D_M C_M$, and by $D_M C_M$ if $D_M C_M < D_X C_X$.

The solubility product of a precipitate is a good index for evaluating its stability at a certain temperature for a given alloy composition. The solubility products of several second-phase particles relative to austenite are available in the literature(33, 47-51). Typically, the solubility product increases with increasing temperature. Promising grain-growth inhibitors are TiN , AlN , TiB_2 , ZrN and MnS . It has also been suggested that LaS and CeS possess a particularly high potential

for resisting grain growth based on thermodynamic calculations.

2.7 Isothermal Grain Growth

In a wide variety of pure metals, solid-solution alloys, and sintered ceramic compounds, the kinetics of normal grain growth can be expressed as (52-55) :

$$\bar{D} = K t^n \quad (19)$$

where \bar{D} is the average grain diameter, t is the isothermal annealing time, and K and n are parameters depending on the material and temperature. A parabolic law of grain growth ($n=0.5$) has been observed in metals of ultrapurity at high temperatures. Such a parabolic grain-growth law has been deduced by several authors (52, 56-57) with different approaches. The equation can be expressed as $\bar{D} = K t^{1/2}$, or $\bar{D}^2 - \bar{D}_0^2 = C t$, where \bar{D}_0 and \bar{D} are the average grain diameter before and after growth ; C is a rate constant. Hillert (31) has presented a theory of normal grain growth which predicts such a parabolic growth rate equation. He further treated the effect of second-phase particles on grain growth and obtained a cubic growth rate equation, that is, the average grain size in isothermal grain growth is then proportional to $t^{1/3}$. Recently, Rhine and Craig (58) studied the topological features of three-dimensional grain growth in aluminum by serial-section microscopy and reported that the tetrakaidecahedron is the average topological shape during normal grain growth of equiaxed grains. They also predicted that the average grain volume should be proportional to time and the corresponding growth rate equation should be $\bar{D} = K t^{1/3}$.

Suga et al.(26) studied grain growth characteristics in extruded RSP 9 Ni-4 Co steels after prolonged treatment. The grain growth takes place in three basic stages. At lower temperatures, there is a slow growth of equiaxed grains within the prior powder particle domains. At higher temperatures and longer times, a "necklace" or "bamboo" structure of enlarged grains develops and later a larger fairly uniform equiaxed grain structure is attained. The third stage of grain growth in the RSP material is typical abnormal grain growth. Higher austenitizing treatments induce abnormal grain growth earlier than do lower austenitizing temperatures.

2.8 Effect of Austenitizing Temperature on High-Strength Steels

Recently, considerable attention has been given to the effect of high austenitizing treatment on the mechanical properties of high-strength steels, such as 4340, 300M, and Cr-Mo steels(59-66). Experimental data have shown that K_{IC} fracture toughness is substantially increased thereby, but the Charpy impact energy and ductility are decreased. The enhancement of K_{IC} has been attributed to the dissolution of void-initiating inclusion particles, while the reductions in Charpy impact energy and ductility have been attributed to the occurrence of excessive grain growth. Fleishman(27) has examined the mechanical properties of RSP 9 Ni-4 Co-0.6 C steel and reported that an improvement of K_{IC} was obtained after high-austenitizing treatment. The increase in fracture toughness was accompanied by a change in the fracture mode from intergranular cleavage to ductile void coalescence. He also noted that the fracture toughness (K_{IC} and CVN energy) of a 4 Mo-0.25 C steel increased by 30-50 % after high-austenitizing treatment

in both conventionally processed and fully consolidated RSP steels, while the RSP steel showed a greatly reduced transition temperature associated with its finer grain size. Hence, it is expected that superior mechanical properties can be achieved in fully-consolidated RSP steels provided that a fine microstructure is maintained.

3. Materials and Experimental Procedures

3.1 Materials Processing

Both M-2 and M-50 matrix steels were vacuum arc remelted (VAR). The M-2 matrix steel (available as commercial VASCO-MA steel) was produced with an ingot diameter greater than 9" while the M-50 matrix steel (laboratory heat) was produced with a diameter of 3". Both matrix steels were supplied by the Climax Molybdenum Laboratory after reduction to plate stock. The chemical compositions of these matrix steels are shown in Table 1.

For each matrix steel, VAR ingots were conventionally processed down to 0.4 " plate via hot forging and rolling, while companion pieces were sent to the West Palm Beach Plant of Pratt and Whitney for rapid solidification processing by induction-vacuum remelting and centrifugally atomizing in high-velocity helium gas ($\sim 10^5$ K/sec cooling rate). The RSP powders were separated by size, and were blank-die compacted in mild steel sleeves and then hot extruded at the Air Force Materials Laboratory into appropriate bar stock for heat treatment, metallography and mechanical property testing. The extrusion conditions for both matrix steels are shown in Table 2. Table 1 also shows the chemical analysis of the matrix steels after rapid solidification and consolidation.

Secondary dendrite arm spacings were measured from the cross section of RSP powders. The cooling rates were estimated by extrapolating the experimental results of Maraging 300 steel(18) and are summarized in Table 3. Figure 1 shows optical and SEM electron micrographs of as-solidified

RSP matrix steel powders. Pores or voids induced by trapped inert gas were observed in RSP powders. Figure 2 illustrates residual pore defects remaining after hot extrusion(900^oC) in the RSP matrix steels. The residual pores exist in the form of irregular shapes and the pore sizes are larger than 1 μm (up to 30 μm).

3.2 Heat Treatment

In commercial practice, the M-50 steel is austenitized at 1095^oC and the M-2 matrix steel at a temperature between 1095 and 1120^oC. In this study, the specific austenitizing temperatures examined were 1100^oC, 1140^oC, 1180^oC, 1220^oC, 1260^oC, and 1300^oC for both matrix steels. For the grain growth experiments, the samples were austenitized in argon-filled quartz tubes at each temperature for one hour and then quenched in oil. Those samples were large enough to avoid the effect of free surface on grain growth. Samples for mechanical testing were tempered and then air cooled. The M-2 matrix steel was double tempered at 565^oC for 2+2 hours and the M-50 matrix steel triple tempered at 540^oC for 2+2+2 hours in order to obtain typical secondary hardening.

3.3 Metallography and Grain-Size Measurement

Optical microscopy was used to observe the general appearance of the microstructure and to measure grain size. The mounted and polished samples were etched with 2 % Nital to reveal prior austenitic grain boundaries. Grain sizes were measured by the mean linear-intercept method. The average grain diameter is given as $1.65 \frac{L}{N}$, where L is the length of the traverse and N is the number of grain-boundary intercepts. For each sample, at least 500 intercepts were counted. The grain-size distribution parameter, Z, was estimated from the ratio of the maximum to the mean linear intercept along a traverse on an optical micrograph. For each sample, the maximum linear intercepts of at least five large grains were measured and averaged. Similar Z values were obtained for longitudinal and transverse sections.

3.4 Determination of Volume Fraction of the Dispersed Phases

Thin foils for TEM and STEM examination were taken from specimens quenched from high austenitizing temperatures where the excess carbides were completely dissolved. Samples were cut with a low speed diamond saw and then thinned down to 0.004" thickness. After punching into 3 mm disks, the thinned samples were electropolished in a Fischione Twin-Jet Electropolisher with an electrolyte consisting of 8% perchloric acid (60%), 70% ethyl alcohol, 10% glycerol, and 12% distilled water. The operating condition was -20°C with a current of 45 mA. Thin foils were then examined in a Philip EM-300 Transmission Electron Microscope operated at 100 KV. For each specimen, at least 100 particles in 4 or 5 thin foils were counted. The particle-size distributions were corrected using the method proposed by Crompton et al.(67). The contribution to the projected image of truncated spherical particles with centers lying outside the foil and the effects of the ratios of foil-to-particle thickness were taken into account in the corrected particle-size distribution.

The volume fractions of the dispersed phases were estimated from the projected image of the thin foil(68). In this case the mean particle diameter, \bar{d} , is nearly equal to the foil thickness, t , hence particle image overlap is negligible. Image truncation was taken into account, estimating the volume fraction of particles as :

$$f_v = A'_A \left(\frac{2 \bar{d}}{2 \bar{d} + 3 t} \right) \quad (20)$$

where A'_A is the area fraction of particles in the projected image, and t is taken as 1500\AA which represents a reasonable approximation to the foil thickness.

3.5 Identification of Dispersed Phases

Since small particles are often embedded within the foil and large particles are not always retained in the foil, the extraction-replica technique is useful for the analysis of dispersed phases. Mounted and polished samples were slightly etched with 2 % Nital to reveal particles and then deposited with evaporated carbon to about 1000\AA thickness. The carbon-deposited samples were then deeply etched with 10 % Nital to strip the carbon replica (with particles) from the surface of the specimen. Stripped replicas were then placed on grids for particle observation. Chemical analysis of individual particles in both thin foil and extracted replica specimens were performed with a VG HB5 Scanning Transmission Electron Microscope (STEM) using energy dispersive X-ray analysis via a thin-window X-ray detector to analyze both heavy and light elements.

3.6 Hardness and CVN Tests

Hardness of the matrix steels was measured on the Rockwell-C scale. Each representative value of hardness was taken from the average value of five measurements. A Physmet CIM-128 Impact test machine with a total energy of 24 ft-lb was used to measure the Charpy impact energy on standard-sized specimens.

3.7 Plane-Strain Fracture Toughness Measurements

The fracture toughness specimens used for K_{IC} measurements were of the three-point bend type with the dimensions of the half-size Charpy V-notched bar shown in Figure 3. The specimens were tested in the longitudinal L-T direction (based on ASTM Standard E399-78a). The specimen dimensions meet ASTM specification E399-72 for all conditions studied. The minimum dimension specified for the breadth, B, is given as $2.5\left(\frac{K_{IC}}{Y.S.}\right)^2$, where Y.S. is the yield strength and K_{IC} , the fracture toughness. Fracture toughness values of the matrix steels determined in this study ranged from 20 to 45 Ksi $\sqrt{\text{in}}$ with hardness levels from 61 to 55 H_{RC} . A yield strength of 250 Ksi is estimated for a hardness of 55 H_{RC} . With a fracture toughness of 45 Ksi $\sqrt{\text{in}}$, the minimum B, $2.5\left(\frac{K_{IC}}{Y.S.}\right)^2$, is calculated as 0.08 ". Therefore, the specimen size in the study easily satisfies the requirement of ASTM Standard E399-72.

Heat-treated specimens with a Charpy V-notch were cut by a string saw using a wire of 0.005 " diameter to a depth of 0.02 ". Fatigue pre-cracking was performed on a Physmet FCM - 300 B fatigue pre-cracking machine to obtain a total crack length of about 5 mm (0.2 "). The machine was designed to shut off automatically when the crack propagated to the pre-determined depth. The plane-strain fracture-toughness test was performed in a Physmet SB-750C slow bend test machine with a speed of 0.0125 "/minute. The typical shape of the load-displacement curves for all samples is shown in Figure 4, which satisfied the requirement for a valid K_{IC} test. However, crack growth was determined from crosshead displacement rather than a specimen clip-gauge.

4. RESULTS AND DISCUSSIONS

4.1 Second-Phase Dispersions

4.1.1 Size-Distribution of Second-Phase Particles

Optical micrographs of the conventional and RSP M-2 matrix steels after one-hour austenitizing at 1180°C, 1220°C and 1260°C are shown in Figure 5. Small grains with a fine dispersion of precipitate particles were observed in the RSP steel while coarse grains with a wide distribution of particle sizes were observed in the conventional steel. Annealing twins were also observed above 1180°C in the RSP steel.

Because the size of the dispersed second-phase particles in the RSP steel is less than 1 μm , electron microscopy is necessary to monitor the particle-size distribution. The size distributions of the second-phase particles in the RSP M-2 matrix steel after one hour austenitizing above 1180°C are shown in Figures 6-8. The particle size varied from 600Å to 7000Å and the size-distribution curve moved to the right-hand direction as austenitizing temperature was increased. The apparent average particle sizes were 0.18 μm , 0.19 μm , and 0.23 μm after austenitizing at 1180°C, 1220°C, and 1260°C for one hour respectively. The corrected results show a small change in particle-size distribution and the average particle sizes become 0.19 μm , 0.20 μm and 0.24 μm after austenitizing at 1180°C, 1220°C, and 1260°C for one hour respectively. In the conventional M-2 matrix steel, the particle size varied from 0.2 μm to 10 μm . Figures 9 - 11 show the size distribution of precipitate particles after austenitizing at 1180°C, 1220°C, and 1260°C for one hour and average

particle sizes were 1.7 μm , 2.0 μm , and 2.5 μm respectively.

Optical micrographs of the conventional and RSP M-50 matrix steels after one hour austenitizing at 1180°C and 1220°C are shown in Figure 12. Again, a fine dispersion of precipitate particles in a matrix of small grains was observed in the RSP steel while a wide particle-size distribution in a matrix of coarse grains was evident in the conventional steel.

The size distributions of the dispersed particles for the RSP M-50 matrix steel after one-hour austenitizing above 1180°C are shown in Figures 13-15. The particle size varied from 600Å to 8000Å with apparent average particle sizes of 0.19 μm , 0.21 μm , and 0.26 μm after one-hour austenitizing at 1180°C, 1220°C, and 1260°C respectively. The corrected results also show a small change in particle-size distribution and the average particles sizes become 0.20 μm , 0.22 μm , and 0.27 μm after austenitizing at 1180°C, 1220°C, and 1260°C for one hour respectively. A wide particle size distribution was also observed in the conventional M-50 matrix steel, as shown in Figures 16-18. The average particle sizes are 1.4 μm , 1.6 μm , and 1.9 μm for the conventional steel austenitized at 1180°C, 1220°C, and 1260°C respectively.

4.1.2. Identification of the Dispersed Particles

High-resolution STEM microanalysis was used to analyze the compositions of the finely dispersed phases by energy dispersive x-ray analy-

sis via a thin-window x-ray detector. Considerable effort was made to identify and quantify the undissolved particles which were responsible for inhibiting grain growth at austenitizing temperatures above 1180°C where carbides have dissolved. Table 4 summarizes the types of stable particles present at 1180°C, 1220°C, and 1260°C in the RSP M-2 matrix steel. The energy dispersive x-ray spectrum of each phase is shown in Figure 19. Evidently, the simpler sulfides (MnS and VS) dissolved above 1180°C, but complex sulfides associated with SiO₂ still survived. After austenitizing at 1260°C, the remaining undissolved phases were SiO₂, Mg silicate (MgO-SiO₂), and two complex phases of SiO₂-VS and SiO₂-MnS. The average particle sizes of these two complex phases and silicates were larger than that of the simple SiO₂ phase. For austenitizing temperatures varying between 1180°C to 1260°C, the coarsening kinetics of SiO₂ and those phases associated with SiO₂ were near the same rate.

STEM and SEM were used to analyze the chemical composition of fine particles (<1μm) and coarse particles(>1μm), respectively, in the conventional M-2 matrix steel. The results of these analyses are listed in Table 5. No complex phases were present in the conventional M-2 matrix steel. Coarse carbides (0.8-10 μm) in the form of vanadium-rich, Mo, Cr, W carbide (MC) remained undissolved up to 1220°C. No excess carbides were detected in the RSP M-2 matrix steel after one-hour austenitizing above 1180°C. The presence of undissolved coarse carbides can be rationalized by supposing that these

carbides were too coarse to diffuse completely into the matrix within the one-hour austenitizing treatment. Also coarse sulfide particles (MnS, 0.5–4.0 μm) survived up to 1220°C in one-hour austenitizing treatments. No VS was detected in the conventional steel. Most of the vanadium was found in carbides rather than sulfides.

Table 6 lists the stable particles observed after austenitizing above 1180°C in the RSP M-50 matrix steel. Again, the simpler sulfides (MnS and VS) dissolved above 1220°C but complex sulfides associated with aluminum oxide still survived beyond their dissolution temperature. After austenitizing at 1260°C, the remaining undissolved phases were Al_2O_3 , SiO_2 , aluminum oxysulfide, Al silicate ($\text{Al}_2\text{O}_3\text{-SiO}_2$) and two complex phases of $\text{Al}_2\text{O}_3\text{-MnS}$ and $\text{Al}_2\text{O}_3\text{-VS}$. The corresponding energy dispersive x-ray spectrum for each phase is shown in Figure 20. The average particle sizes of silicate and complex phases were appreciably larger than those of simple phases (MnS, VS, Al_2O_3 , SiO_2 , and aluminum oxysulfide). The average particle size of aluminum oxysulfide was less than each stable phase. The solubility of the oxysulfide is much smaller than those of the oxide and sulfide (69,70). In the range of austenitizing temperatures 1180°C – 1260°C, the coarsening kinetics of those stable phases were about the same rate.

The stable phases after austenitizing above 1180°C in the conventional M-50 matrix steel are listed in Table 7. No complex phases were present in the conventional M-50 matrix steel.

Simple sulfides dissolve above 1220°C. Oxides (SiO_2 and Al_2O_3) oxysulfide, and silicate remain undissolved up to 1260°C. Clearly, the particle sizes of stable phases in the conventional M-50 matrix steel were smaller than those in the conventional M-2 matrix steel. The cooling rate during solidification of the conventional M-50 matrix steel was faster than that of the conventional M-2 matrix steel due to the smaller diameter ingot. This indicates that a faster cooling rate during solidification can produce finer precipitate particles. No coarse carbides (vanadium-rich, W, Mo, Cr carbide) were present in the conventional M-50 matrix steel. This can be attributed to the lower content of carbon and carbide-forming alloy elements (V, Cr, and no W).

Complex phases of sulfides (MnS and VS) with oxides (SiO_2 or Al_2O_3) were observed in both RSP matrix steels. The oxide component is SiO_2 in the M-2 matrix and Al_2O_3 in the M-50 matrix. This difference is consistent with the initial melt history which included Si-deoxidation in the M-2 matrix and Al-deoxidation in the M-50 matrix steel. Such complex phases were not found in either conventional matrix steel. The formation of such complex phases is likely due to the large melt supercooling in RSP. Waters et al. (71) have observed a combined oxide-carbide phase in RSP nickel-based superalloys.

Mg-bearing silicates were found only in the RSP M-2 matrix steel. The chemical analysis of Table 1 confirms that the Mg content of the RSP M-2 matrix steel was increased by 20 times that of the conventional

material and that the oxygen content was increased by a factor of about 10. The occurrence of Mg-bearing silicates probably resulted from the interaction between the melt and the refractory materials of the remelting crucible during the atomizing process.

4.1.3 Volume Fraction of Second-Phase Dispersions

The volume fraction of precipitates over the austenitizing temperatures examined can be estimated from the thin-foil electron micrographs (68). The volume fraction of each phase and volume fraction for a given particle size were estimated based on observed size and frequency of appearance. Figure 21 shows the volume fraction of precipitates and volume fraction of each phase in the RSP M-2 matrix steel. The volume fractions of oxide (SiO_2) and silicate ($\text{MgO} - \text{SiO}_2$) in austenite remain fairly unchanged up to 1260°C for their low solubilities in austenite. The volume fraction with respect to the size distribution over the temperatures studied is shown in Figure 22 .

The volume fraction of undissolved precipitate particles after one-hour austenitizing at 1180°C , 1220°C , and 1260°C in the RSP M-50 matrix steel is shown in Figure 23. The volume fractions of oxides (SiO_2 and Al_2O_3), oxysulfide, and silicate remain relatively unchanged over the temperatures of interest. This is because of their low solubilities in austenite. The volume fraction with respect to the particle size distribution is shown in Figure 24.

The sulfur content of the M-50 matrix steel was higher than that of

the M-2 matrix steel ; consistent with this, the volume fraction of sulfides observed in the M-50 matrix steel was larger than in the M-2 matrix steel. The dissolution temperature of sulfides can be determined by extrapolating the volume fractions of sulfides at 1180°C, as shown in Figures 21 and 23. The determined dissolution temperatures are 1220°C and 1240°C for M-2 and M-50 matrix steels, respectively. The 20°C difference in dissolution temperature is consistent with the difference in sulfur content. Evidence shows that the average size of sulfide particles in the RSP M-50 matrix steel was a little larger than in RSP M-2 matrix steel. Although the additional sulfur content of the M-50 matrix steel may enhance the pinning force by increasing the volume fraction of sulfides, it apparently promotes particle coarsening during subsequent heat treatment.

4.1.4 Morphology of Second-Phase Particles

In both RSP matrix steels, the precipitate particles were finely dispersed with particle size varying from 600^oÅ to 8000^oÅ. Electron micrographs of the RSP matrix steels are shown in Figures 25 and 26. These precipitates were observed in the shape of relatively equiaxed globules. The SEM was used to examine the particle morphology in the conventional materials. Figures 27 - 29 show typical shapes of particles in both conventional materials. Type 1 MnS usually appeared as an isolated globular particle on grain boundaries in the matrix. Some MnS was present as an irregular shape of particle in the matrix. SiO₂ with a size of about 9 μm appeared as an irregular inclusion. In the conventional M-2 matrix steel, coarse carbides (vanadium-rich, W, Mo, Cr carbide; 0.8-10μm) sur-

vived up to 1220°C and had the form of irregular ellipsoids and irregular plate-like particles. The refinement of precipitate and morphological modification of precipitates in the RSP steels may result in a finer grain size and lead to some beneficial effects in mechanical properties.

4.2 Grain Growth Characteristics

4.2.1 Isothermal Grain-Growth Characteristics

The time dependence of austenitic grain growth at high temperatures was examined in both matrix steels. The Log-Log plots of grain size vs. time in hours are shown for M-2 matrix steel in Figures 30 and 31, and for M-50 matrix steel in Figures 32 and 33. The abrupt changes in slope correspond to the onset of abnormal grain growth and are marked as 'x' points. The data are reasonably well represented by a straight line for normal grain growth at temperatures studied. This indicated that the isothermal grain growth behavior is consistent with the equation, $\bar{D} = K t^n$. The value of the time exponent, n , varies from 1/2.7 to 1/3.6. For the RSP M-2 matrix steel, n is about 1/3.1 at temperatures above 1180°C, while for the RSP M-50 matrix steel, n is about 1/3.5 at temperatures above 1100°C.

During prolonged isothermal treatment, grain growth accompanies particle coarsening. The limiting grain size, \bar{D} , is proportional to the ratio of \bar{d}/f_v , as indicated in equation(17). Jones(72) studied the kinetics of particle coarsening in RSP aluminum alloys. The indication is that accelerated boundary-diffusion controlled coarsening can be important at lower temperatures, but that the volume-diffusion controlled coarsening predominates in the higher temperature range of interest here. For the case of small f_v and uniform dispersions, the volume-diffusion controlled coarsening of second-phase particles can be treated by the Lifshitz-Slyozov-Wagner (LSW) theory (45,46), as shown in equation (18). Combining equations (17) and (18), then a prediction of $t^{1/3}$ time dependence is obtained for particle-pinning controlled grain growth.

The present experimental results, with an n value of $\sim 1/3$, suggest that the rate of isothermal grain coarsening is in accordance with the kinetics of volume-diffusion controlled particle coarsening. Hence, particle-pinning controlled grain growth prevails in both matrix steels. The deviation of n value from $1/3$ may be attributed to the wide range of particle size, the finite initial particle size, the shape of the particles, and the presence of prior powder-particle boundaries. That pinning is due to more than one type of particle may also lead to the variability of the time exponent, n .

4.2.2 Prior Powder-Particle Boundaries

It is interesting to note that n is as large as $1/1.6$ at the initial stage of 1100°C austenitizing treatment for the RSP M-2 matrix steel. This is due to the presence of prior powder-particle boundaries promoting abnormal grain growth. By optical microscopy, abnormal grain growth was observed within prior powder-particle domains. These domains were elongated ellipsoids with dimensions of $300\ \mu\text{m}$ in length and $25\ \mu\text{m}$ in width, as shown in Figure 34. The grains at the middle of the domains are larger than the grains at the tips of the domains. The prior powder-particle domains were detectable after short-time low-austenitizing treatment and disappeared after long-time or higher-austenitizing treatment. This suggests the occurrence of segregation at the surface of the powder particles.

Waters et al. used Auger Electron Spectroscopy to study prior powder-

particle boundaries in hot isostatically pressed (HIP) nickel-based superalloy. Experimental results confirmed that combined oxide-carbide morphology was retained at the prior powder-particle boundaries in the as-HIPPed material. Ross and Kear (73) have analyzed the surface composition of rapidly solidified superalloy powders using Auger Electron Spectroscopy. They have shown that certain components of the melt, such as C, S, O, Zr, and Ti, segregate to the surface during processing. It was proposed that when the nucleation of solids takes place at the surface of a liquid droplet, the solidification front travels rapidly to the other side of the droplet and so various solutes will then pile-up at the surface. In the present work, no prior powder-particle domains were observed in the RSP M-50 matrix steel after short-time low-austenitizing treatment. The excess carbides dissolve above 1100°C in the M-50 matrix steel and the volume fraction of carbides in the M-2 matrix steel is about 2 % at 1100°C (7). Therefore, the strong grain-boundary pinning at the prior powder-particle boundaries of the RSP M-2 matrix steel may be caused by the segregation of C, V, Mo, W, and Cr at the powder surfaces.

4.2.3 High-Temperature Grain-Coarsening Resistance

The as-received conventional material had a hardness of $H_{\text{RC}} \sim 10$ in the annealed condition, while the RSP material in the as-extruded condition had a hardness of $H_{\text{RC}} 52$. Figure 35 compares the grain growth behavior between the conventional and RSP M-2 matrix steels. The conventional material starts to coarsen at 1140°C and reaches a grain diameter of $700 \mu\text{m}$ at 1300°C for one hour. At temperatures above 1140°C , the grain growth becomes time and temperature dependent. In contrast, the RSP material

possesses a remarkable grain coarsening resistance after one hour of high austenitizing treatment up to 1300°C . As indicated in Figure 35, the effectiveness of RSP in this respect is not very sensitive to the size of the RSP powders. The optical micrographs of these two steels are shown in Figure 5. The excess carbides in the M-2 matrix steel are almost completely dissolved above 1180°C , and yet the RSP M-2 matrix steel still exhibits pronounced grain-coarsening resistance.

Similarly, grain-coarsening resistance at high temperatures is also observed in the RSP M-50 matrix steel, as shown in Figure 36. The conventional material coarsens to about $500\ \mu\text{m}$ at 1300°C for one hour while the RSP material maintains a strong coarsening resistance. In addition, the effectiveness of RSP in retarding grain growth is not sensitive to the size of the RSP powders. Optical micrographs of these two materials are shown in Figure 12. The excess carbides are almost completely dissolved above 1100°C in the M-50 matrix steel. This also indicates that the RSP M-50 matrix steel exhibits high-temperature grain-coarsening resistance even after the excess carbides have been dissolved.

The volume fraction of residual pores in RSP steels can be estimated from density measurements. The densities of the M-2 and M-50 RSP matrix steels were 99.8% and 99.7% relative to the densities of conventional matrix steels. The density measurement of RSP matrix steels showed a lower volume fraction of pores than of second-phase particles. The residual pores or voids in the hot-consolidated RSP matrix steels are quite large, as shown in Figure 2. Hence the contribution of residual pores or voids

to grain-boundary pinning is insignificant and can be neglected.

Carbides are very effective grain-growth inhibitors in high-speed steels but tend to dissolve or readily coarsen at high temperatures. Previous studies in the RSP steels(19,25,26) have indicated that a fine dispersion of relatively insoluble sulfides can be obtained during rapid solidification processing, which may act to pin grain boundaries effectively at high temperatures up to 1200°C. In this study, MnS as well as VS act as effective pinning particles in retarding grain growth. The present experimental results on both RSP matrix steels(Tables 4 and 6) suggest that other potential grain-growth inhibitors, such as oxides(SiO_2 and Al_2O_3), aluminum oxysulfide, silicates, and complex phases are also playing an important role in retarding grain growth. It is evident that simpler sulfides(MnS or VS) dissolve above 1200°C. When associated with oxides, the complex sulfides survive to higher temperatures in austenite, and thereby can still contribute to grain-boundary pinning. Because of their low solubilities in austenite, the stable phases of oxides, oxysulfide, and silicates remain relatively unchanged at high temperatures up to 1260°C, and thus can pin grain boundaries effectively at such high temperatures. Evidence is that both M-2 and M-50 RSP matrix steels can maintain a significant austenitic grain-growth resistance at high austenitizing temperatures even after all carbides and simpler sulfides have dissolved.

4.2.4 Conventional M-2 vs. M-50 Matrix Steels

The comparison of grain growth behaviors between the conventional M-2 and M-50 matrix steels is shown in Figure 37. The M-50 matrix steel exhibits a slower grain-growth rate, even with a larger initial grain size. The difference of grain-growth behaviors in these two conventional steels can be correlated with the effective pinning particles.

The M-50 matrix steel was derived from the matrix composition of M-50 steel when austenitized at about 1095°C. Experimentally, excess carbides dissolved at about 1100°C in the M-50 matrix and 1180°C in the M-2 matrix steels. The volume fraction of carbides in the M-2 matrix steel was estimated at about 2 % at 1100°C and 1 % at 1150°C (7). Consequently, the M-2 matrix steel obtains a finer grain size at 1100°C. As the temperature is increased to 1180°C, however, the volume fraction of total undissolved phases in the M-50 matrix steel is more than that in M-2 matrix steel due to the addition of sulfur and aluminum in the M-50 matrix steel (Figures 21 and 23). Additionally, the mean particle size in the conventional M-50 matrix steel is smaller than in the conventional M-2 matrix steel (tables 5 and 7). This is likely due to faster solidification (smaller ingot dia.) of the M-50 matrix steel. Only the finer particles are responsible for effective grain-boundary pinning. There are more effective second-phase particles in the M-50 matrix steel than in the M-2 matrix steel. In addition to the grain-boundary pinning effect, the fine particle size resulting from faster solidification in the M-50 matrix steel may also lead to some beneficial effect on mechanical properties.

During the subsequent heat treatment of steels, the initial precipitates tend to coarsen at high temperatures and thus reduce the retarding effect on grain growth. The particle coarsening may also deteriorate somewhat the mechanical properties. According to equation(18), the rate of particle coarsening depends on the DC product of the rate-controlling species in the matrix at a certain temperature for a given alloy composition. The grain-growth inhibitors with the most potential are high-melting second-phases with low solubility in the austenite, thereby to resist dissolution as well as coalescence in the matrix phase.

4.3. Relation of Second-Phase Dispersions to Grain-Growth Characteristics

4.3.1. Relation of \bar{D} vs. \bar{d}/f_v .

Equation (17) indicates that the quantitative relationship between grain size and second-phase dispersion size is : $\bar{D} = K \frac{\bar{d}}{f_v}$. This linear relationship can be tested by plotting \bar{D} vs. \bar{d}/f_v . The results for RSP matrix steels and conventional matrix steels are shown in Figures 38 and 39 respectively. The data for RSP materials were directly determined through observation. The volume fractions in the conventional material were assumed equivalent to those of RSP material but with appropriate correction for the change in chemical composition after RSP and survival of coarse inclusion particles beyond their own dissolution temperatures. A near straight-line relationship was obtained in both RSP materials. The value of the constant, K, varied between 0.52 and 0.6 for RSP materials. The K values for conventional material were 0.42 - 0.32 which are less than those of the RSP material. The grain-size distribution parameter, Z, measured from the observation of optical micrographs was about 1.7 for RSP materials and about 1.6 for conventional materials. This indicates that Z values fall in the range of 2 to 4 / 3 for both matrix steels undergoing normal grain growth. It is known that a large Z value may result in a higher K value. Thus the value of Z is consistent with the value of K in both matrix steels.

Existing grain-boundary pinning models were tested against the available experimental results for steels, including the present work. The comparisons are shown in Figure 40. It is seen that those models fail to give a satisfactory estimation of inhibited grain size on a quantita-

tive basis.

4.3.2. Grain-Boundary Pinning Theory

In grain growth the driving force is provided by the interfacial energy of the grain boundary, or more strictly, by the release of energy which arises from any reduction of the overall grain-boundary area within the specimen. The quantitative relation of grain size and second-phase particles was first proposed by Zener (29) who considered the case of uniform spherical particles with a matrix-phase of spherical grains. Zener's original model predicts a much larger equilibrium grain size than is observed. Gladman (32) has criticized Zener's treatment for ignoring the fact that the contraction of an interface often involves the expansion of another attached interface, and the assumption of spherical grain shape misrepresents the topology of a real metal grain. Gladman (32) has given a detailed appraisal of the energy changes which accompany the particle-boundary unpinning process for a dispersion of uniform spherical second-phase particles in a matrix of tetrakaidecahedral grains. The estimation of inhibited grain size based on Gladman's treatment gives a lower limiting grain size than the experimental observation. This discrepancy can be attributed to an overestimate of the total restraining force of the particles. Hellman-Hillert's analysis (31) is based on the extension of Hillert's grain-size distribution theory and modification of Zener's treatment on the net restraining force of all particles in contact with boundaries. They suggested that a statistical approach was required to achieve a satisfactory treatment of the net effect of

all the second-phase particles in a specimen.

Table 8 lists the existing grain-boundary pinning models with relevant variables considered. When applied to experimental results in steels, the existing grain-boundary pinning models fail to give a satisfactory estimation of the observed grain size, as shown in Figure 40. The physical significance of the grain-size contrast parameter Z (as discussed in Section 2.5) is that only large grains will grow at the expense of neighboring small grains in a polycrystalline structure. The restraining force exerted by a particle also depends on the relative position of the particle to the grain boundary. An attempt is made here to synthesise the approaches of Gladman and Hellman-Hillert to obtain a model which accounts for the observed grain-coarsening behavior.

We first consider a tetrakaidecahedron which gives a reasonable approximation to the shape of a real metal grain. The assumption is that the second-phase particles are rather evenly distributed in the material, and only particles in contact with a grain boundary can provide a pinning force. The driving force and pinning force for grain-boundary migration are then derived as follows :

A growing grain has a radius R in a matrix of regular grains having a mean radius \bar{R} . If the grain radius R grows to a radius of $(R + \Delta R)$, then the grain-boundary area eliminated, A_e , is :

$$A_e^A \cong 3 \Delta R / \bar{R} \quad (21)$$

However, the growing grain also increases its own area of boundary, A_i :

$$A_i^A \cong 2 \Delta R / R \quad (22)$$

The net change in area, A_n , is :

$$A_n = A_e - A_i = \Delta R (3 / 2\bar{R} - 2 / R) \quad (23)$$

The net change of grain-boundary interfacial energy per unit boundary area is σA_n ;

$$\sigma A_n = \frac{\sigma \Delta R}{R} (\frac{3}{2} - \frac{2}{Z}) \quad (24)$$

where $Z = R / \bar{R}$.

The driving force for grain growth per unit grain-boundary area, F_D^A , is :

$$F_D^A = \frac{\sigma}{R} (\frac{3}{2} - \frac{2}{Z}) \quad (25)$$

The restraining force caused by a single particle at the boundary is $2 \sigma \pi r \sin \theta \cos \theta$. The maximum restraining force per particle is then $\sigma \pi r$, corresponding to $\theta = 45^\circ$ (29). Considering the particles of discrete size classes and summing up the total restraining force over all the particles interacting with a unit area of the boundary :

$$F_p^A = 6 \pi \sum_i N_i^A r_i \quad (26)$$

Where N_i^A is the number of particles of a given size r_i per unit area of grain boundary. Assuming a random distribution of particles within the volume, N_i^A will be sensitive to the degree of boundary flexibility.

Let the effective interaction distance of the boundary be δ_i , noting that this distance depends on r_i . Then:

$$N_i^A = \delta_i N_i^V \quad (27)$$

where N_i^V is the number of particles of a given size r_i per unit volume.

Thus :

$$N_i^V = \frac{f_i}{\frac{4}{3} \pi r_i^3} \quad (28)$$

$$F_p^A = 6 \frac{3}{4} \sum \frac{f_i r_i}{r_i^2} \quad (29)$$

$$\text{Let } \delta_i = \alpha r_i \quad (30)$$

where α is a factor which can be determined by comparison with experiment.

We then obtain:

$$F_p^A = 6 \alpha \frac{3}{4} \sum \frac{f_i}{r_i} \quad (31)$$

The limiting grain size is obtained by equilibrating the driving force and net restraining force per unit area of boundary.:

$$F_D^A = F_P^A$$

$$\frac{\sigma}{\bar{R}} \left(\frac{3}{2} - \frac{2}{Z} \right) = \sigma \alpha \frac{3}{4} \sum \frac{f_i}{r_i} \quad (32)$$

$$\bar{R} = \frac{4}{3\alpha} \left(\frac{3}{2} - \frac{2}{Z} \right) / \sum \frac{f_i}{r_i} \quad (33)$$

$$\bar{D} = \frac{4}{3\alpha} \left(\frac{3}{2} - \frac{2}{Z} \right) / \sum \frac{f_i}{d_i} \quad (34)$$

where \bar{D} is the limiting grain diameter and d_i is the diameter of a given particle. If the detailed information of particle size distribution is unknown, the equation (34) can be alternatively approximated as :

$$\bar{D} = \frac{4}{3\alpha} \left(\frac{3}{2} - \frac{2}{Z} \right) \frac{\bar{d}}{f_v} \quad (35)$$

where \bar{d} is the average particle diameter.

The summation of f_i / d_i over the particle-size distribution can be obtained from Figures 22 and 24 for M-2 and M-50 RSP matrix steels respectively. The comparison of equations (34) and (35) is given in Tables 9 and 10 for M-2 and M-50 RSP matrix steels respectively. In this comparison

α was taken as 1.0 and the parameter, Z , was determined experimentally to be equal to 1.7. It is evident that the measured and calculated grain sizes are in good agreement. The calculated results with equation (34) give a better agreement than with equation (35). The difference in the calculated results between equations (34) and (35) is in the range of 15% - 30%. This demonstrates convincingly that the high-temperature grain-coarsening resistance in these RSP steels is due to grain-boundary pinning by finely dispersed second-phase particles. Some other available data on grain growth with second-phase observations in non-RSP materials (33,43,74) have been reviewed and checked with the proposed grain-boundary pinning model. Figure 41 shows a comparison of the proposed model with available experimental results. The factor α was taken as 1.0 for each material. Arrows indicate the change of the ratio of \bar{d}/f_v when equation (34) is applied. The RSP points move from the $Z = 1.8$ to the $Z = 1.7$ lines, which give a better agreement with the experimental results. All such findings can be rationalized on a quantitative basis according to equations 34 or 35.

In the Zener and Hellman-Hillert treatments α was taken as 1.0 while Gladman assumed $\alpha = 2.0$. A proper test of the factor, α , can be made from the present experimental results. Comparing the measured results and the calculated results with equation (34) in Tables 9 and 10, the value of α falls in the range of 0.95-1.25. This comparison indicates that $\alpha = 1$ is a fair approximation while $\alpha = 2$ may lead to

some underestimation of the limiting grain size.

4.4 Mechanical Behavior

The application of high-austenitizing treatments for high-strength steels has indicated that K_{IC} sharp-crack fracture toughness is significantly increased, but usually results in a decrease of CVN blunt-notch fracture toughness as the austenitizing temperature is increased. The latter trend is due to excessive grain coarsening. Accordingly, the high-temperature resistance to grain growth exhibited by RSP steels may be used to improve mechanical properties by coupling with high-austenitizing treatments. Both matrix steels can be considered as prototypes to explore the potential of improved mechanical properties in RSP martensitic steels.

A comparison of mechanical properties between conventional and RSP M-2 matrix steels over the austenitizing temperatures examined is shown in Figure 42. The steels were austenitized at each temperature for one hour and double tempered at 565°C for 2+2 hours. The density of the RSP steel is 99.8 % relative to that of the conventional steel. There is no significant difference in hardness between conventional and RSP steels, but both depend sensitively on austenitizing temperature. For conventional M-2 matrix steel, a high K_{IC} fracture toughness is obtained at 1140°C. The toughness enhancement may be due to the elimination of void-initiating excess carbides. Lower toughness at higher temperatures may be due to excessive grain coarsening. The fractography shows a mixed fracture mode of quasi-cleavage and a small amount of dimple rupture. The K_{IC} value of the RSP steel is increased compared to the conventional steel. The increase

of K_{IC} is higher at higher austenitizing temperature, consistent with the larger difference in microstructure between the RSP and conventional steels. A significant improvement in CVN blunt-notch fracture toughness is evident for the RSP steel after austenitizing over the intermediate range of temperature. This is mainly due to the refined microstructure and high-temperature grain-coarsening resistance through rapid solidification processing. CVN blunt-notch fracture toughness is generally found to be more sensitive to grain size.

The commercial hardening temperature for M-2 matrix steel is 1100°C. On raising the hardening temperature to 1140°C, the hardness can be increased without detriment to the K_{IC} toughness, but the CVN value deteriorates. On the other hand, when the RSP M-2 matrix steel is austenitized at 1140°C, the K_{IC} and CVN levels are maintained despite the increase in hardness.

Additional hot-working processes were applied to the as-extruded RSP M-2 matrix steel in order to obtain a fully dense material. Hot isostatic pressing (HIP at 1100°C / 3 hours, 30 Ksi) and hot rolling (1100°C. 50% reduction in thickness) were undertaken separately or together on as-extruded RSP M-2 matrix steel. The density measurements and K_{IC} fracture toughness values of the M-2 matrix steels are summarized in Table 11. The density of RSP steel is increased to 99.9 % of that of conventional steel. The additional hot-working processes at 1100°C may cause unavoidable coarsening of grain size and precipitate particles. The results show that K_{IC} fracture toughness is insensitive to austenitizing temperatures

above 1140°C and a small improvement in density. It is worth noting that the K_{IC} fracture toughness of RSP M-2 matrix steel followed HIPping and hot rolling is improved with austenitizing temperatures up to 1180°C.

The mechanical properties of RSP and conventional VAR M-50 matrix steels are compared in Figure 43. The M-50 matrix specimens were austenitized at each temperature for one hour and triple tempered at 540°C for 2+2+2 hours in order to achieve typical secondary hardening. The density of the RSP M-50 matrix steel was 99.7 % relative to that of conventional M-50 matrix steel. The hardness of the RSP steel is about H_{RC} 1.2 higher than that of the conventional steel. This is mainly due to the difference of carbon content between the RSP and conventional M-50 matrix steels (Table 1). It is worth noting that the K_{IC} of the conventional M-50 matrix steel is unusually high for a tool steel. A high K_{IC} value of 45 $Ksi\sqrt{in}$ with a hardness of H_{RC} 56 is obtained at 1100°C. The fractography reveals a mixed fracture mode of quasi-cleavage and a fair amount of dimpled rupture, as shown in Figure 44. This also indicates that the coarse grain may be counter-balanced somewhat by the elimination of excess carbides at high temperatures. The K_{IC} fracture toughness of RSP M-50 matrix steel is lower than that of the conventional M-50 matrix steel. However, the fracture toughness of hardened-and-tempered martensitic steel is not only a simple function of microstructure. The lower K_{IC} fracture toughness is associated with an increase in hardness. It seems that the K_{IC} fracture toughness is very sensitive to the hardness variation. On the other hand, the CVN fracture toughness of RSP steel is slightly increased in spite of the higher hardness level.

Additional hot-working processes such as HIPping, hot-rolling, and hot forging at 1100°C were applied to the as-extruded RSP M-50 matrix steel to help improve the density. The density measurements and K_{IC} fracture toughness values are listed in Table 12. The density of the RSP M-50 matrix steel after subsequent hot working is improved to within 0.2 % of the conventional M-50 matrix steel. Residual pores or voids resulting from powder processing and imperfect consolidation were clearly observed on the fracture surface of the RSP steel after the hot-working process, as shown in Figure 45. However, there is considerable coarsening of the microstructure. The K_{IC} fracture toughness remains fairly level after the hot-working. The K_{IC} fracture toughness is more sensitive to hardness than to the austenitizing temperature. The optimum austenitizing temperatures for both RSP M-2 and M-50 matrix steels are 1140°C and 1100°C respectively. The variation of the K_{IC} sharp-arack fracture toughness of high-strength steels (4,7,75,76) with hardness in the range H_{RC} 52 to 63 is shown in Figure 46. It demonstrates that the K_{IC} value is very sensitive to hardness. It is observed that the K_{IC} value of RSP matrix steels (for optimum heat treatment) is still comparable to that of conventional high-strength steels even if the RSP matrix steel is not of full density. Figure 47 shows the CVN fracture toughness versus hardness for both RSP and conventional matrix steels. Grain sizes and relative densities of RSP materials are indicated in parentheses. There is a clear indication that the CVN energy of the RSP matrix steel is significantly improved over the conventional matrix steels when compared at equal hardness levels, consistent with the RSP microstructural refinement.

In agreement with previous results on M-2 matrix steel (7), the fracture toughness results summarized in Figures 42 and 43 indicate that the present steels derive little improvement in K_{IC} sharp-crack fracture toughness from the use of high austenitizing temperatures, in contrast to the effects previously observed for lower alloy steels (59-66). This is consistent, however, with the observation (27) that the toughness improvements in the latter steels are confined to the first stage of tempering where strengthening arises from ϵ carbide, and significant amounts of metastable retained austenite are present. The secondary-hardened matrix steels examined here were tempered at much higher temperatures. The benefit of high austenitizing in these steels is the dissolution of alloy carbides and the achievement of full hardness. In this condition, where the conventionally processed steels exhibit excessive grain coarsening, the coarsening resistance of the RSP steels allows practical attainment of full hardness with a significant advantage in blunt-notch CVN toughness.

5. CONCLUSIONS

1. Significant austenitic grain-growth resistance is observed in both M-2 and M-50 RSP matrix steels at high austenitizing temperatures even after all carbides and simple sulfides are dissolved.
2. In both of these matrix steels, the isothermal grain-growth behavior can be expressed as $\bar{D} = K t^n$ at high temperatures with n near $1/3$, consistent with dispersion-controlled grain growth.
3. The operative grain-growth inhibitors are identified as sulfides, oxides, oxysulfides, silicates and complex phases. When associated with oxides as complexes, sulfides survive beyond the dissolution temperature of the simple sulfides. In addition to such complex sulfides, the most prominent dispersed phases are SiO_2 , Al_2O_3 , oxysulfide, and silicates. These phases are an order of magnitude finer in the RSP material, and the complex phases are absent in the conventional material.
4. A model of grain-boundary pinning by dispersed second-phase particles is developed, which accounts for the observed grain-growth behavior in these matrix steels and also in steels more generally. It is confirmed that high-temperature grain-coarsening resistance in RSP steels is due to the fine dispersion of relatively insoluble second-phase particles. This model takes into account the distribution of particle sizes existing in the dispersion.

5. The RSP M-2 matrix steel can be hardened at a higher-than-usual temperature (1140°C) to achieve higher hardness without detriment to the K_{IC} and CVN toughness levels.

6. For a given hardness, the CVN blunt-notch fracture toughness in both M-2 and M-50 RSP matrix steels is appreciably higher than in the conventional matrix steels, while the sharp-crack K_{IC} toughness is not materially effected. This is consistent with the greater sensitivity of CVN fracture toughness to the micro-structural refinement.

References

1. F. Kayser and M. Cohen, "Carbides in High-Speed Steels- Their Nature and Quantity", Metal Progress, June 1952, P.79.
2. VASCO-MA Steel, VASCO, Latrobe, PA. 15650
3. B. L. Averbach, Metal Progress, December 1980, P.19.
4. J.A. Rescalvo and B.L. Averbach, Met. Trans., Vol. 10A, September 1979, P.1265.
5. G.A. Roberts, J.C. Hamaker, Jr., and A.R. Johnson, "TOOL STEELS" 3rd. edition, ASM, 1962.
6. L.M. Barker and W.C. Leslie, Fracture 1977, Waterloo, Canada, June 1977, Vol. 2, P.305.
7. C.M. Kim, A.R. Johnson, and W.F. Hosford, "Fracture Toughness of AISI M-2 High-Speed Steel and Corresponding Matrix Tool Steel", Met. Trans., Vol. 13A, September 1982, P.1595.
8. "Rapid Solidification Processing", Proceedings of International Conference on Rapid Solidification Processing, 1977. Claitor's Publishing Division.
9. "Rapidly Quenched Metals", Proceedings of 2nd. International Conference on Rapidly-Quenched Metals, edited by N. J. Grant and B.C. Giessen, MIT Press, 1975.
10. "Rapidly Quenched Metals", Proceedings of 3rd. International Conference on Rapidly-Quenched Metals, edited by B. Cantor Chameleon Press, London, 1978.
11. T.R. Ananthranaman et al., in the Proceedings of 3rd. International Conference on Rapidly-Quenched Metals, edited by B. Cantor Chameleon Press, London 1978.
12. M. Cohen, B.H. Kear and R. Mehrabian, 2nd. International Conference on Rapid Solidification Principles and Technologies. Reston, Virginia, 1980.
13. R.W.K. Honeycombe, in Proc. of 3rd. Int. Conf. on Rapidly-Quenched Metals, edited by B. Cantor, Chameleon Press, London, 1978, P.73.
14. R. Wang, in the Proceedings of 2nd. Int. Conf. on Rapidly Solidified Metals, edited by N.J. Grant and B.C. Giessen, MIT Press, 1975
15. J.V. Wood and R.W.K. Honeycombe, Mat. Sci. Eng. 23 (1976) 107.

16. Y. Inokuti and B. Cantor, *Scripta Met.*, 10 (1976) 655.
17. J.V. Wood, A. Crossley and W.M. Stobbs, in the Proceedings of 3rd. Int. Conf. on Rapidly-Quenched Metals, 1978.
18. R. Mehrabian, "Rapid Solidification Processing Principles and Technology", in the Proceedings of Int. Conf. on Rapid Solidification Processing (1977), Claitor's Publishing Division.
19. T. Kelly and J.B. Vander Sande, 2nd. Int. Conf. on Rapid Solidification, Reston, Virginia, 1980, P.100.
20. J.J. Rayment and B. Cantor, *Met. Trans.* 12A (1981) 1557.
21. D.G. Morris, *Metal Science*, March 1981, P.116.
22. I.R. Sare and R.W.K. Honeycombe, in Ref. 4, P.179.
23. P.R. Strutt, H. Nowotny, Y.W. Kim and B.H. Kear, in Ref. 8, on RSP, Claitor, L.A. 1978, PP.112-115.
24. M. Tuli, P.R. Strutt, H. Nowotny and B.H. Kear, Proc. of 2nd. Int. Conf. on RSP, PP.112-115, Claitor, L.A. 1978.
25. J. Goss, M.S. Thesis, Dept. of Mat. Sci. & Eng. MIT (1980).
26. M. Suga, J. Goss, G.B. Olson and J.B. Vander Sande, 2nd. Int. Conf. on Rapid Solidification Principles and Technology, Virginia, 1980 P.364.
27. P.G. Fleyshman, M.S. Thesis, Dept. of Mat. Sci. & Eng. MIT (1983).
28. P. Cotterill and R. Mould, "Recrystallization and Grain Growth in Metals", John Willey & Sons Inc., N.Y. (1976).
29. C. Zener, quoted by C.S. Smith, *Trans. AIME* 175 (1948) P.47.
30. P. Hellman and M. Hillert, *Scandinavian Journal of Metallurgy*, 4 (1975) 211.
31. M. Hillert, *Acta Met.* 13 (1965) 227-238.
32. T. Gladman, *Proc. R. Soc. A* 294 (1966) 298.
33. T. Gladman and F.B. Pickering, *JISI* 205 (1967) 653.
34. B.E. Kula, "Grain Growth in High-Speed Steels" Thesis, MIT (1954).
35. O.O. Miller, *Trans. ASM* 43 (1951) 260.

36. K.J. Irvine, F.B. Pickering, and H. Gladman, Vol. 205 JISI (1967) 161
37. J.E. May and D. Turnbull, Trans. Met. Soc., AIME, 212 (1958) 769.
38. J.E. May and D. Turnbull, J. Appl. Phys. 30, 2105 (1959).
39. B.R. Barnejee, R.E. Lenhart, and W.H. Robinson, J. Appl. Phys. 33 12245 (1962).
40. H.C. Fiedler, Trans. Met. Soc., AIME 230 (1964) 95.
41. H.C. Fiedler, Trans. Met. Soc., AIME, 230 (1964) 603.
42. J. Howard, Trans. Met. Soc., AIME, 233 (1965) 1791.
43. J.W. Flowers, Jr. and S.P. Karas, J. Appl. Phys., 38 (1967) 163.
44. P.A. Beck, M.L. Holyworth and P.R. Sperry, AIME, Trans. 180 (1949) 163.
45. J.M. Lifshitz and V.V. Slyozov, J. Physics Chem. Solids, Vol 19 (1961) 35.
46. C. Wagner, Z. Elektrochem., Vol. 65 (1961) 581.
47. G.B. Olson, H. Ling, J.B. Vander Sande and M. Cohen in the Proc. of Annual Meeting of Materials Research Society, held in Boston 1981. Vol.8, Rapidly Solidified Amorphous and Crystalline Alloys.
48. R. Coladas, J. Masounave, G. Guerin and J.P. Bailon, Metal Science, 1977, Vol. 11 p. 509.
49. E.T. Turkdogan and S. Ignatowicz, JISI; 180 (1955) pp.349 - 354.
50. S. Matsuda and N. Okumura, Tetsu-to-Hagane, J. Iron and Steel Inst., Japan, 1976, Vol. 62.
51. T.J. George and J.J. Irani, J. Australia Inst. of Metals, 1968, Vol. 13, p. 94.
52. P.A. Beck, J.C. Dremer, L.J. Demer and M.L. Holzworth, Trans. Met. Soc., AIME, 175 (1948) 372.
53. P.A. Beck, J. Appl. Phys., 19 (1948) 526.
54. P.A. Beck, J. Toucers and W.D. Manley, Trans. Met. Soc. AIME, 175 (1951) 634
55. P.A. Beck, M.L. Holzworth and H. Hu, Phys. Rev., 73 (1948) 526

56. J.E. Burke, Trans. AIME, 180 (1949) 73.
57. R.L. Fullman, in Metal Interfaces, ASM, Cleveland, 1952, pp. 179-207.
58. F.N. Rhines and K.R. Craig, Met. Trans., 5 (1974) 413.
59. G.Y.Lai, W.E. Wood, R.C. Clark, V.F. Zackay, and E.R. Parker, Met. Trans., 5 (1974) 1663.
60. R.O. Ritchie, B. Francis, and W.L. Server, Met. Trans. 5A (1976) 831.
61. W.E. Wood, Engineering Fracture Mechanics, 1975, Vol. 7, pp. 219-234.
62. W.E. Wood, Met. Trans., 8A (1977) 1195.
63. R.O. Ritchie and R.M. Horn, Met. Trans., 9A (1978) 331.
64. D.S. McDermid, Metals Technology, Jan. 1978, p. 7.
65. D.S. McDermid, Metals Technology, Sep. 1980, p. 372.
66. F.B. Pickering and A.D. Vassiliou, Metals Technology, Oct., 1980, P.409.
67. J.M.G. Crompton, R.M. Waghorne, and G.B. Brook, British J. Appl. Phys. 17 (1966) 1301.
68. E.E. Underwood, "Quantitative Stereology", Addison-Wesley Publishing Company Inc., Reading, Mass., 1970, P.173.
69. E.T. Turkdogan, in the Proceedings of Intl. Conf. on Sulfide Inclusions in Steel, Port Chester, N.Y., Edited by J.J. deBarbadillo and E. Snape, American Society For Metals, 1974, P. 1-22.
70. K.A. Gschneidner, Jr., in Ref. 69, on Sulfide Inclusions in Steel, P.159.
71. R.E. Water, J.A. Charles and C. Lea, Metal Technology, May 1981, P.194.
72. E.O. Hall, Proc. Phys. Soc. B64 (1951) 747
73. P.N. Ross and B.H. Kear, "Rapid Solidification Processing", Proceedings of Intl. Conf. on Rapid Solidification Processing (1977) Claitor's Publishing Division, P.278.
74. L. Anand and J. Gurland, Met. Trans. Vol.6A, (1975) 928.
75. G.B. Olson, A.A. Anctil, T.S. Desisto and E.B. Kula, Met. Trans. Vol.14A, August 1983, P.1661.

76. C.F. Hickey, Jr. and Albert A. Anctil, "Split Heat Mechanical Property Comparison of ESR and VAR 4340 Steel", report number TR83-27, Army Materials and Mechanics Research Center, Watertown, Massachusetts.

TABLE 1: Chemical Analysis of Steels Investigated (Wt %).

<u>Chemical Element</u>	<u>M-2 Matrix Conventional VAR</u>	<u>M-2 Matrix XSR 118C RSP</u>	<u>M-50 Matrix Conventional VAR</u>	<u>M-50 Matrix XSR 273 RSP</u>
C	0.51	0.50	0.45	0.48
Mn	0.22	0.21	0.25	0.26
Si	0.18	0.19	0.26	0.27
Mo	2.72	2.72	3.03	3.03
Cr	4.46	4.53	3.88	3.81
V	1.03	0.99	0.31	0.33
P	0.012	0.014	0.002	0.003
S	0.0052	0.0055	0.0084	0.0094
O	12 ppm	155 ppm	20 ppm	70 ppm
N	108 ppm	94 ppm	12 ppm	14 ppm
W	2.10	1.99	---	---
Co	0.147	0.143	0.007	0.009
Cu	0.063	0.065	0.010	0.002
Ni	0.15	0.16	0.013	0.024
Al	0.001	0.002	0.017	0.023
Mg	0.0001	0.0022	0.0002	0.0003

TABLE 2: Extrusion Data for RSP Powders.

Steel	Run No.	Powder Size (mesh)	Extrusion Temperature	Reduction Ratio	Shape of Final Pieces
M-2 Matrix *	XSR 118	- 200	900°C	4 : 1	1 ⁵ / ₈ " x 5 ⁵ / ₈ " x 13 ¹ / ₂ "
	XSR 118 / 121	- 140	900°C	4 : 1	" "
	XSR 121	- 80 + 140	900°C	4 : 1	" "
M-50 Matrix **	XSR 273 /274	- 140	900°C	10 : 1	1 ¹ / ₅ " x 1 ¹ / ₂ " x 5 ¹ / ₄ "
	XSR 273 /274	- 80 + 140	900°C	10 : 1	" "

* Powders were blank-die compacted before hot extrusion.

** Hot pressing was conducted after hot extrusion.

TABLE 3 : Secondary Dendritic Arm Spacing of RSP Powders.

Steel	Powder Size mesh (μm)	Secondary Dendritic Arm Spacing (μm)	Estimated Cooling Rate ($^{\circ}\text{K}/\text{sec}$)
M-2 Matrix	-200 (< 75 μm)	1.4 - 1.1 μm	7.0×10^4 - 1.6×10^5
	-140 (< 106 μm)	1.6 - 1.2 μm	4.5×10^4 - 1.2×10^5
	-80+140 (106 ~ 180 μm)	1.9 - 1.7 μm	3.0×10^4 - 4.0×10^4
M-50 Matrix	-140 (< 106 μm)	1.6 - 1.2 μm	4.5×10^4 - 1.2×10^5
	-80+140 (106 ~ 180 μm)	1.9 - 1.6 μm	3.0×10^4 - 4.5×10^4

TABLE 4: Dispersed Phases In RSP M-2 Matrix Steel After One-hour Austenitizing at Indicated Temperatures.

(STEM Analysis)

Austenitizing Temperature	Phase	Particle Size	d
1180°C/1 hr.	MnS	0.1-0.6µm	0.20µm
	VS	0.1-0.6µm	0.19µm
	SiO ₂	0.1-0.5µm	0.16µm
	MgO - SiO ₂	0.1-0.6µm	0.18µm
	SiO ₂ - VS	0.15-0.6µm	0.23µm
	SiO ₂ - MnS	0.15-0.6µm	0.22µm
1220°C/1 hr.	SiO ₂	0.1-0.6µm	0.18µm
	MgO - SiO ₂	0.1-0.6µm	0.21µm
	SiO ₂ - VS	0.2-0.6µm	0.25µm
	SiO ₂ - MnS	0.2-0.6µm	0.24µm
1260°C/1 hr.	SiO ₂	0.1-0.6µm	0.20µm
	MgO - SiO ₂	0.1-0.7µm	0.21µm
	SiO ₂ - VS	0.2-0.7µm	0.26µm
	SiO ₂ - MnS	0.2-0.7µm	0.26µm

TABLE 5: Dispersed phases in Conventional (VAR)
M-2 Matrix Steel After One-hour Austenitizing
at Indicated Temperatures.

(STEM and SEM Analysis)

Austenitizing Temperature	Phase	Particle Size	\bar{d}
1180°C/1hr.	MnS	0.2 - 3.5 μm	1.0 μm
	SiO ₂	0.2 - 6.5 μm	1.5 μm
	(V,W,Mo,Cr) C Vanadium-rich carbide	0.8 - 9.0 μm	2.2 μm
1220°C/1hr.	MnS	0.5 - 4.0 μm	1.2 μm
	SiO ₂	0.3 - 8.0 μm	1.9 μm
	(V,W,Mo,Cr) C Vanadium-rich carbide	1.5 - 9.5 μm	2.7 μm
1260°C/1hr.	SiO ₂	0.5 - 10.5 μm	2.5 μm

TABLE 6 : Dispersed Phases In RSP M-50 Matrix Steel After One-hour Austenitizing at Indicated Temperatures .

(STEM Analysis)

Austenitizing Temperature	Phase	Particle Size	d
1180°C/1 hr.	MnS	0.1-0.6µm	0.22µm
	VS	0.1-0.6µm	0.23µm
	Al ₂ O ₃	0.1-0.5µm	0.18µm
	SiO ₂	0.1-0.5µm	0.17µm
	Al ₂ (O,S) ₃	0.1-0.5µm	0.16µm
	Al ₂ O ₃ - SiO ₂	0.1-0.6µm	0.23µm
	Al ₂ O ₃ - MnS	0.2-0.6µm	0.25µm
	Al ₂ O ₃ - VS	0.2-0.6µm	0.24µm
1220°C/1 hr.	MnS	0.1-0.6µm	0.25µm
	VS	0.1-0.6µm	0.26µm
	Al ₂ O ₃	0.1-0.6µm	0.20µm
	SiO ₂	0.1-0.6µm	0.19µm
	Al ₂ (O,S) ₃	0.1-0.6µm	0.18µm
	Al ₂ O ₃ - SiO ₂	0.1-0.7µm	0.25µm
	Al ₂ O ₃ - MnS	0.2-0.7µm	0.26µm
	Al ₂ O ₃ - VS	0.2-0.7µm	0.26µm
1260°C/1 hr.	Al ₂ O ₃	0.1-0.6µm	0.23µm
	SiO ₂	0.1-0.6µm	0.23µm
	Al ₂ (O,S) ₃	0.1-0.7µm	0.21µm
	Al ₂ O ₃ - SiO ₂	0.2-0.8µm	0.28µm
	Al ₂ O ₃ - MnS	0.2-0.8µm	0.29µm
	Al ₂ O ₃ - VS	0.2-0.8µm	0.28µm

TABLE 7 : Dispersed Phases In Conventional (VAR) M-50 Matrix Steel
After One-hour Austenitizing at Indicated Temperatures.

(STEM and SEM Analysis)

Austenitizing Temperature	Phase	Particle Size	\bar{d}
1180°C/1hr.	MnS	0.2 -1.6 μm	0.6 μm
	VS	0.05-0.5 μm	0.3 μm
	SiO ₂	0.05-0.6 μm	0.4 μm
	Al ₂ O ₃	0.25-2.5 μm	1.0 μm
	Al ₂ (O,S) ₃	0.2 -1.5 μm	0.9 μm
	Al ₂ O ₃ - SiO ₂	0.7 -5.5 μm	2.0 μm
1220°C/1hr.	MnS	0.2 -1.5 μm	0.6 μm
	VS	0.05-0.5 μm	0.3 μm
	SiO ₂	0.05-0.6 μm	0.4 μm
	Al ₂ O ₃	0.3 -2.4 μm	1.1 μm
	Al ₂ (O,S) ₃	0.2 -1.4 μm	0.9 μm
	Al ₂ O ₃ - SiO ₂	0.7 -6.5 μm	2.2 μm
1260°C/1hr.	SiO ₂	0.05-0.7 μm	0.5 μm
	Al ₂ O ₃	0.5 -2.8 μm	1.3 μm
	Al ₂ (O,S) ₃	0.3 -1.5 μm	1.0 μm
	Al ₂ O ₃ - SiO ₂	0.8 -7.5 μm	2.4 μm

Table 8: Comparison of Variables Considered in Existing Grain-Boundary Pinning Models.

MODEL	DRIVING FORCE	PINNING FORCE	EQUATION
Zener	$F_D = F(\sigma, \bar{D})$	$F_P = F(\sigma, \frac{\bar{d}}{f_v})$	$\bar{D} = \frac{4}{3} \frac{\bar{d}}{f_v}$
Gladman	$F_D = F(\sigma, \bar{D}, Z)$	$F_P = F(\sigma, \frac{\bar{d}}{f_v})$	$\bar{D} = \frac{\pi}{6} \frac{\bar{d}}{f_v} (\frac{3}{2} - \frac{2}{Z})$
Hellman-Hillert	$F_D = F(\sigma, \bar{D})$	$F_P = F(\sigma, \beta, \frac{\bar{d}}{f_v})$	$\bar{D} = \frac{4}{9\beta} \frac{\bar{d}}{f_v}$

σ : Interfacial energy of grain boundary

\bar{D} : Mean grain diameter

\bar{d} : Mean particle diameter

f_v : Volume fraction of particles

Z : Grain-size distribution parameter, $Z = \frac{D}{\bar{D}}$, D is the diameter of growing grain.

β : Boundary curvature correction, $\beta = 0.125 \ln(40 \frac{\rho}{r})$, $\rho = 6 \bar{R}$,
 \bar{R} is mean grain diameter and r is the radius of particle.

TABLE 9: Comparison of Measured and Calculated Austenitic Grain Size in RSP M-2 Matrix Steel; Equations (34) and (35).

Austenitizing Temperature	Mean Diameter of Dispersoids \bar{d} , μm	Volume Fraction of Dispersoids f_v	\bar{d} / f_v	$\frac{1}{\sum(f_i / d_i)}$	Austenitic Grain Diameter, \bar{D} , μm		
					Calculated with Eq. (35)	Calculated with Eq. (34)	Measured
1180°C/1hr.	0.19	3.7×10^{-3}	51	61	22	26	25
1220°C/1hr.	0.20	2.6×10^{-3}	77	97	33	42	40
1260°C/1hr.	0.24	2.2×10^{-3}	109	139	47	60	55

$$\text{Eqn. (34)} \quad \bar{D} = \frac{4}{3\alpha} \left(\frac{3}{2} - \frac{2}{Z} \right) \sum \left(\frac{f_i}{d_i} \right)$$

$$\text{Eqn. (35)} \quad \bar{D} = \frac{4}{3\alpha} \left(\frac{3}{2} - \frac{2}{Z} \right) \frac{\bar{d}}{f_v}$$

$$\alpha = 1.0$$

$$Z = 1.7$$

TABLE 10: Comparison of Measured and Calculated Austenitic Grain Size in RSP M-50 Matrix Steel; Equations (34) and (35).

Austenitizing Temperature	Mean Diameter of Dispersoids \bar{d} , μm	Volume Fraction of Dispersoids f_v	\bar{d} / f_v	$\frac{1}{\sum (f_i / d_i)}$	Austenitic Grain Diameter, \bar{D} , μm		
					Calculated with Eqn. (35)	Calculated with Eqn. (34)	Measured
1180°C/1hr.	0.20	4.6×10^{-3}	43	56	19	24	25
1220°C/1hr.	0.22	3.3×10^{-3}	67	81	29	35	35
1260°C/1hr.	0.27	3.0×10^{-3}	90	116	39	50	50

$$\text{Eqn. (34)} \quad \bar{D} = \frac{4}{3\alpha} \left(\frac{3}{2} - \frac{2}{Z} \right) / \sum \left(\frac{f_i}{d_i} \right)$$

$$\text{Eqn. (35)} \quad \bar{D} = \frac{4}{3\alpha} \left(\frac{3}{2} - \frac{2}{Z} \right) \frac{\bar{d}}{f_v}$$

$$\alpha = 1.0$$

$$Z = 1.7$$

TABLE 11: K_{IC} Fracture Toughness of M-2 Matrix Steel.

Austenitizing Time : 1 hour
 Tempering Temperature : 565°C
 Tempering Time : 2+2 hours.

Steel Condition	Relative Density*	1100°C	1140°C	1180°C	1220°C	1260°C
Conventional (VAR)	1.0	23.1	24.9	23.0	22.7	21.9
RSP(As-Extruded)	99.79 %	22.9	25.6	23.9	25.2	27.2
RSP + HIPping at (1100°C/3hrs. 30Ksi)	99.83 %	23.1	22.4	21.4	20.9	19.8
RSP + Hot Rolling at 1100°C, (50% Reduction in Thickness)	99.86 %	22.7	27.3	22.8	25.2	24.8
RSP + HIPping + Hot Rolling at 1100°C	99.88 %	25.8	26.5	24.1	24.0	23.7

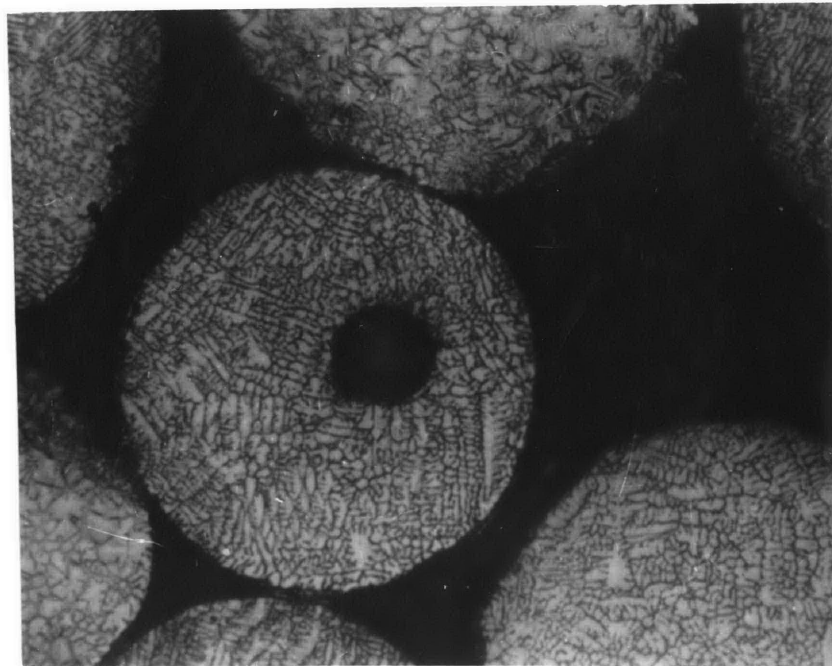
* Density of RSP Material Relative to Conventional VAR Material.

TABLE 12: K_{IC} Fracture Toughness of M-50 Matrix Steel.

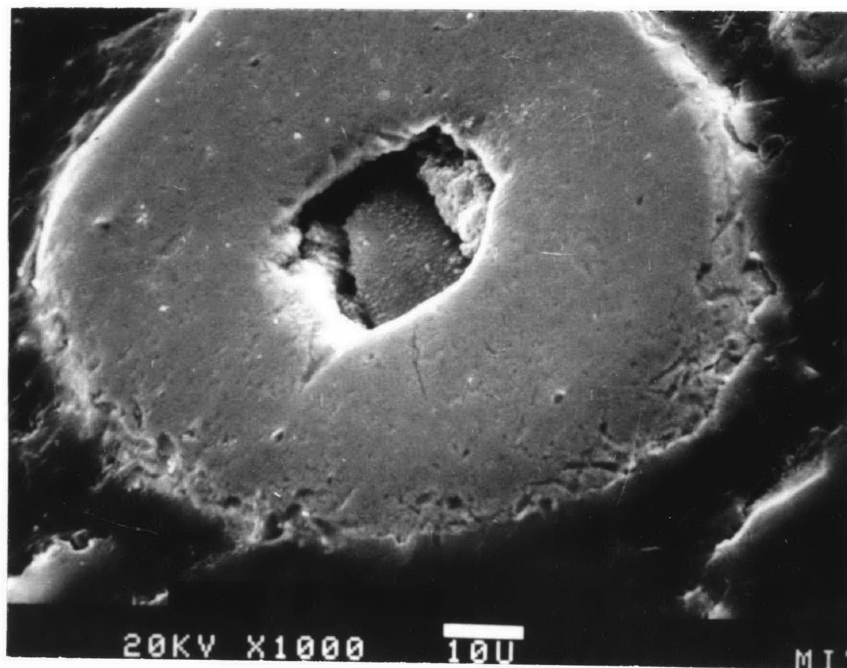
Austenitizing Time : 1 hour
 Tempering Temperature : 540°C
 Tempering Time : 2 + 2 + 2 hours

Steel Condition	Relative [*] Density	1100°C	1140°C	1180°C	1220°C	1260°C
Conventional (VAR)	1.0	45.1	41.5	42.5	40.1	38.9
RSP (As-Extruded)	99.65 %	36.9	38.0	37.9	38.7	35.6
RSP + HIPping at 1100°C/3hrs. 30Ksi	99.70 %	33.7	35.9	36.0	33.8	33.9
RSP + Hot Rolling at 1100°C, (50% Reduction in Thickness)	99.72 %	32.0	32.4	32.0	33.7	35.5
RSP + HIPping + Hot Rolling at 1100°C	99.76 %	37.0	35.6	36.2	36.4	37.1
RSP + Upset Forging at 1100°C (~ 75 % Red.)	99.78 %	37.9	36.9	36.5	35.9	36.3

* Density of RSP Material Relative to Conventional VAR Material.



(a)

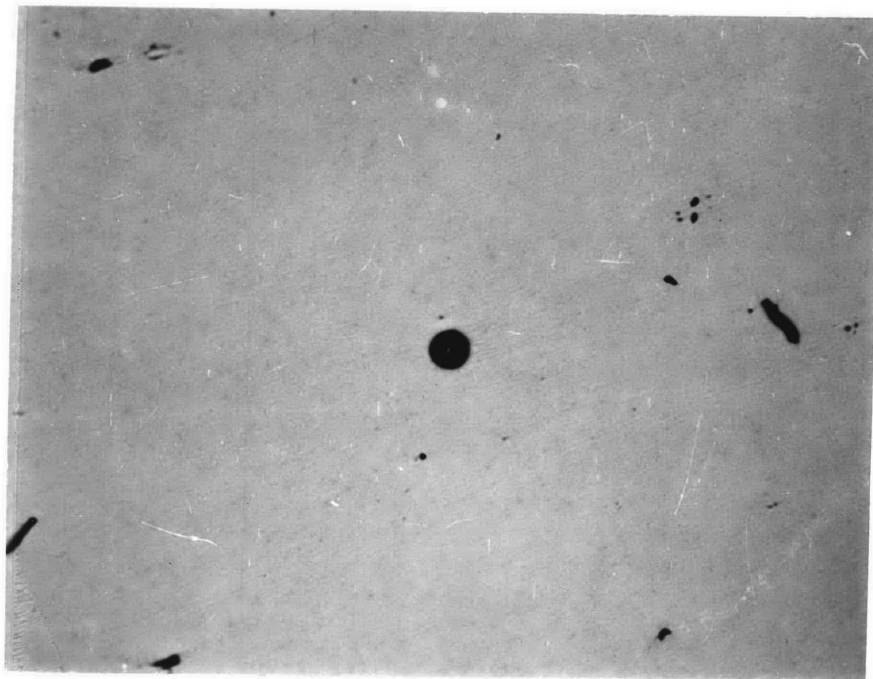
10 μm 

(b)

Figure 1. Optical Micrograph of As-Solidified RSP M-2 Matrix Steel Powders (a); (b) SEM Electron Micrograph of As-Solidified RSP M-50 Matrix Steel Powder.

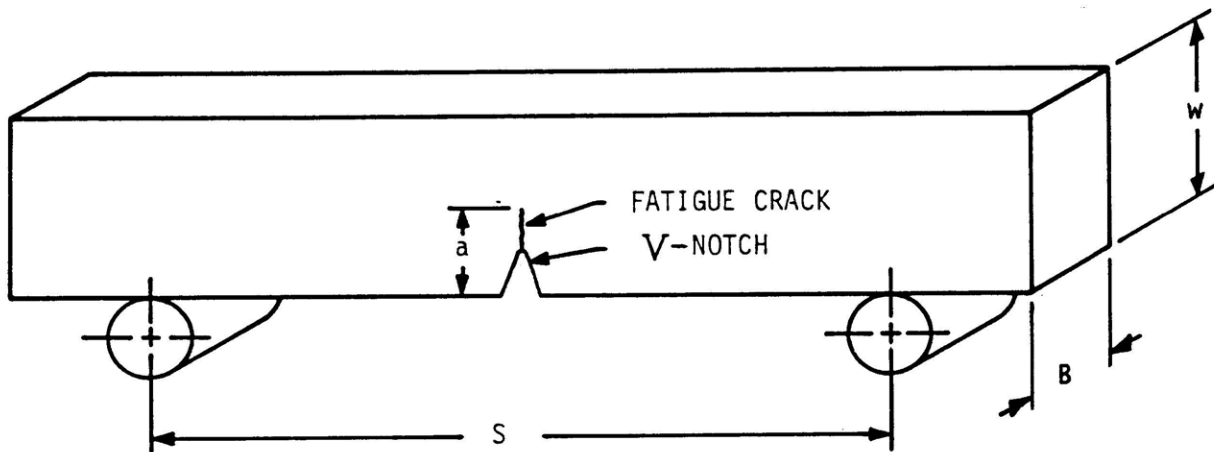


(a) 100 μm



(b)

Figure 2. Optical Micrograph of Hot-consolidated RSP Matrix Steels, As-Polished, (a) RSP M-2 Matrix Steel, (b) RSP M-50 Matrix Steel.



S = Span, 4.0 cm (1.575 in.)

w = Width or depth, 1.0 cm (0.394 in.)

B = Breadth or thickness, 0.5 cm (0.197 in.)

a = Total crack length

Figure 3. Geometry and Dimensions of Three-Point-Bend-Fracture Toughness Specimen.

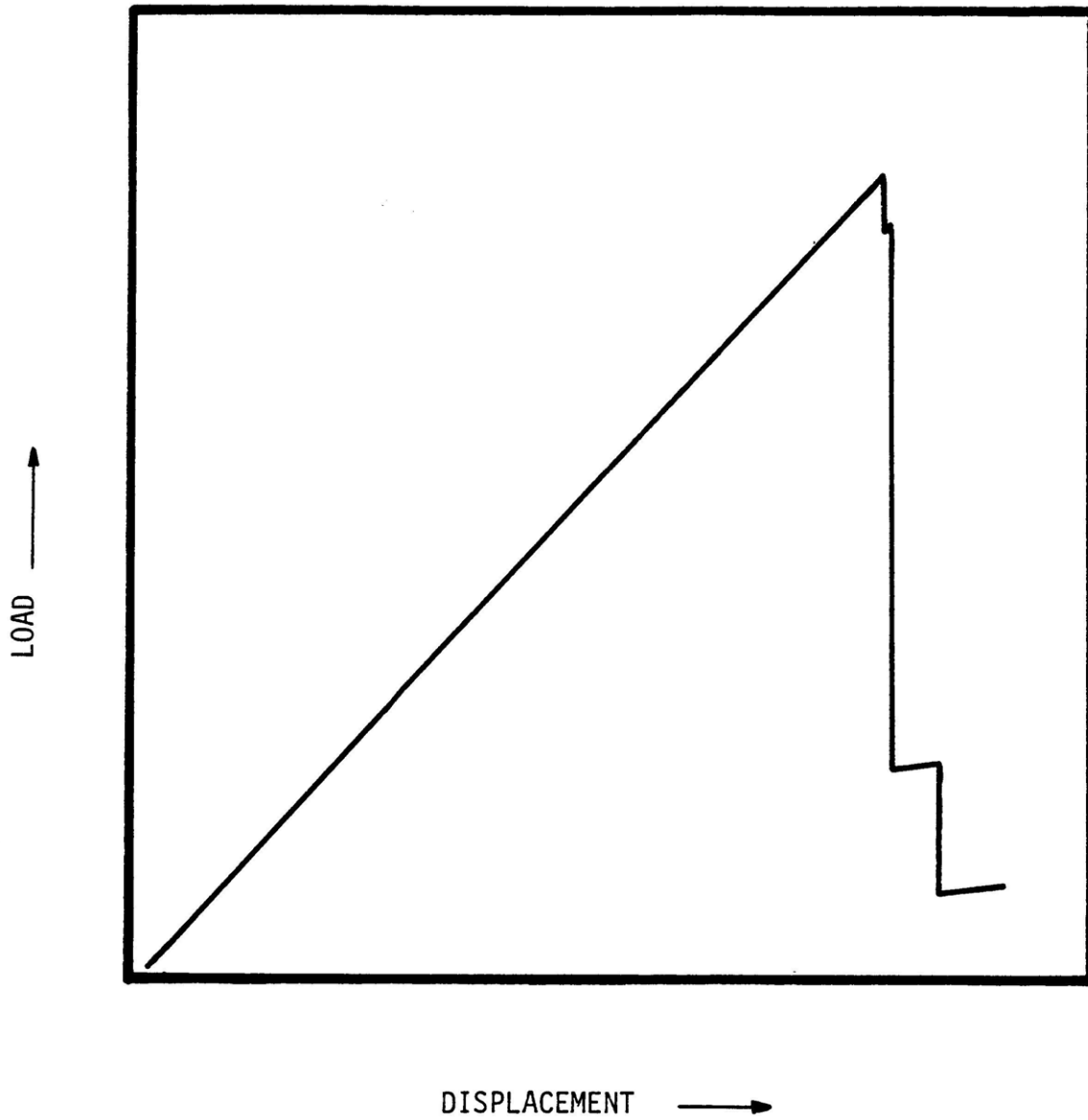


Figure 4 .Typical Load-Displacement Curve for Hardened-and-Tempered M-2 and M-50 Matrix Steels.

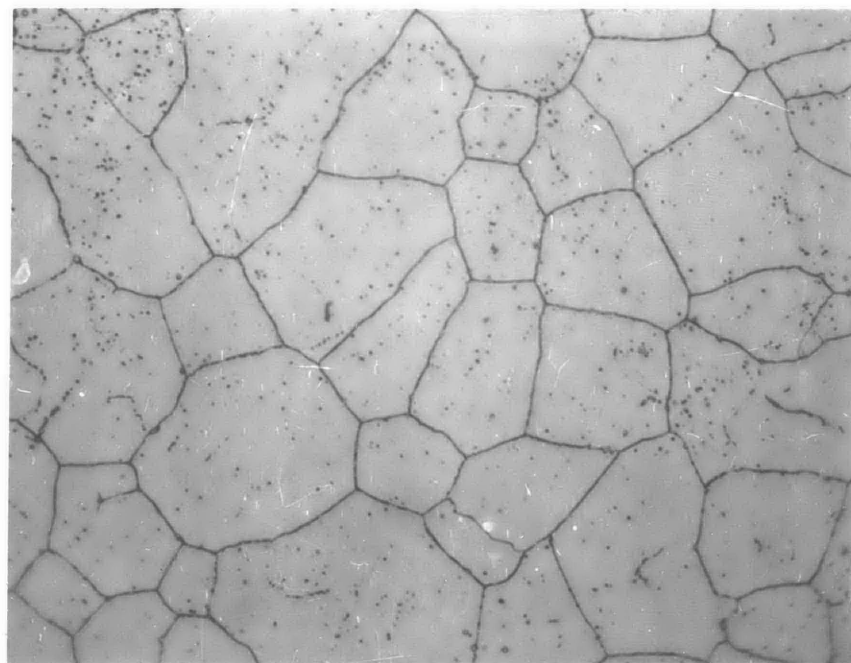
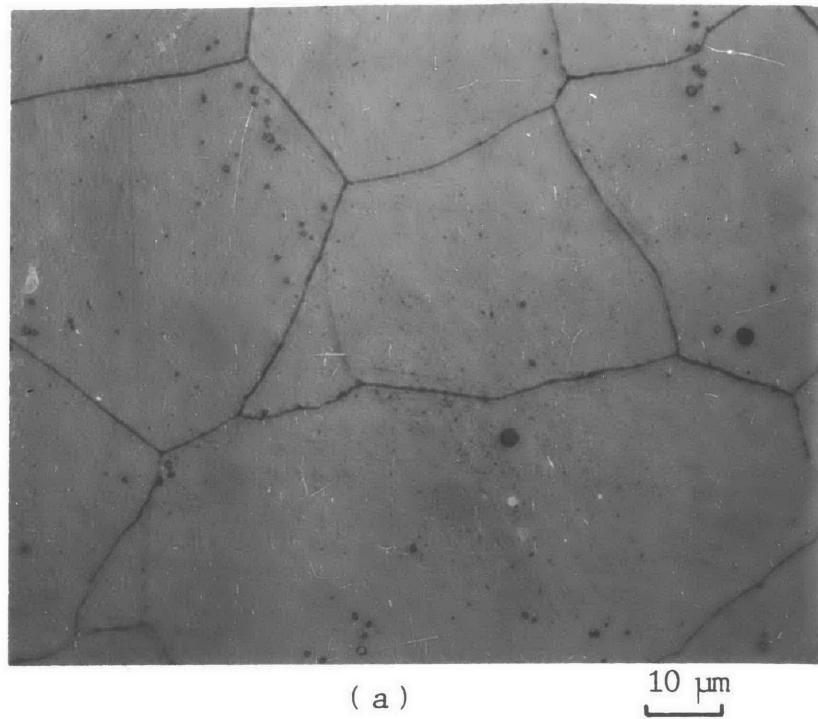
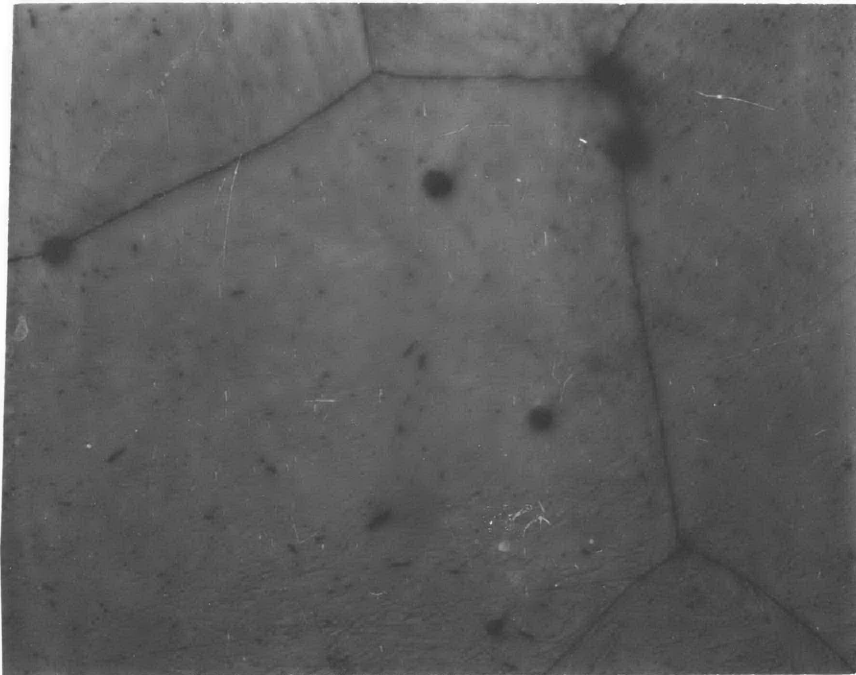
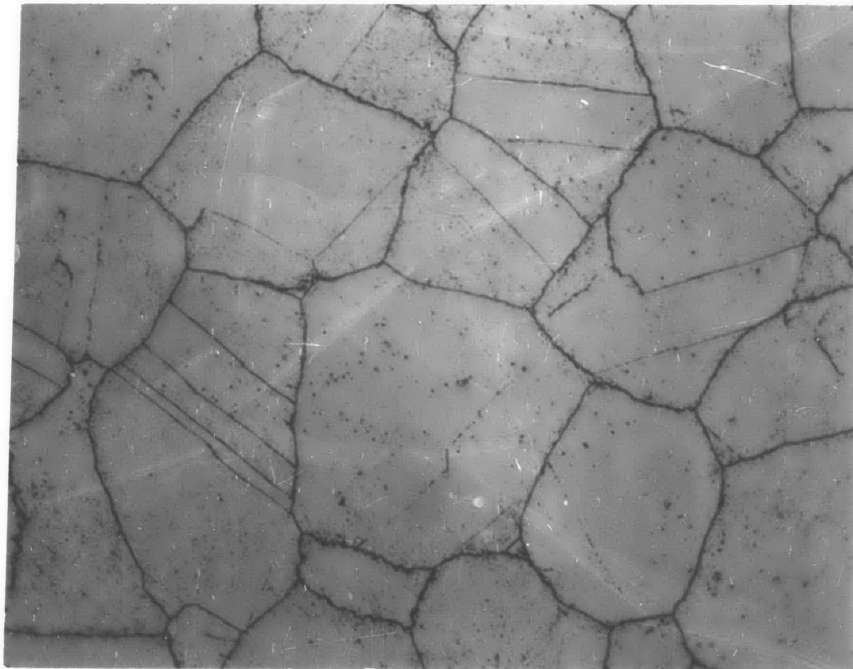


Figure 5. Optical Micrograph of M-2 Matrix Steel, (a) VAR, 1180°C/1hr. (b) RSP, 1180°C/1hr.



(c)

10 μm 

(d)

Figure 5. Continued- (c) VAR. 1220°C/1hr., (d) RSP. 1220°C/1hr.

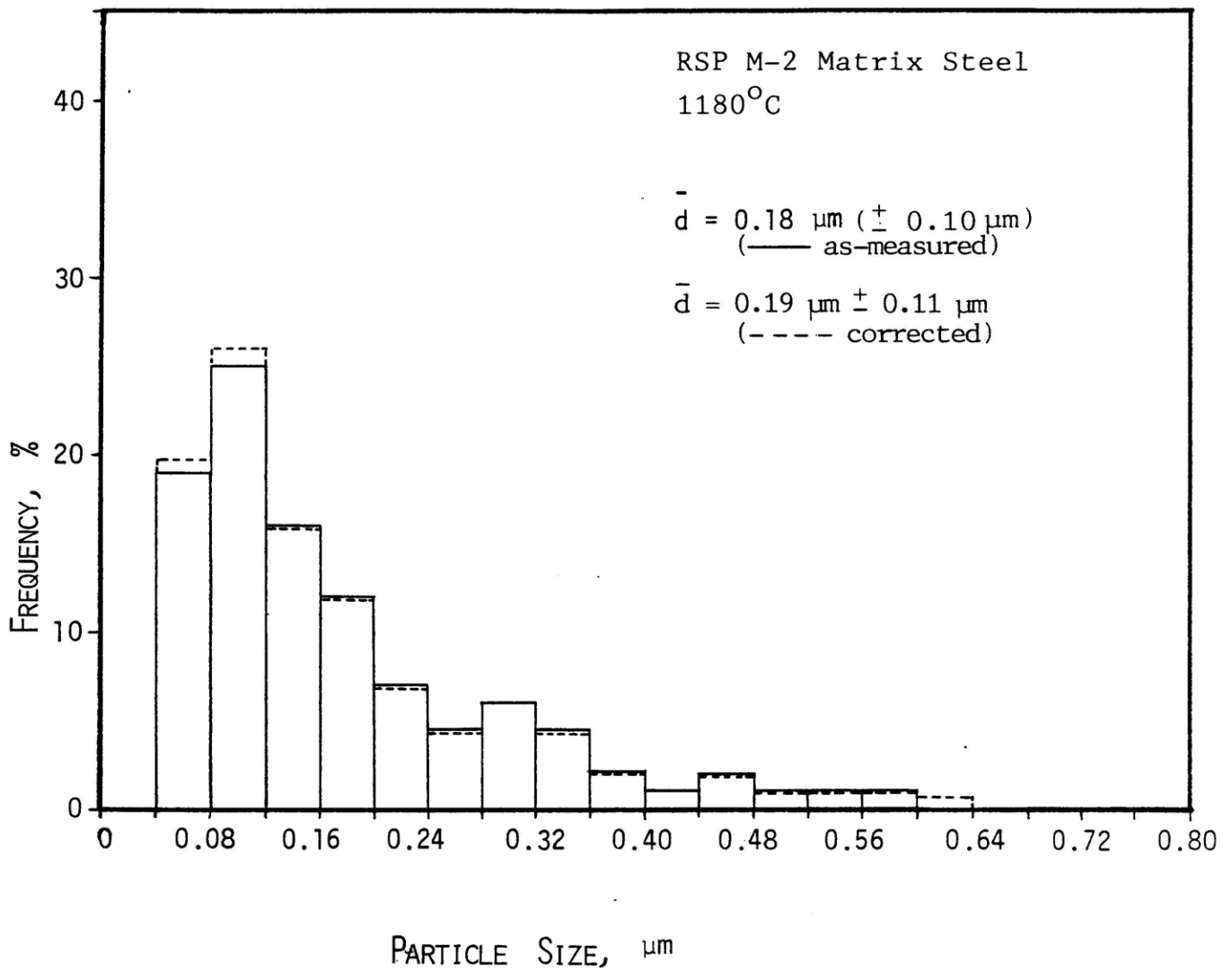


Figure 6: Particle-size Distribution of Second-phase precipitates in RSP M-2 Matrix Steel Austenitized at 1180°C for One Hour.

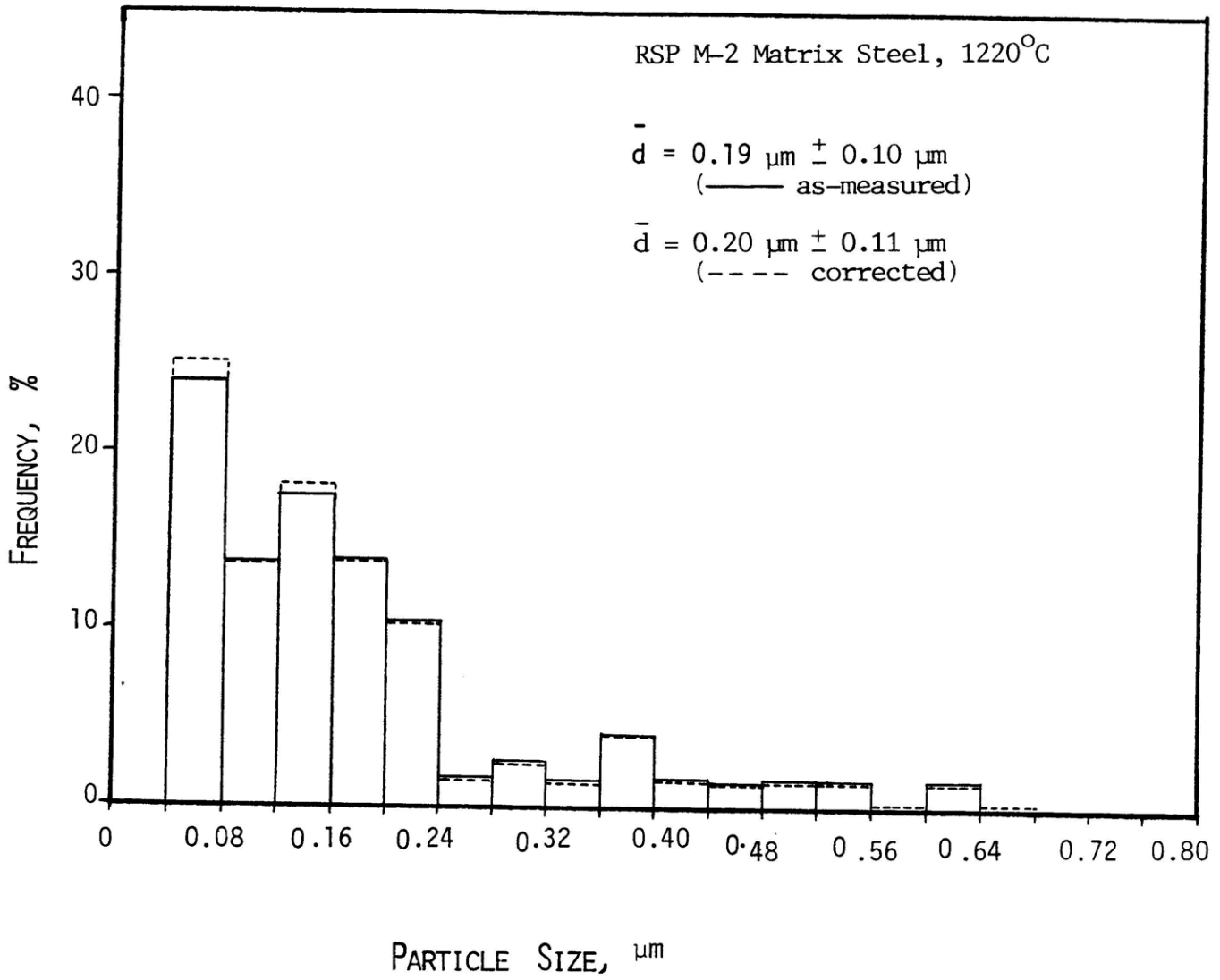


Figure 7: Particle-size Distribution of Second-phase Precipitates in RSP M-2 Matrix Steel Austenitized at 1220°C for One Hour.

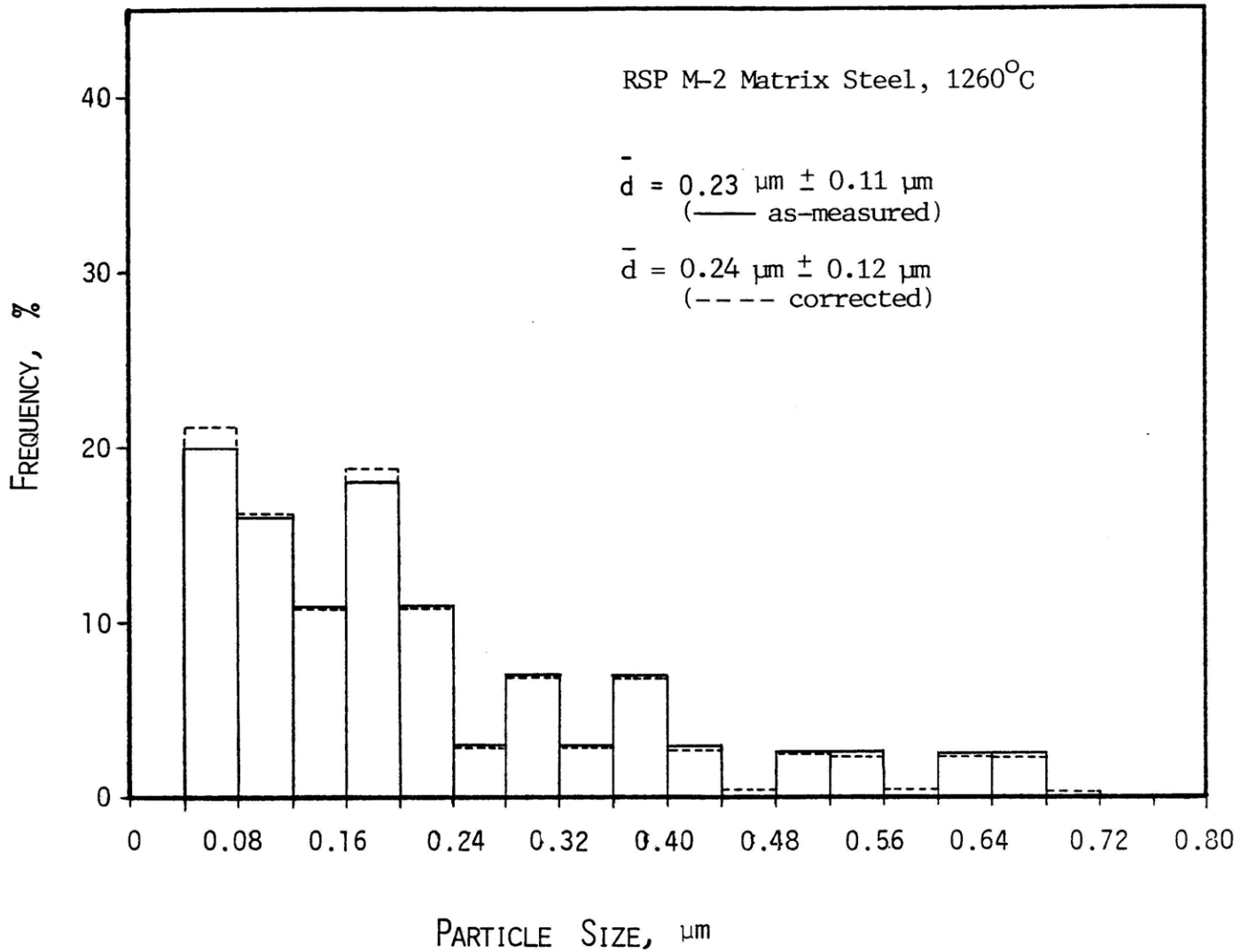


Figure 8: Particle-size Distribution of Second-phase Precipitates in RSP M-2 Matrix Steel Austenitized at 1260°C for One Hour.

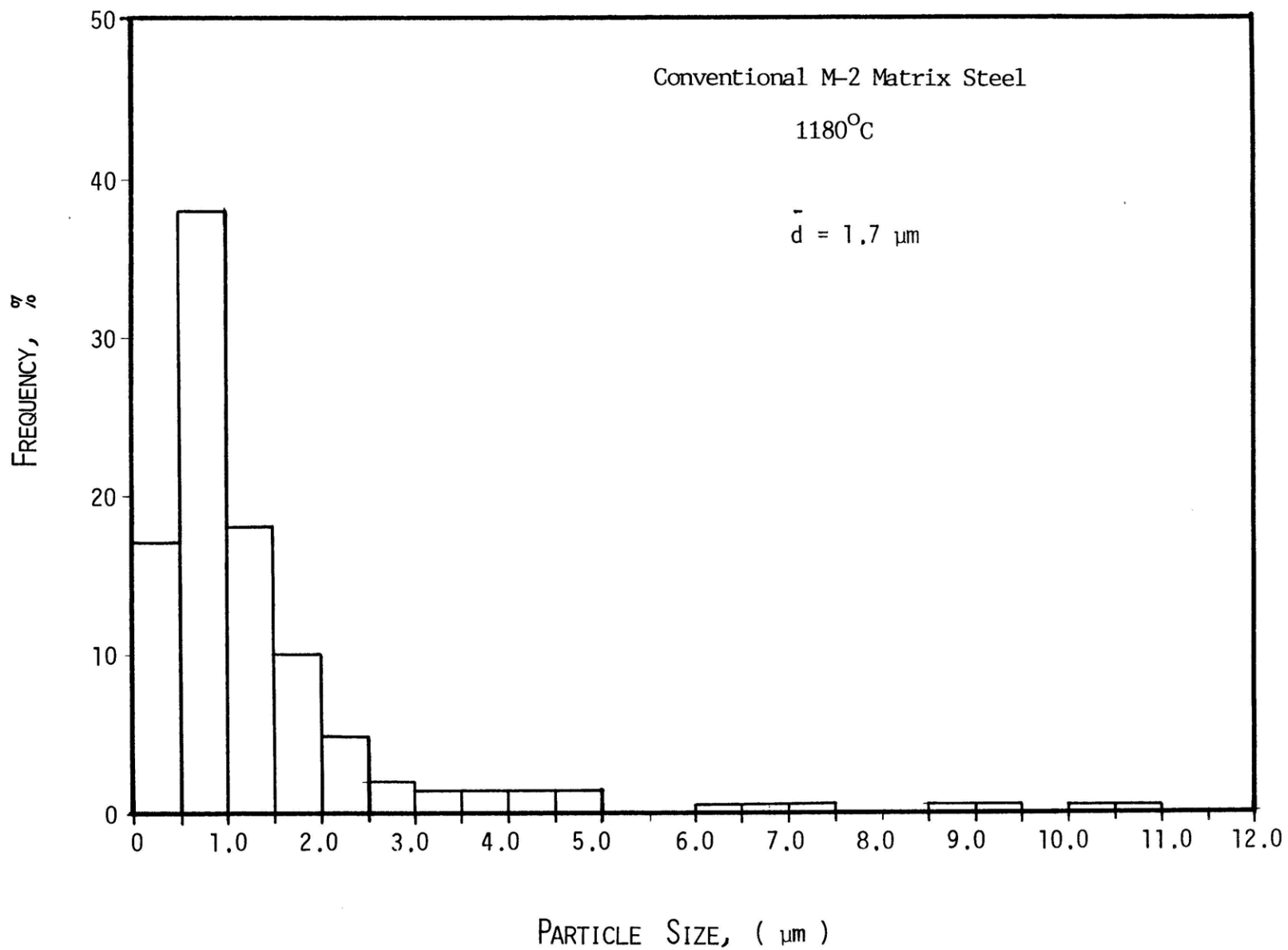


Figure 9: Particle-Size Distribution of Second-Phase Precipitates In Conventional M-2 Matrix Steel. (1180°C for 1 hr. treatment)

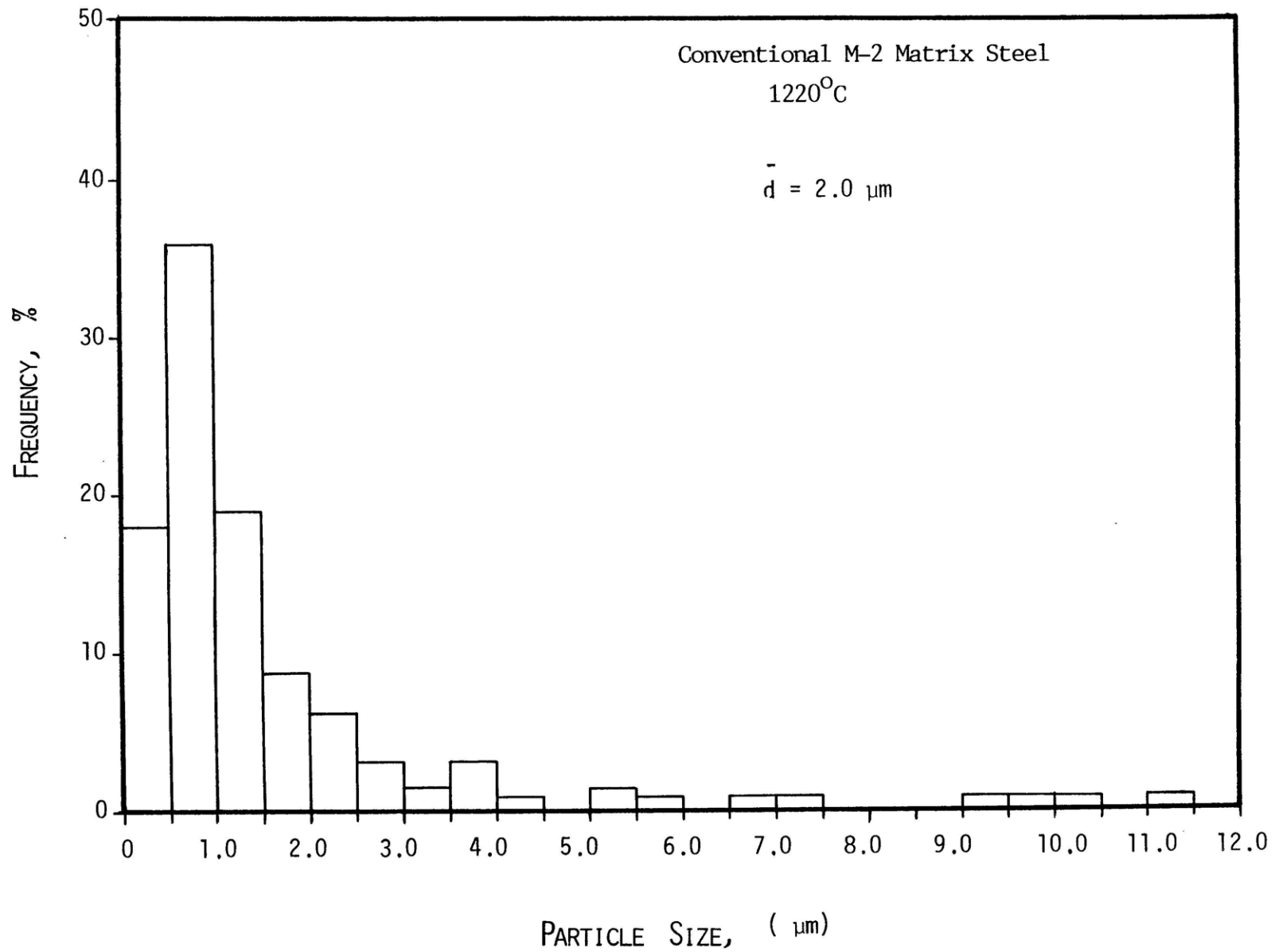


Figure 10: Particle-Size Distribution of Second-Phase Precipitates In Conventional M-2 Matrix Steel. (1220°C for 1 hr. treatment)

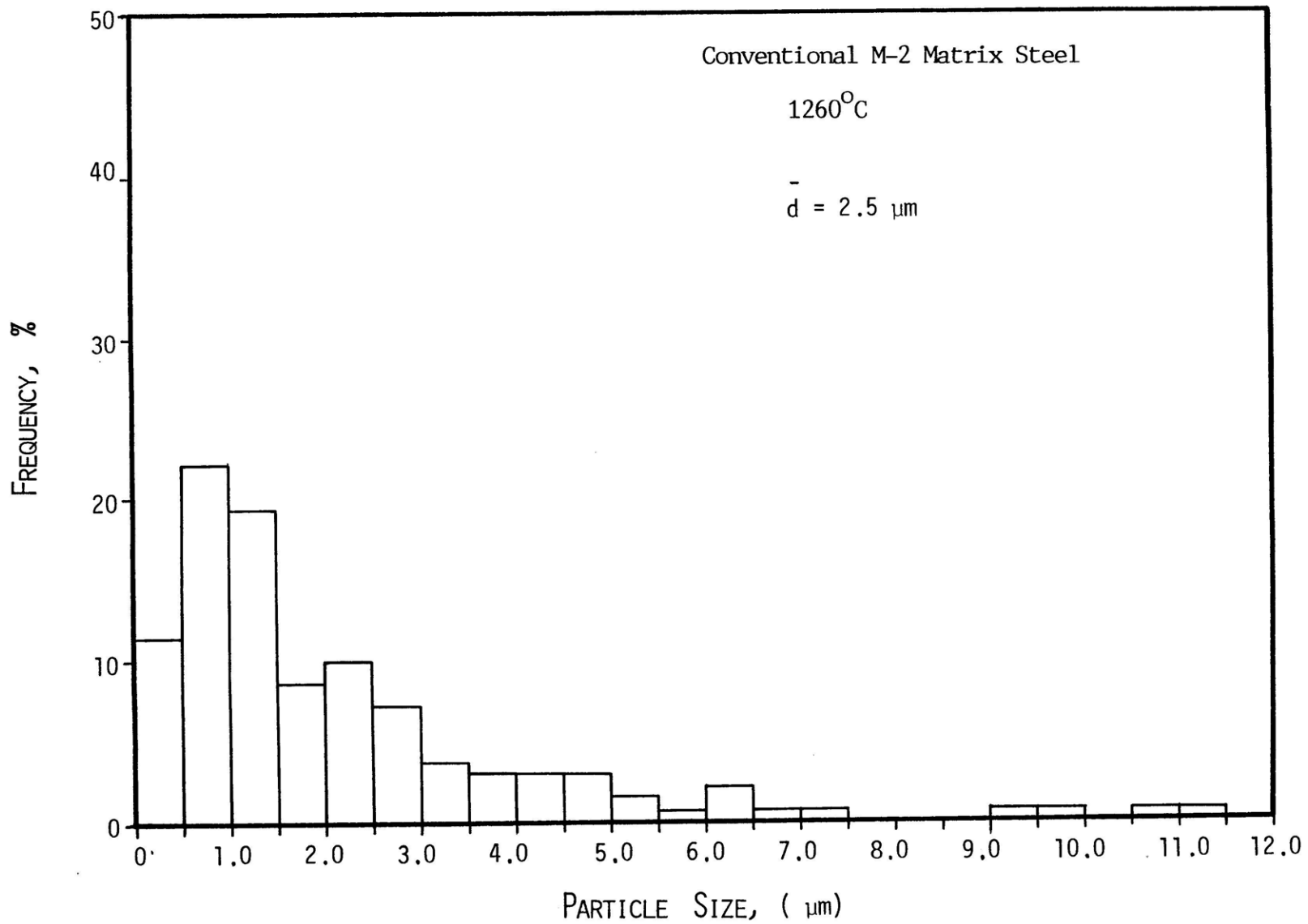
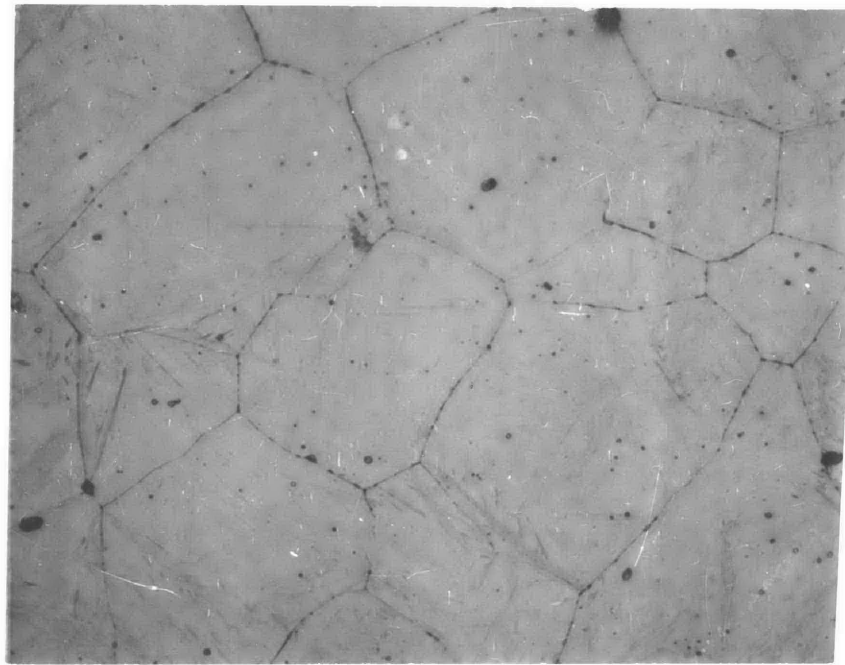
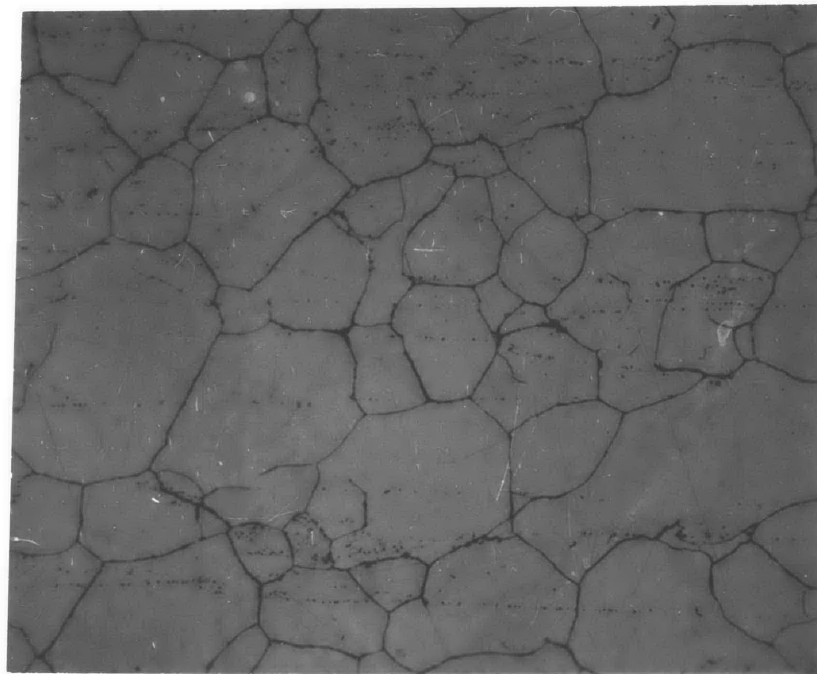


Figure 11: Particle-Size Distribution of Second-Phase Precipitates In Conventional M-2 Matrix Steel. (1260°C for 1 hr. treatment)

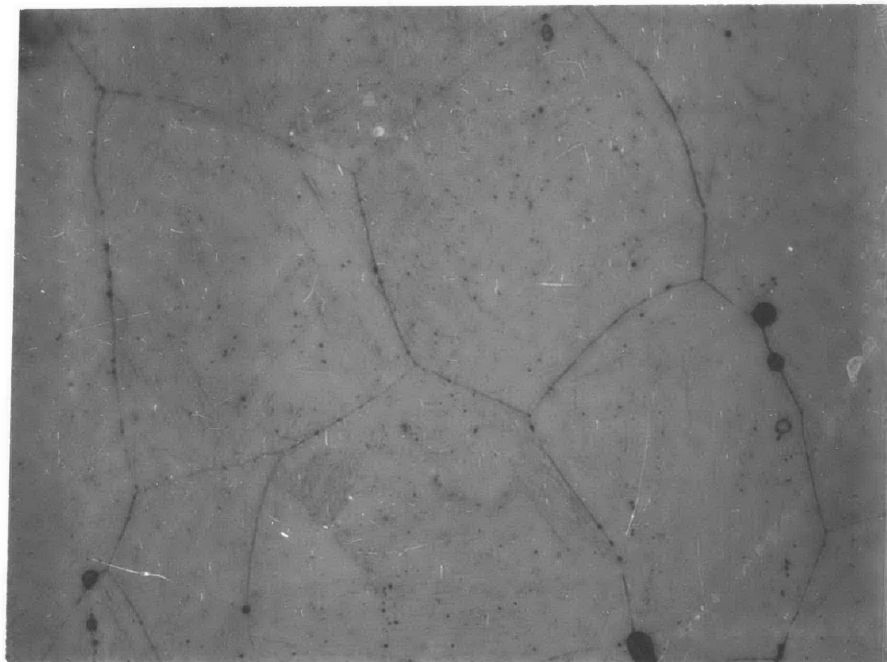


(a)

10 μm 

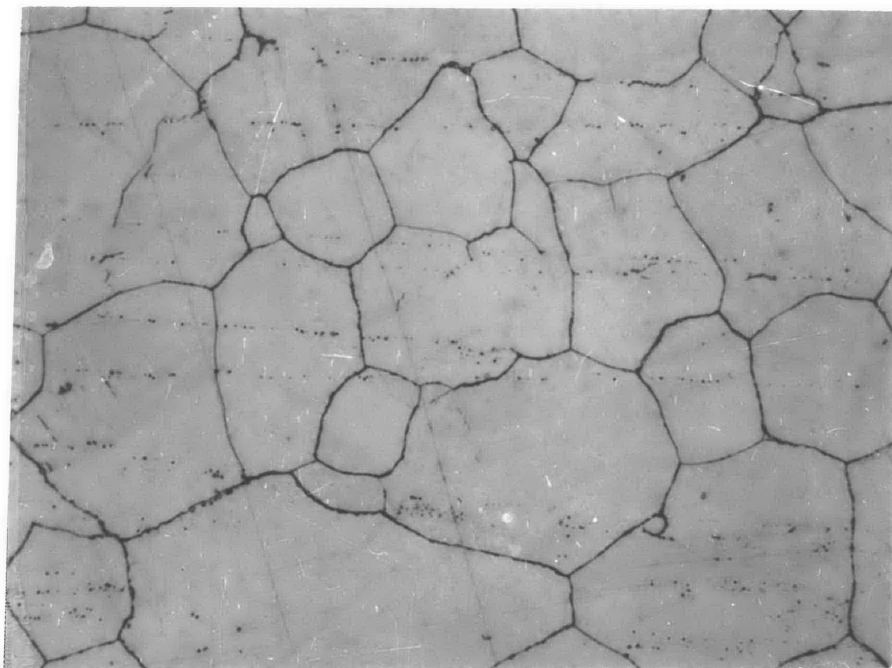
(b)

Figure 12. Optical Micrograph of M-50 Matrix Steel, (a) VAR. $1180^{\circ}\text{C}/1\text{hr.}$, (b) RSP. $1180^{\circ}\text{C}/1\text{hr.}$



(c)

10 μm



(d)

Figure 12. Continued, (c) VAR. 1220°C/1hr., (d) RSP. 1220°C/1hr.

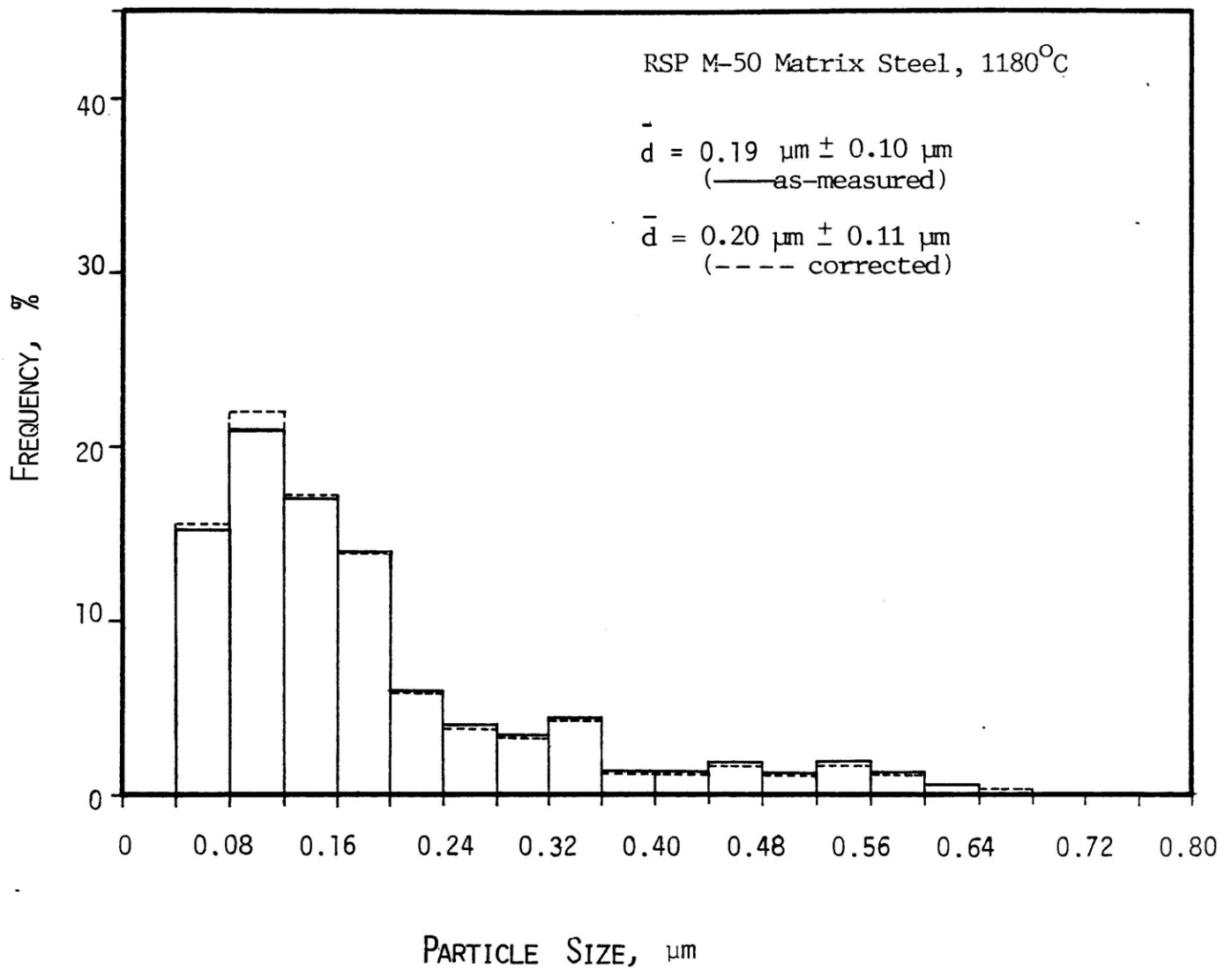


Figure 13: Particle-size Distribution of Second-Phase Precipitates in RSP M-50 Matrix Steel Austenitized at 1180°C for One Hour.

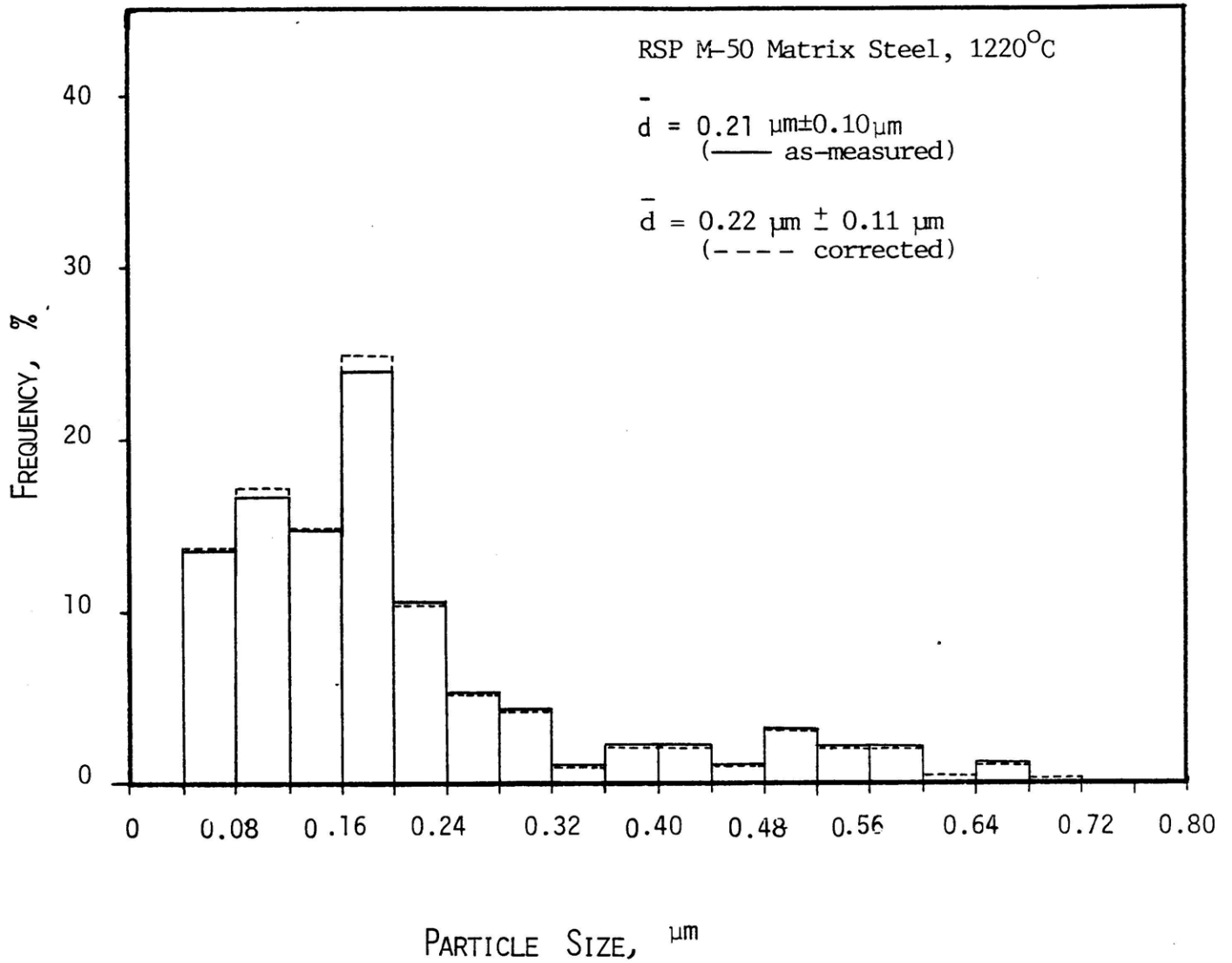


Figure 14: Particle-size Distribution of Second-phase Precipitates in RSP M-50 Matrix Steel Austenitized at 1220°C for One Hour.

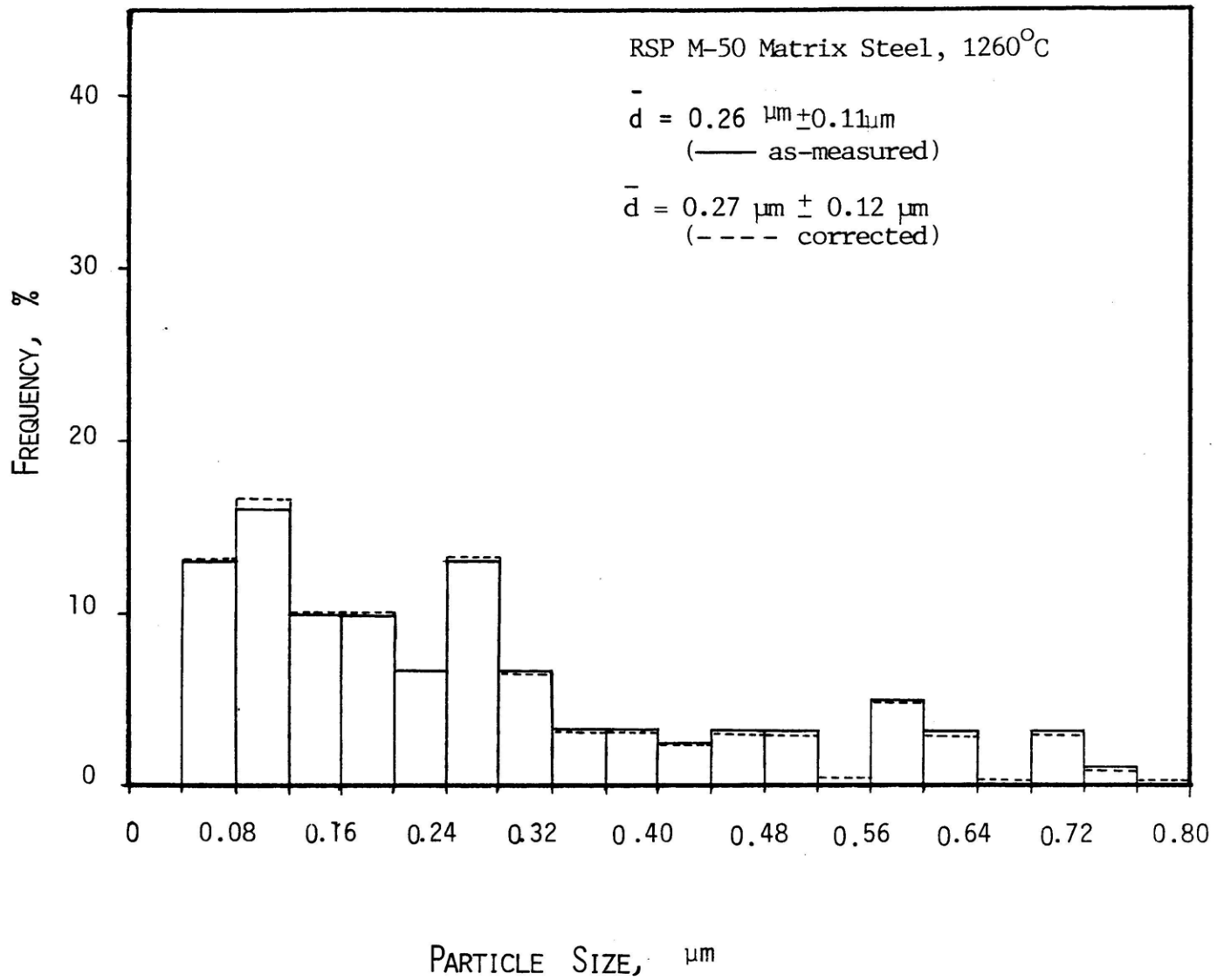


Figure 15: Particle-size Distribution of Second-phase Precipitates in RSP M-50 Matrix Steel Austenitized at 1260°C for One Hour.

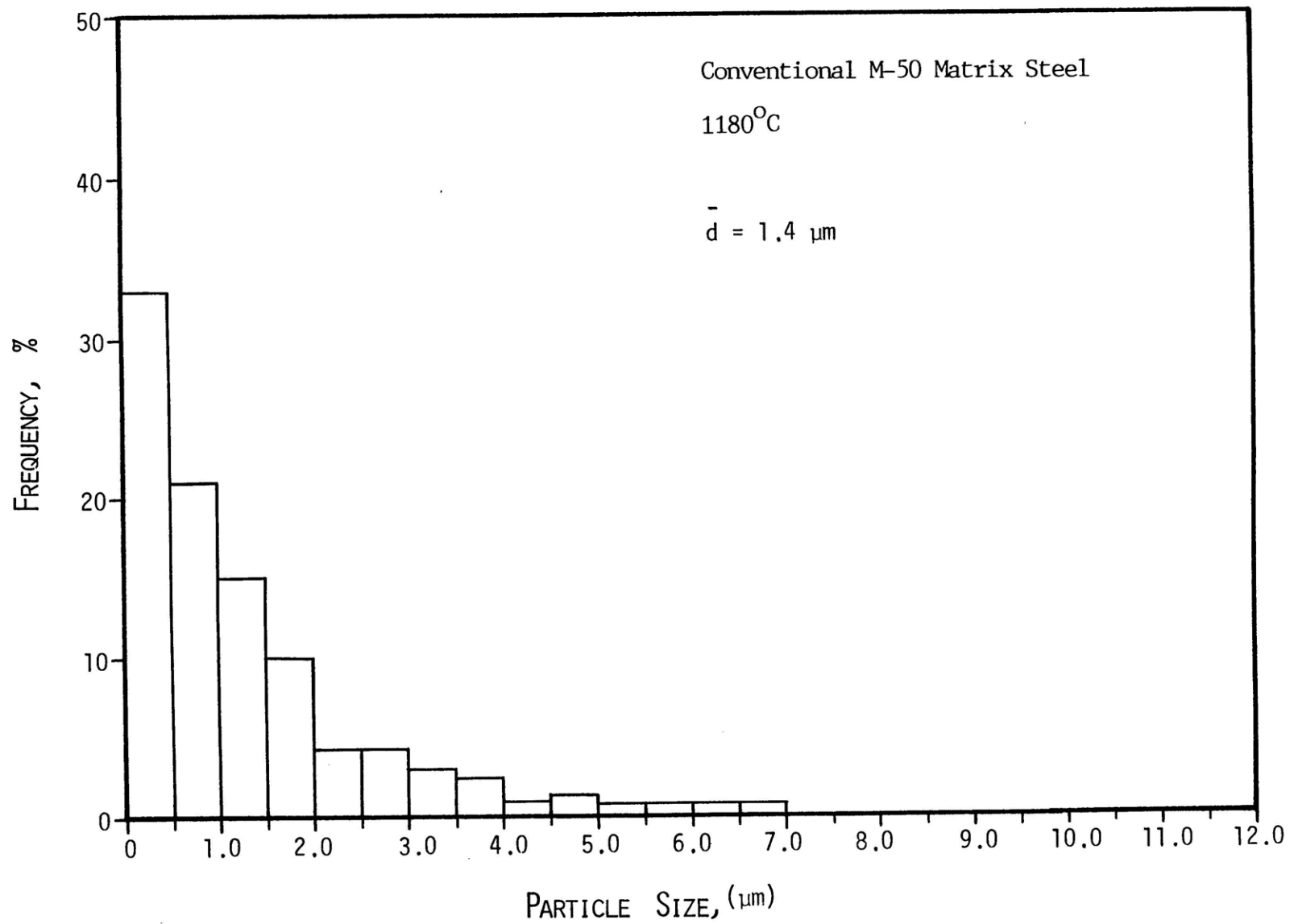


Figure 16 : Particle-Size Distribution of Second-Phase Precipitates In Conventional M-50 Matrix Steel. (1180°C for 1 hr. treatment)

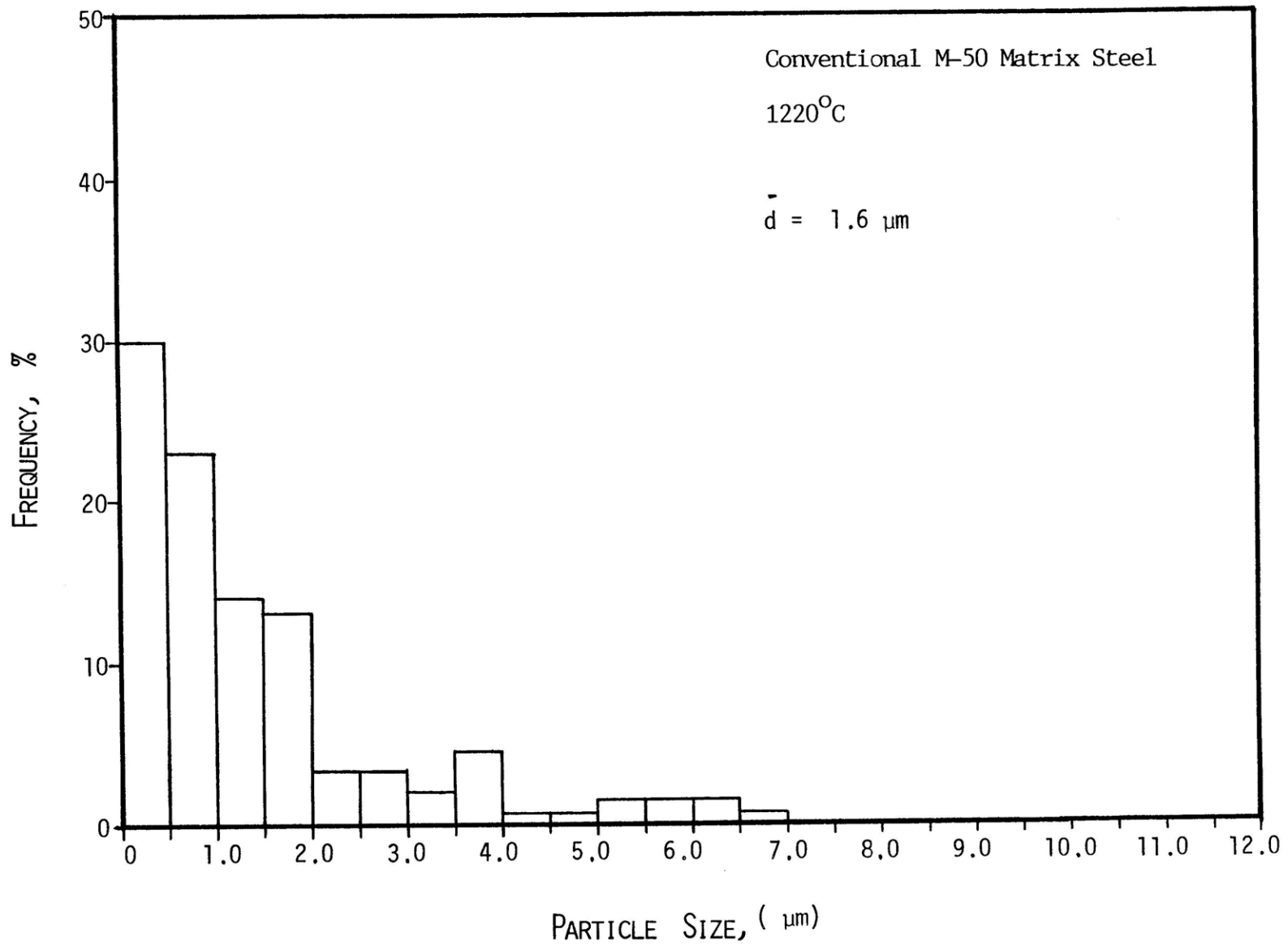


Figure 17: Particle-Size Distribution of Second-Phase Precipitates In Conventional M-50 Matrix Steel. (1220°C for 1 hr. treatment)

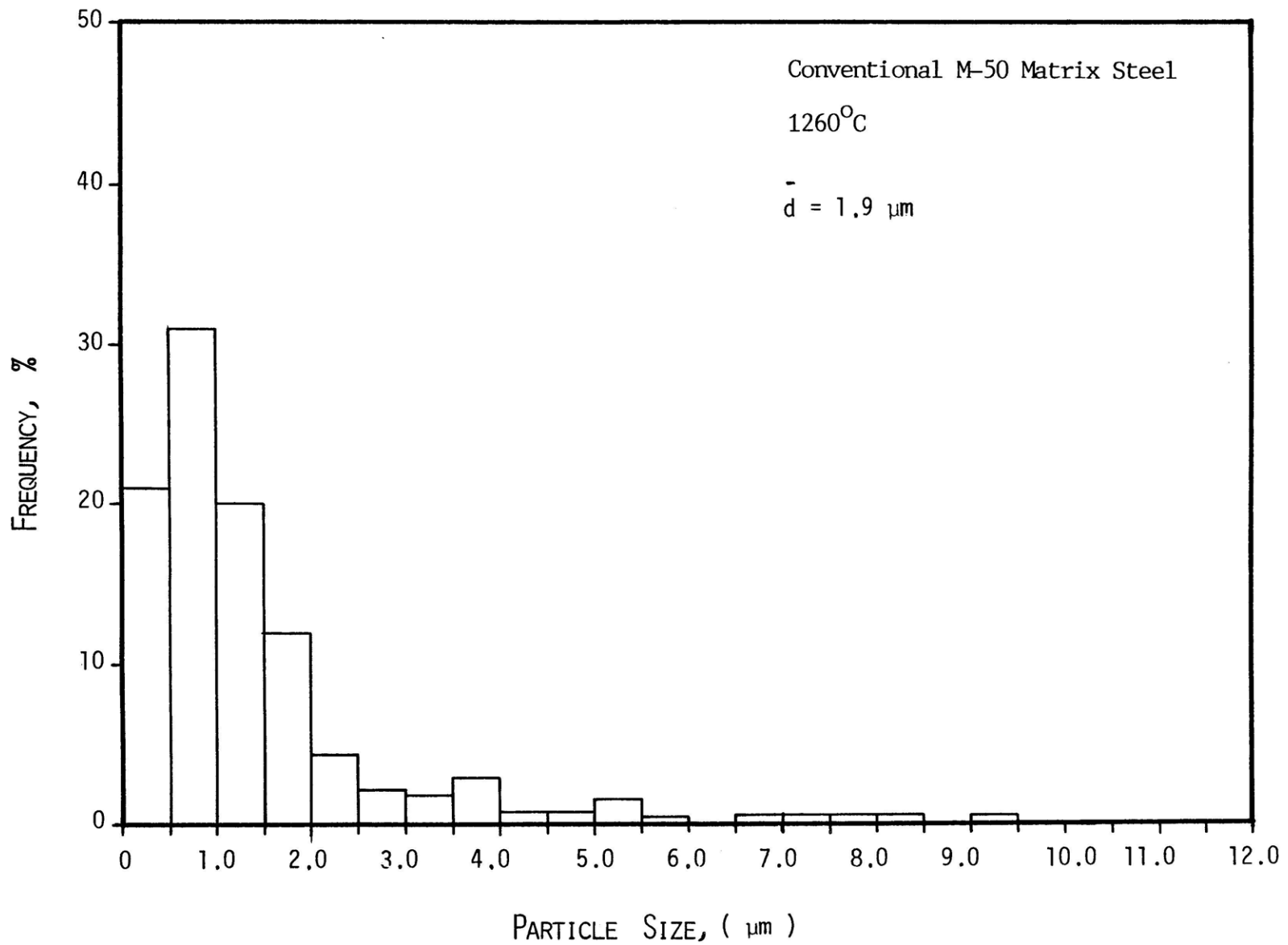


Figure 18 : Particle-Size Distribution of Second-Phase Precipitates In Conventional M-50 Matrix Steel. (1260°C for 1 hr. treatment)

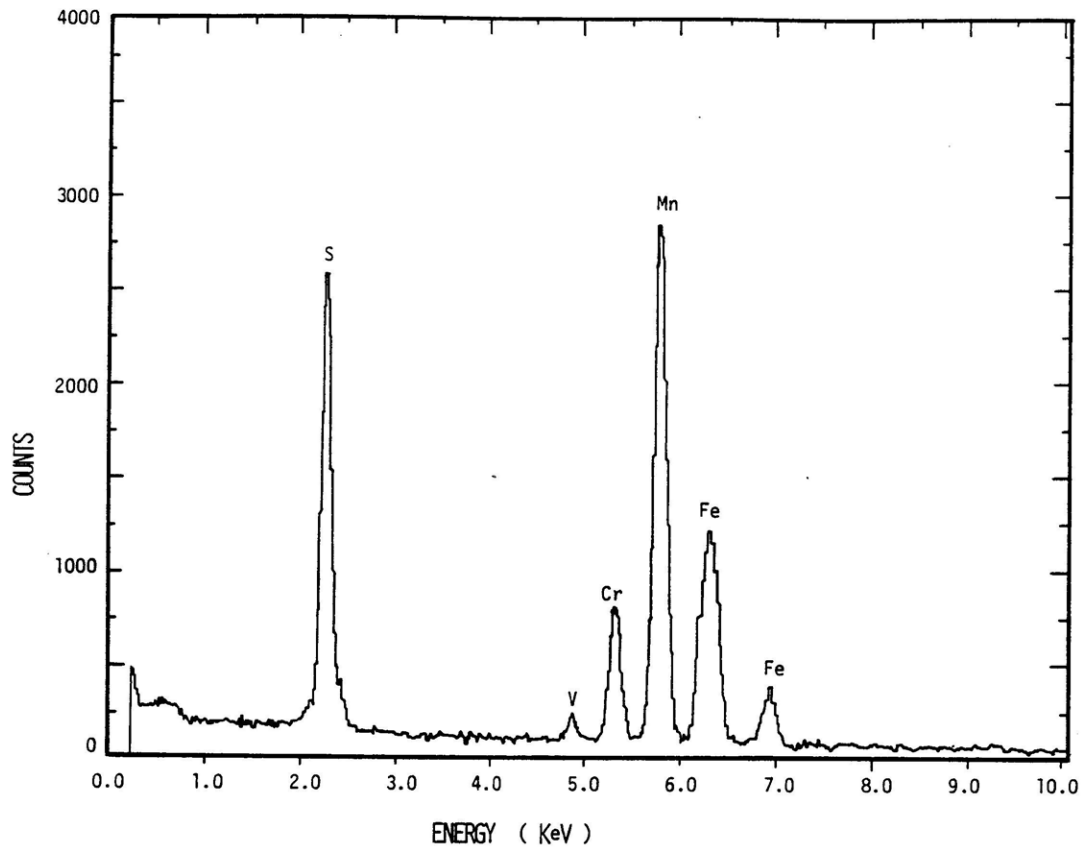


Figure 19(a). EDAX Spectrum of MnS.

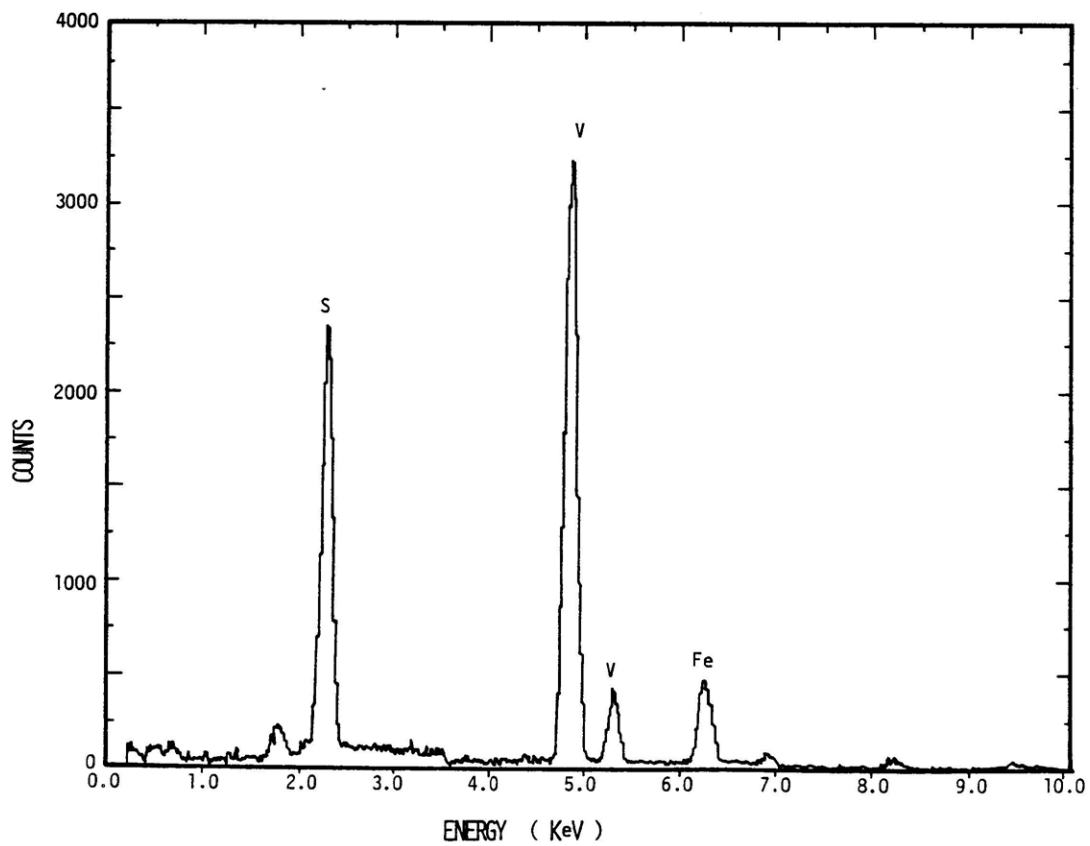


Figure 19(b). EDAX Spectrum of VS.

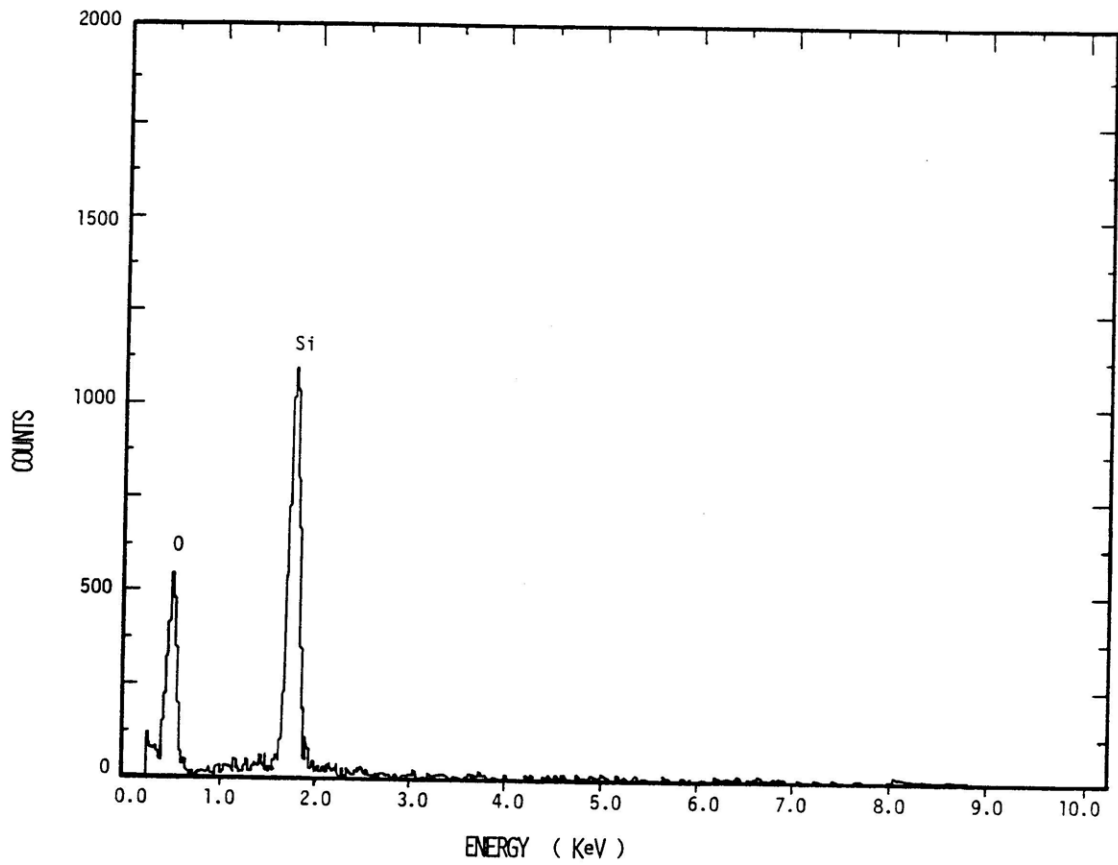


Figure 19(c). EDAX Spectrum of SiO₂.

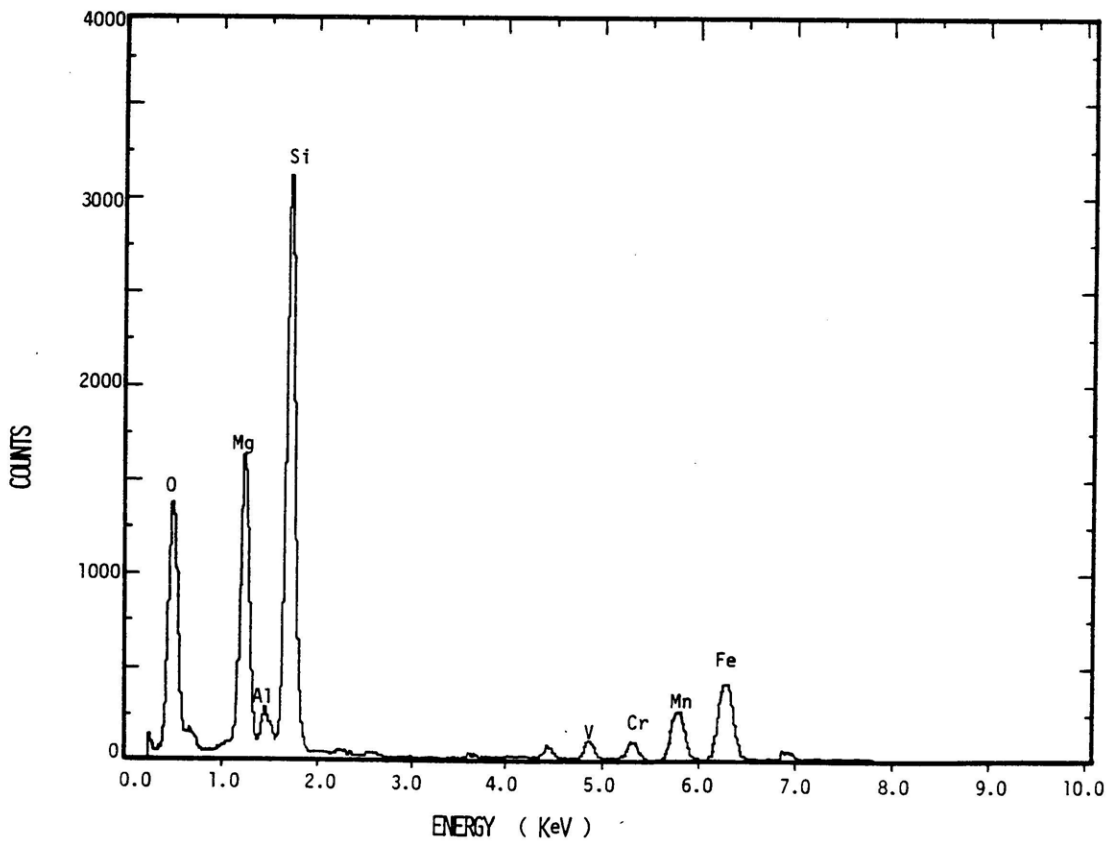


Figure 19 (d). EDAX Spectrum of Mg-Silicate(MgO-SiO₂).

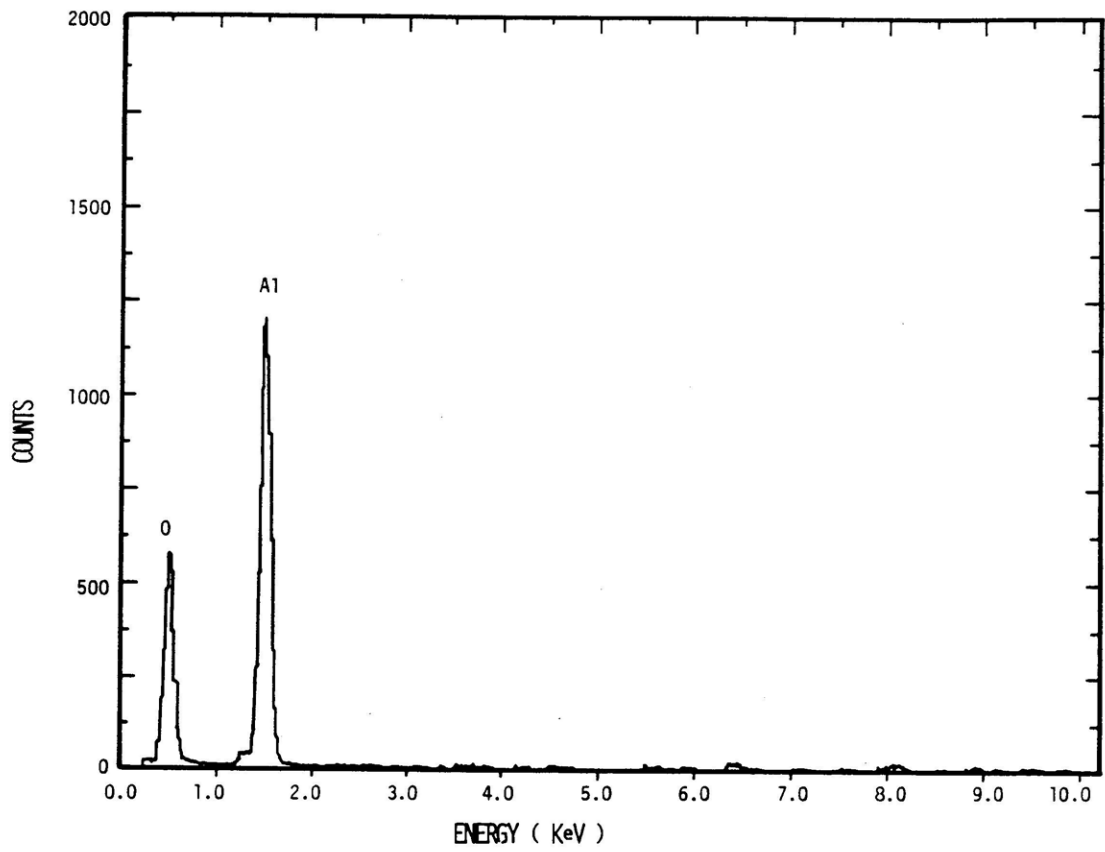


Figure 20(a). EDAX Spectrum of Al_2O_3 .

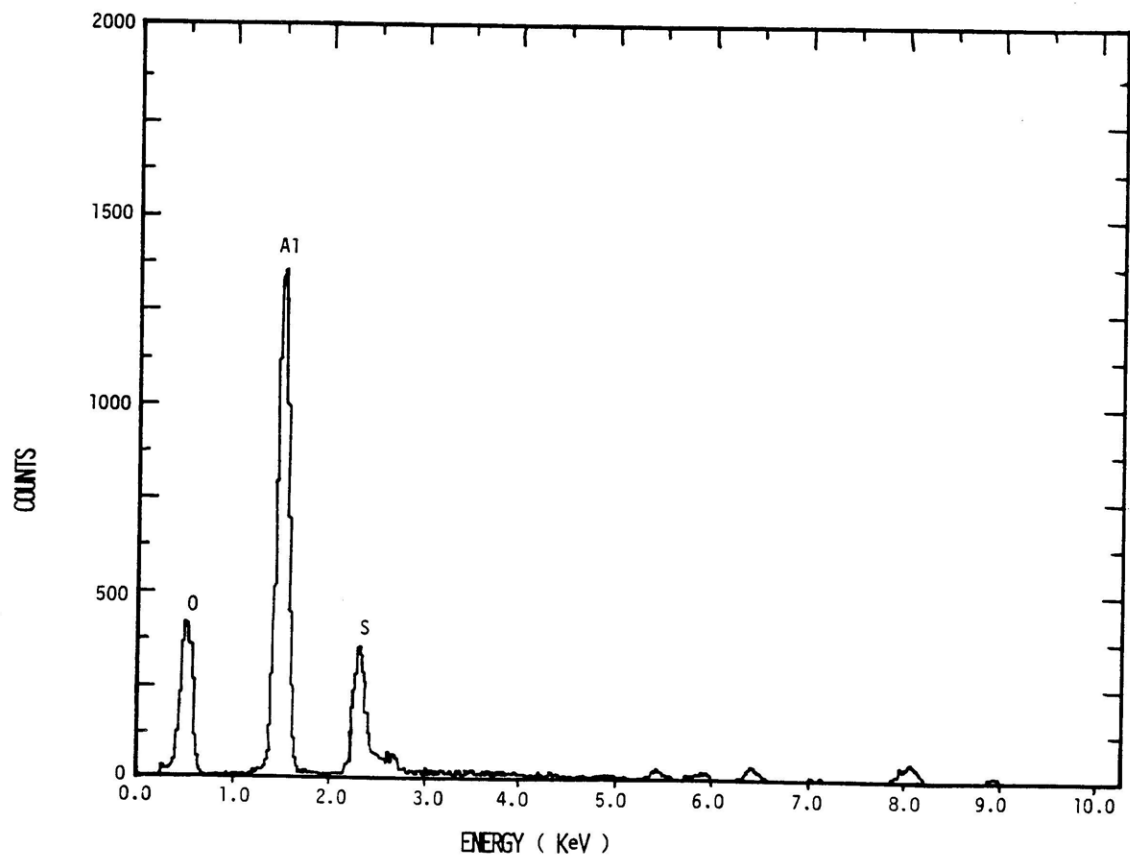


Figure 20(b). EDAX Spectrum of Aluminum Oxysulfide, $\text{Al}_2(\text{O,S})_3$.

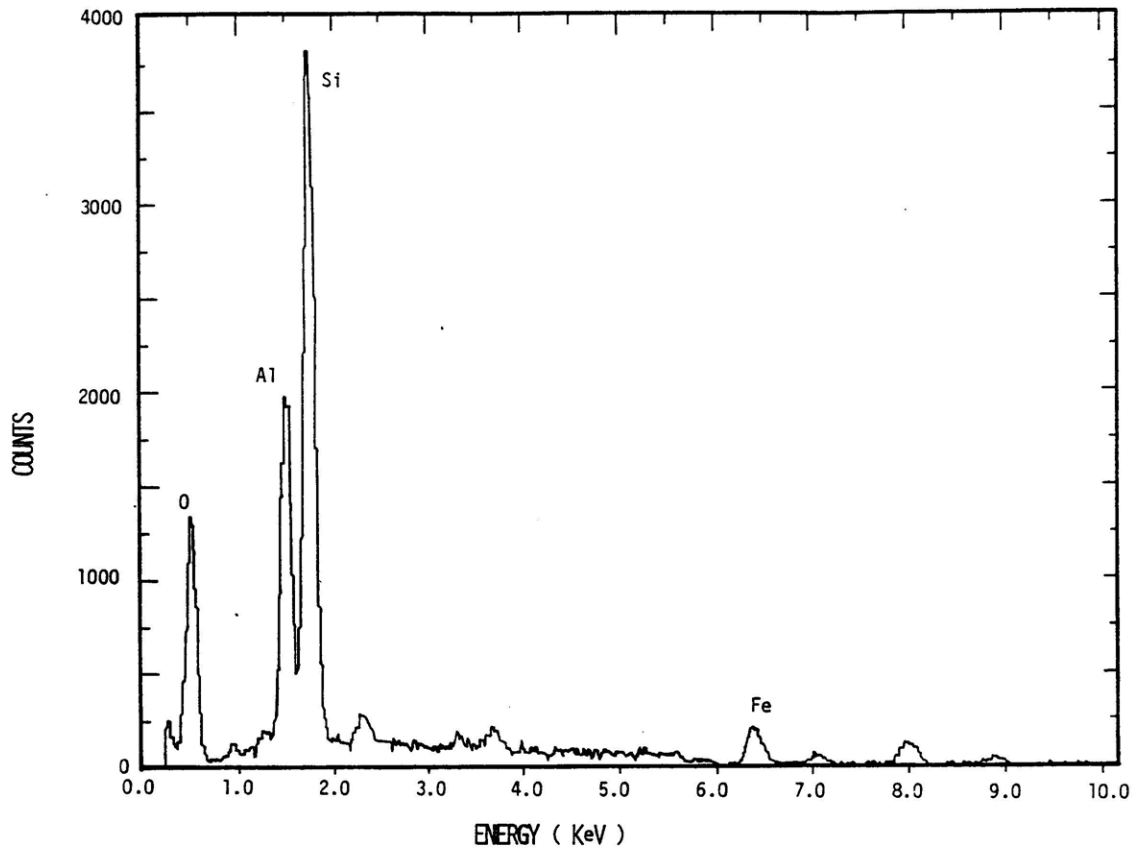


Figure 20(c). EDAX Spectrum of Aluminum Silicate($\text{Al}_2\text{O}_3 - \text{SiO}_2$).

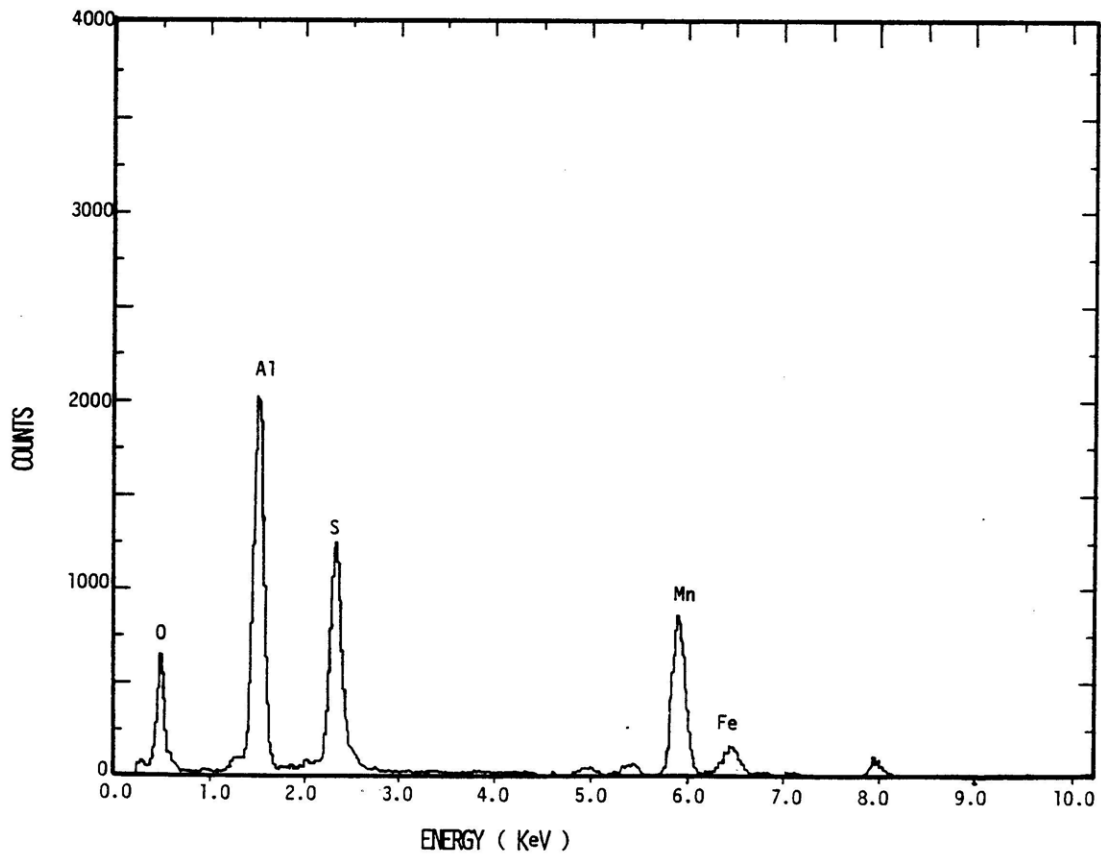


Figure 20(d). EDAX Spectrum of $\text{MnS} - \text{Al}_2\text{O}_3$.

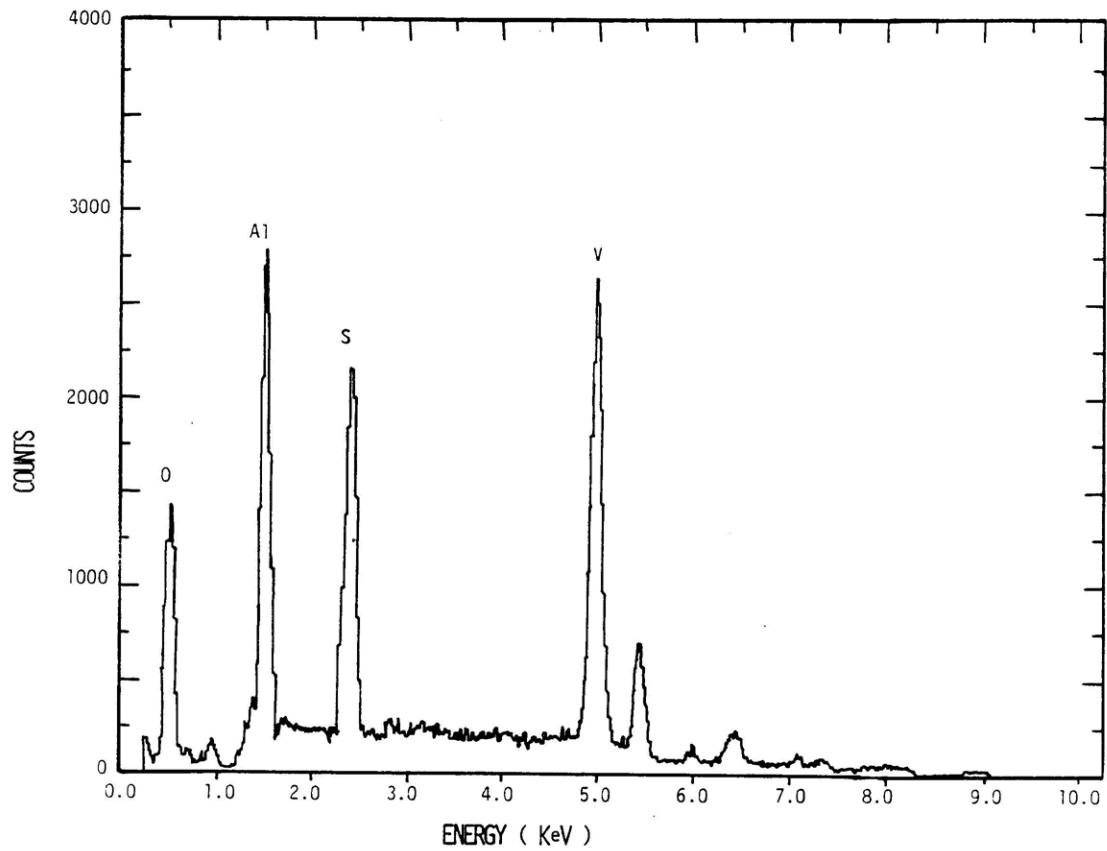


Figure 20(e). EDAX Spectrum of VS-Al₂O₃.

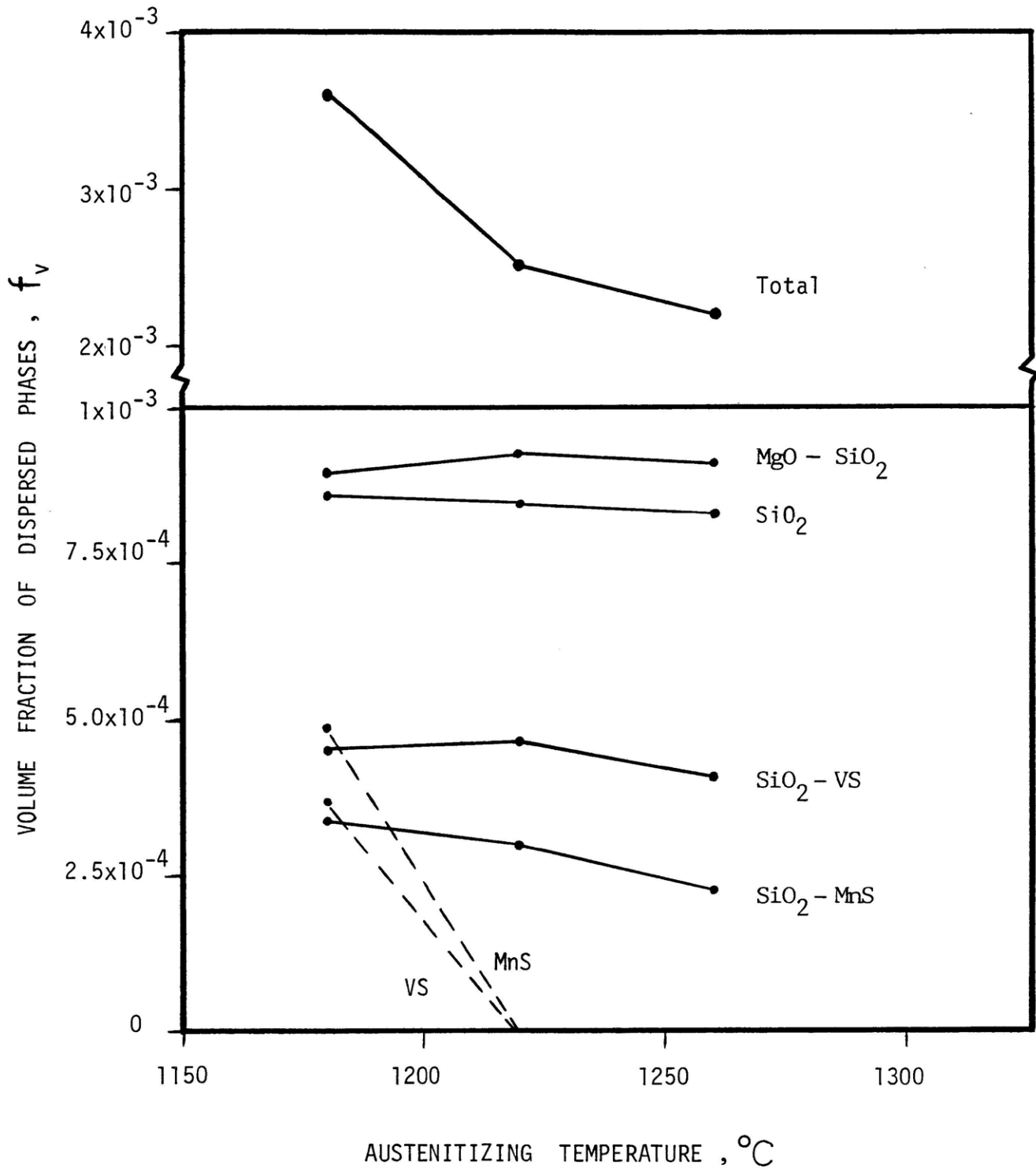


Figure 21: Volume Fraction of Dispersed Phases In RSP M-2 Matrix Steel as a Function of Austenitizing Temperature (1 hr. treatment).

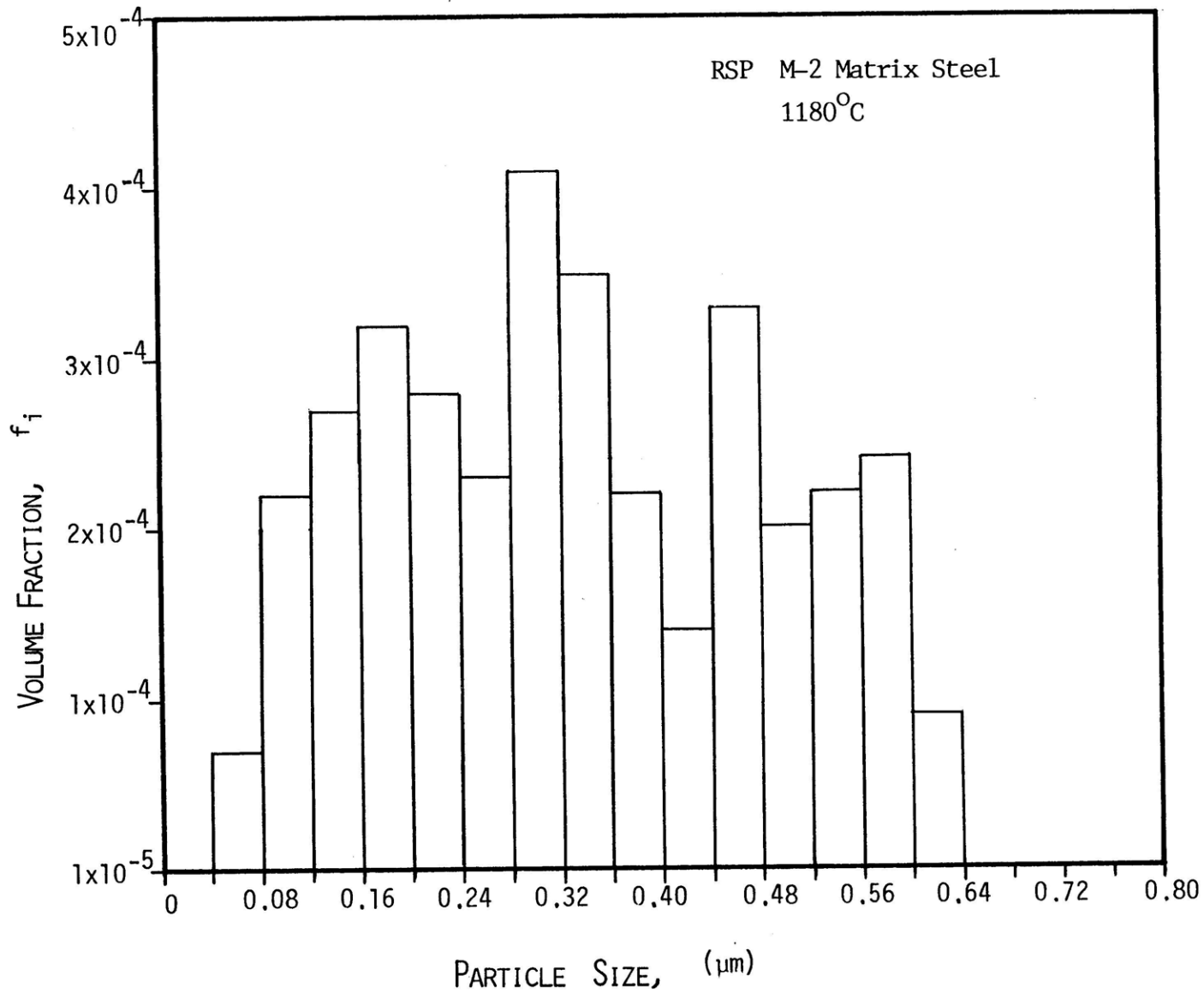


Figure 22A: Volume Fraction / Particle-Size Distribution In RSP M-2 Matrix Steel, Austenitized at 1180°C for One Hour.

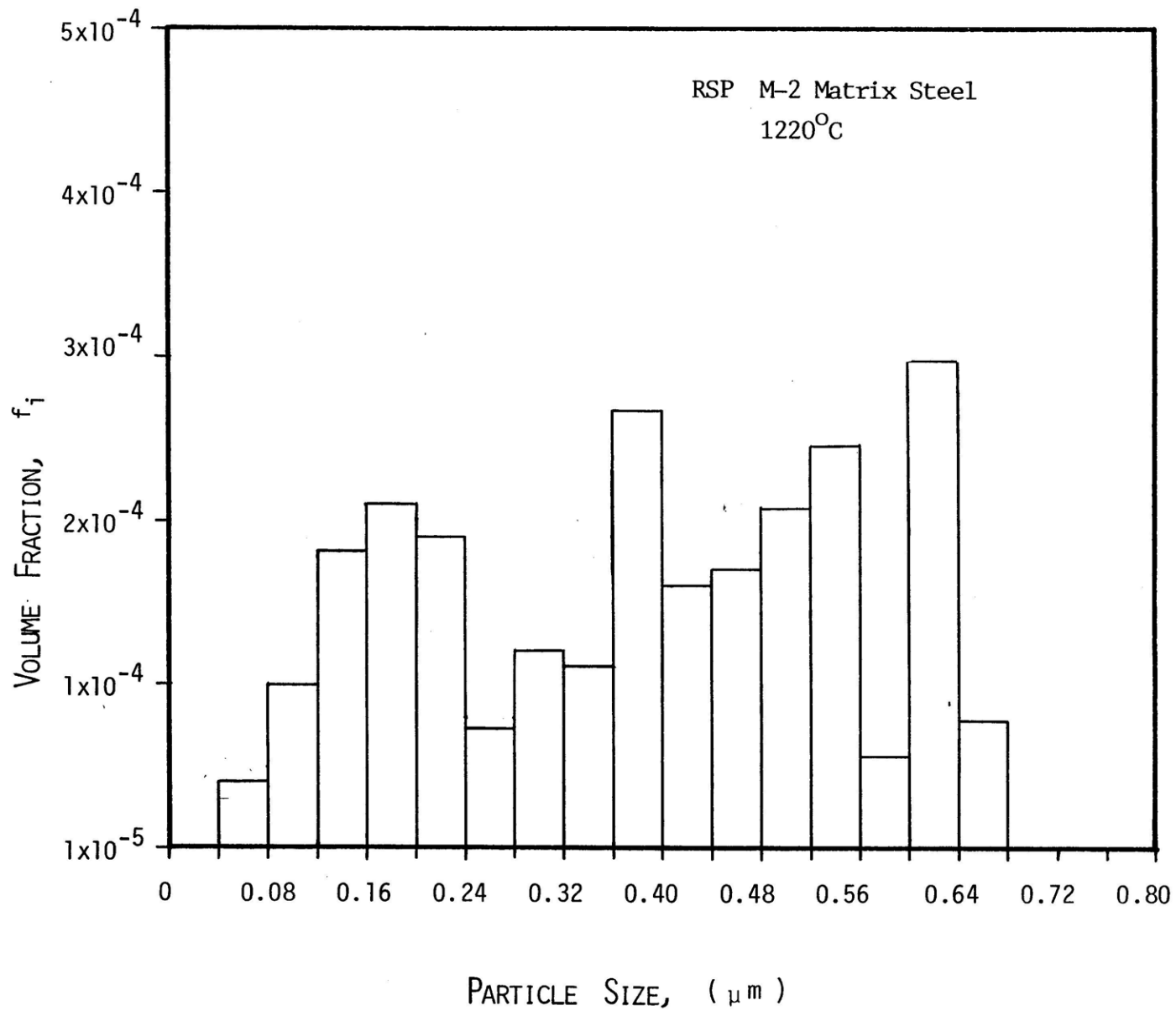


Figure 22B: Volume Fraction / Particle-Size Distribution In RSP M-2 Matrix Steel, Austenitized at 1220°C for One Hour.

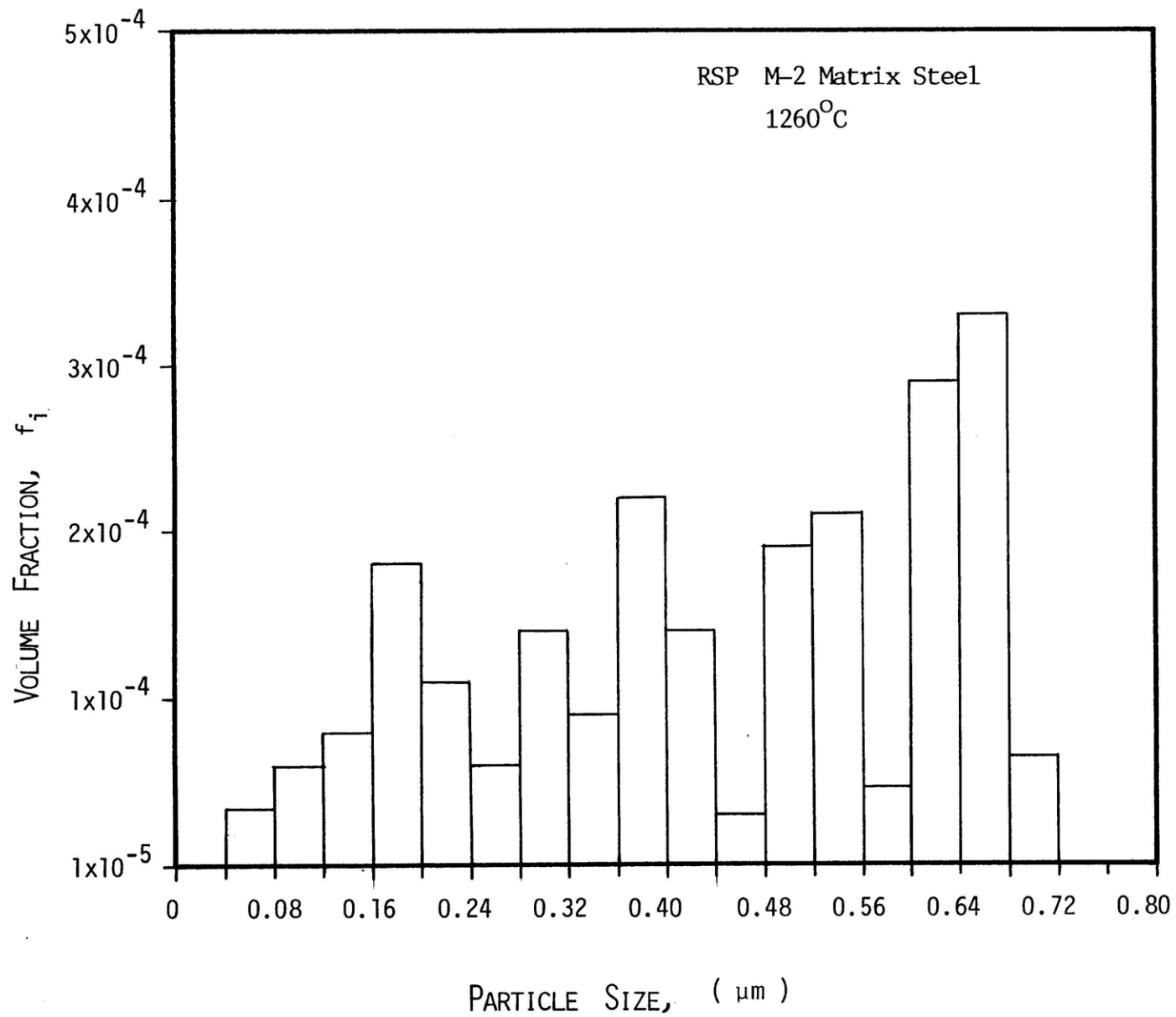


Figure 22C: Volume Fraction / Particle-Size Distribution In RSP M-2 Matrix Steel, Austenitized at 1260°C for One Hour.

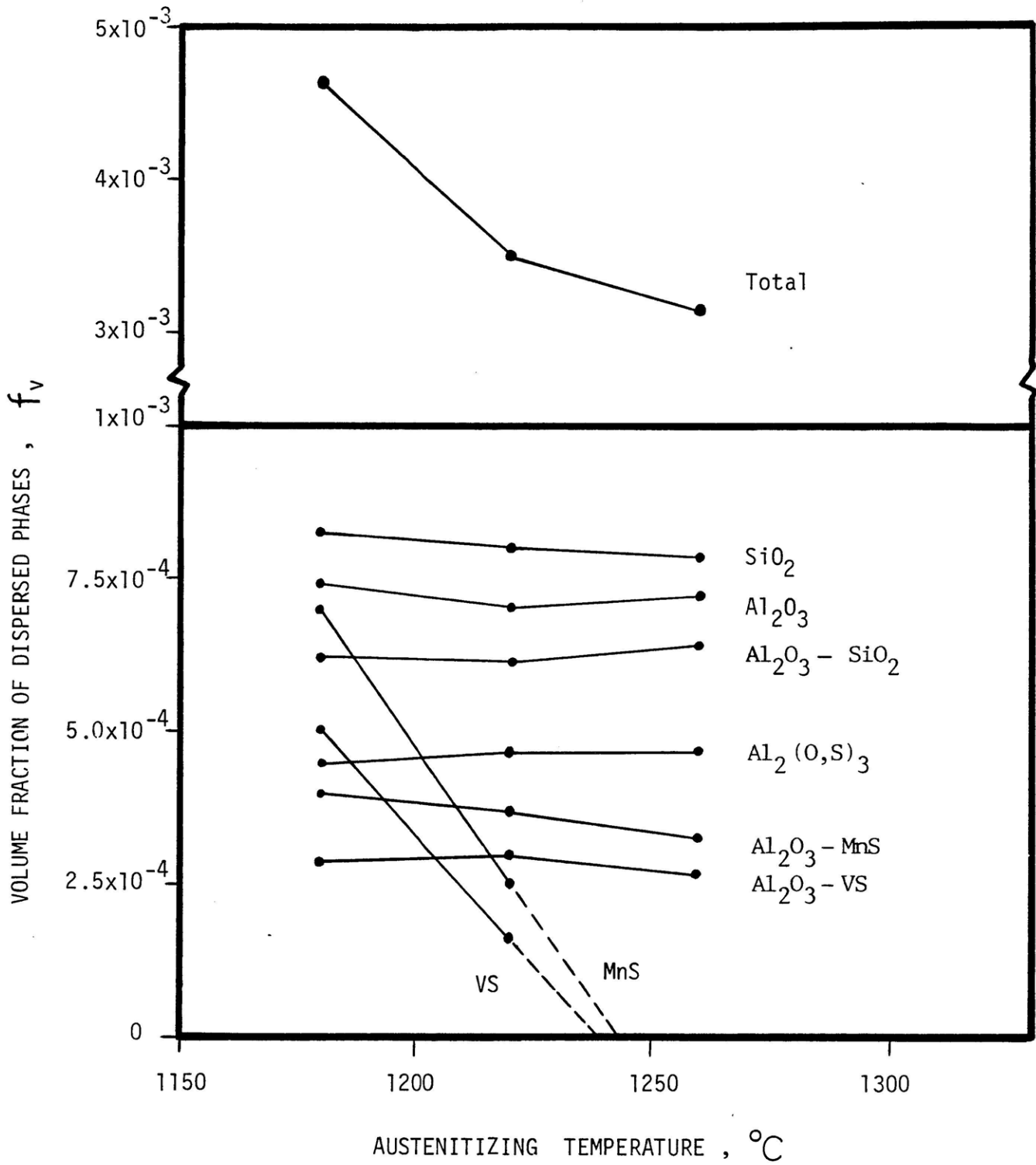


Figure 23: Volume Fraction of Dispersed Phases in RSP M-50 Matrix Steel as a Function of Austenitizing Temperature (1 hr. treatment)

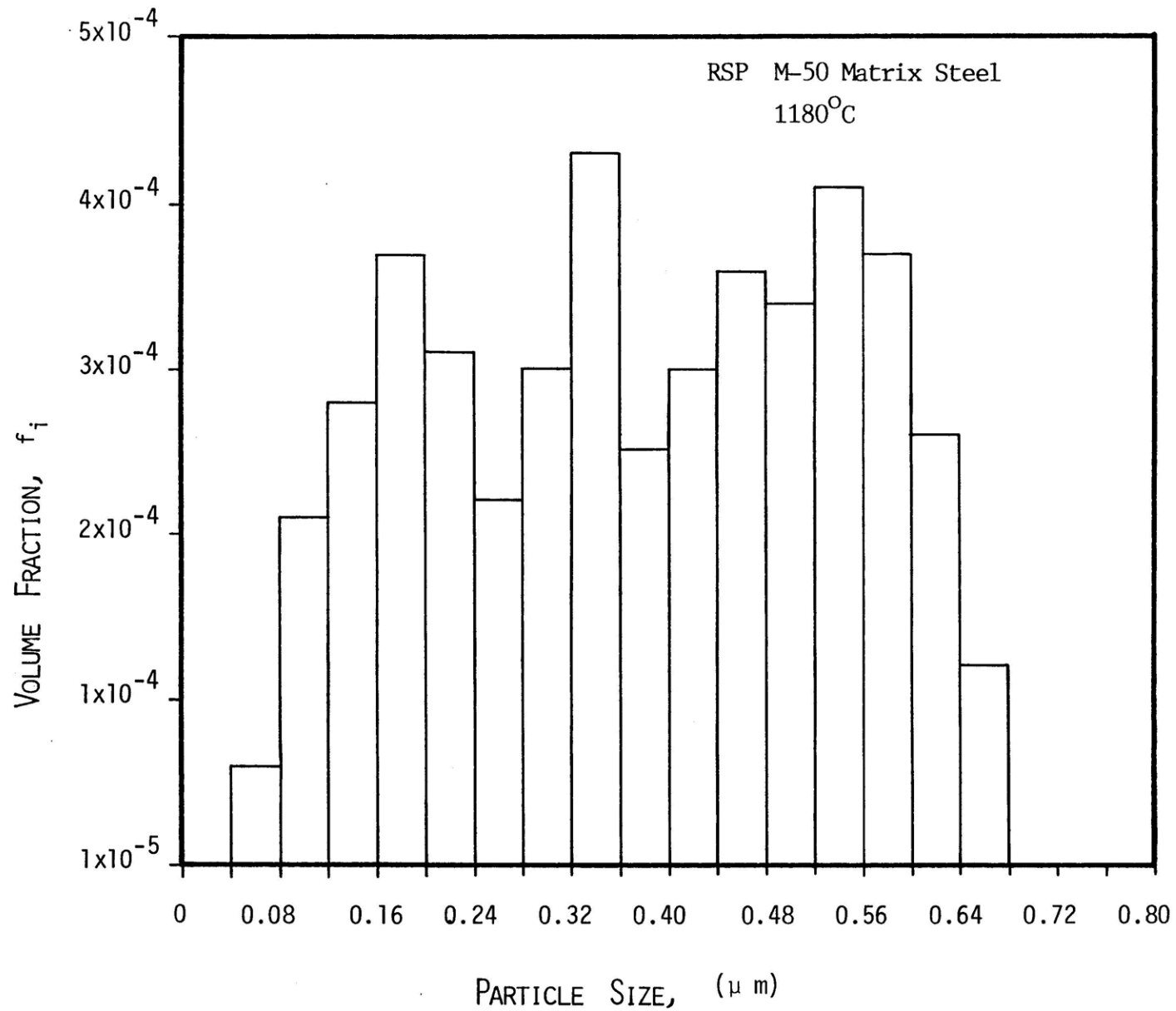


Figure 24A: Volume Fraction/ Particle Size Distribution In RSP M-50 Matrix Steel, Austenitized at 1180°C for One Hour.

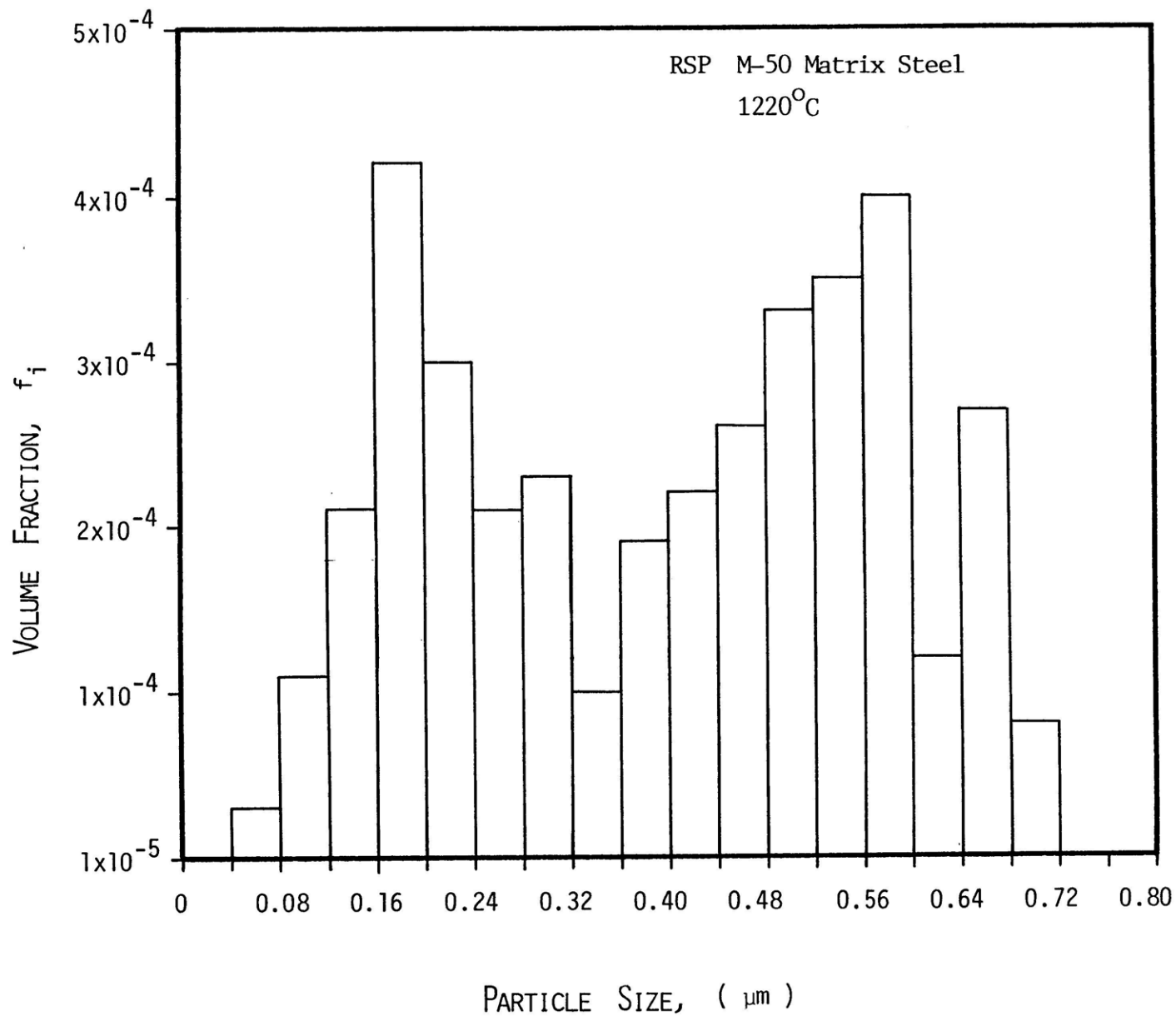


Figure 24B: Volume Fraction/ Particle-Size Distribution In RSP M-50 Matrix Steel, Austenitized at 1220°C for One Hour.

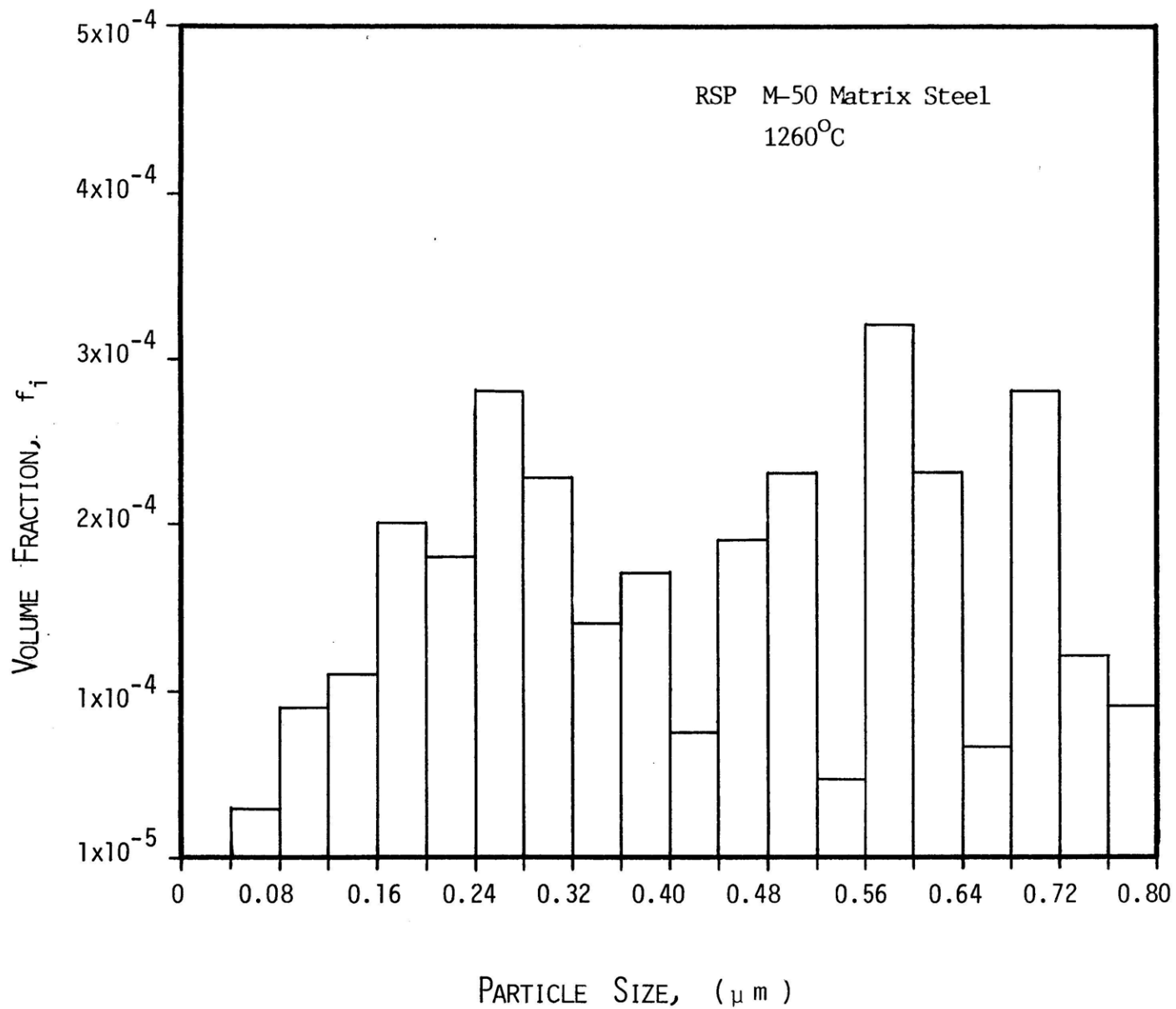
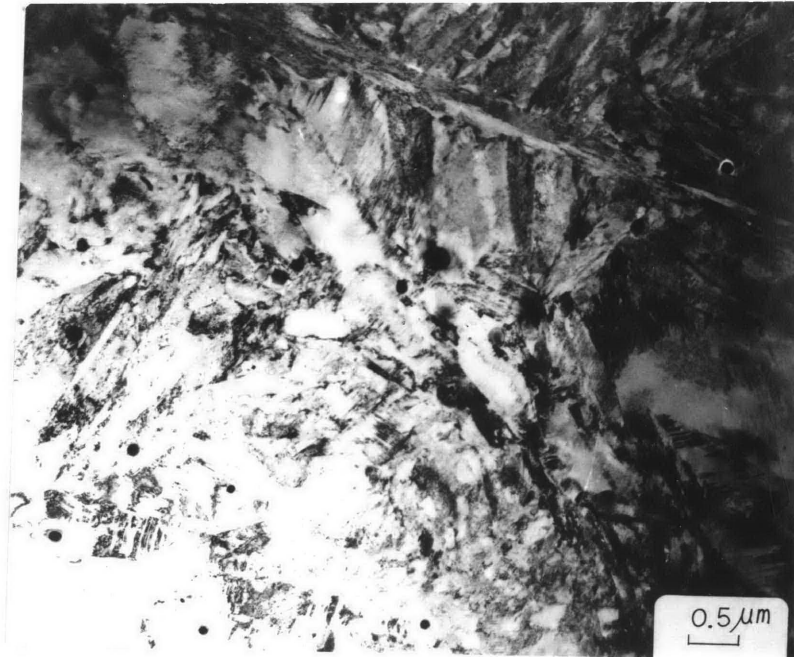
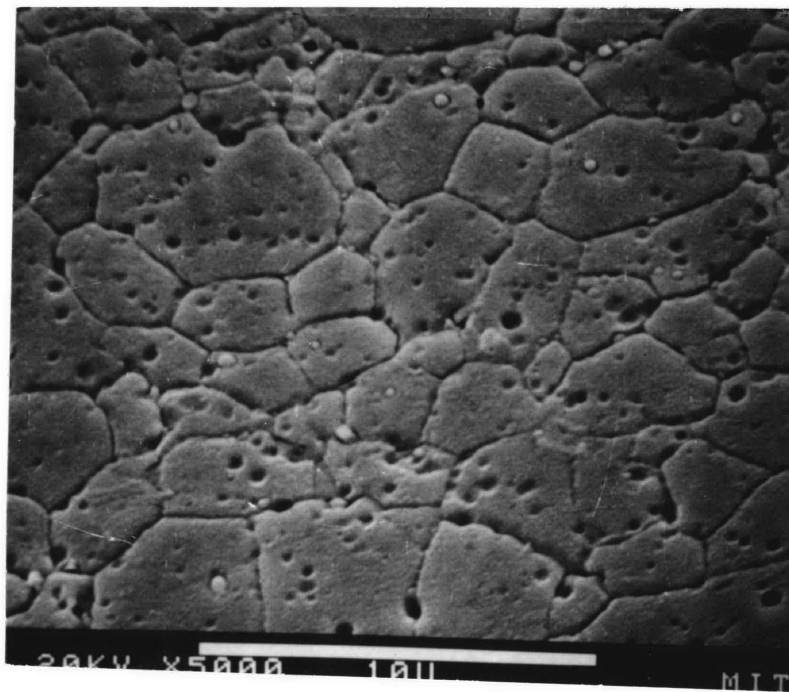


Figure 24C: Volume Fraction / Particle-Size Distribution In RSP M-50 Matrix Steel, Austenitized at 1260°C for One Hour.



(a)



(b)

Figure 25. Electron Micrograph of the RSP M-2 Matrix Steel, (a) TEM, 1220°C/1hr., (b) SEM, 1100°C/15min.



1.0 μm

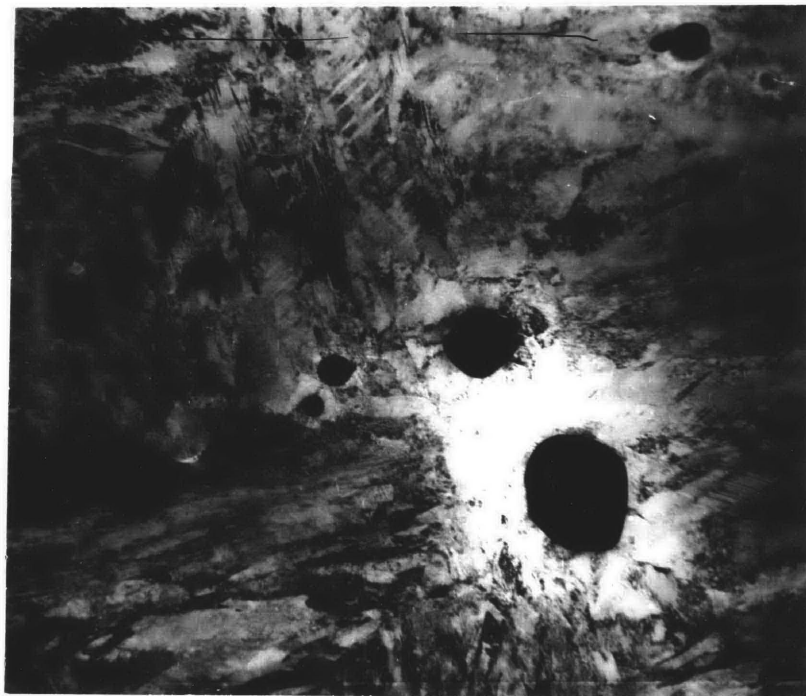


Figure 26. TEM Electron Micrograph of the RSP M-50 Matrix Steel, Austenitized at 1220°C for One Hour.

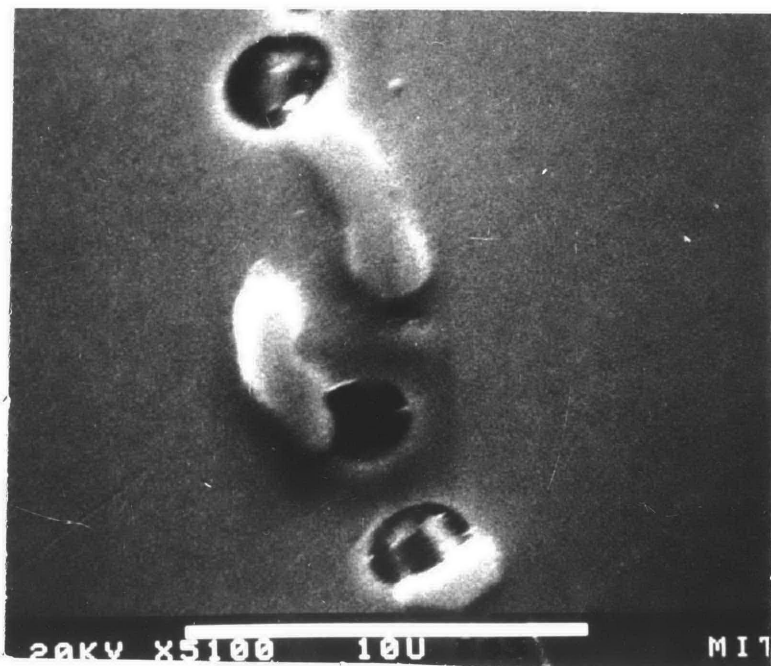
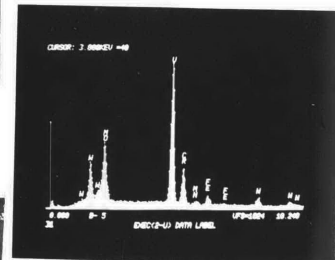


Figure 27. Scanning Electron Micrograph of the Morphology of Vanadium-rich Coarse Carbides, $(V,W,Mo,Cr)C$, in the Conventional (VAR) M-2 Matrix Steel, Austenitized at $1220^{\circ}C$ for One Hour.

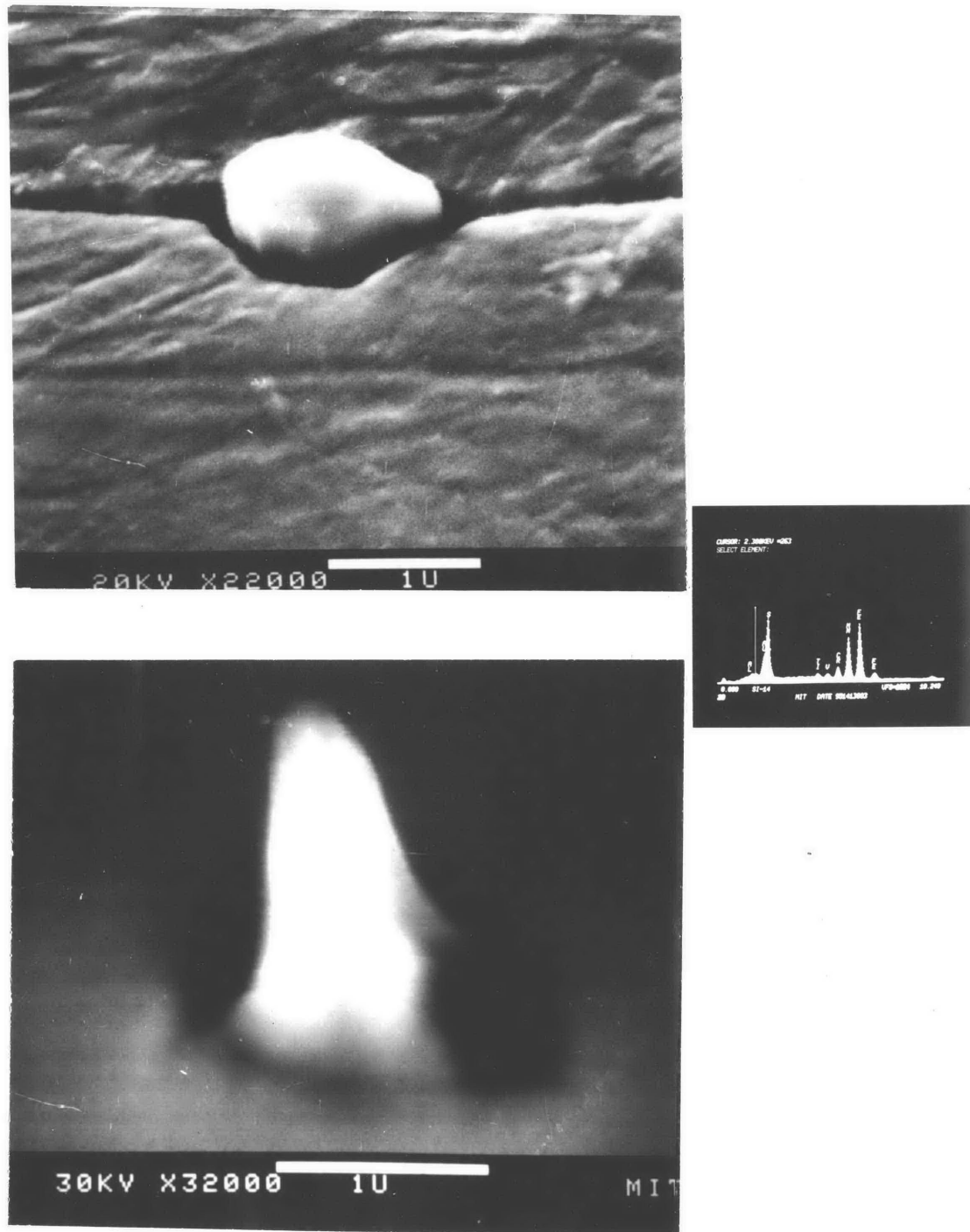


Figure 28. Scanning Electron Micrograph of the MnS Morphology in the Conventional (VAR) Matrix Steels, Austenitized at 1180°C for One Hour.

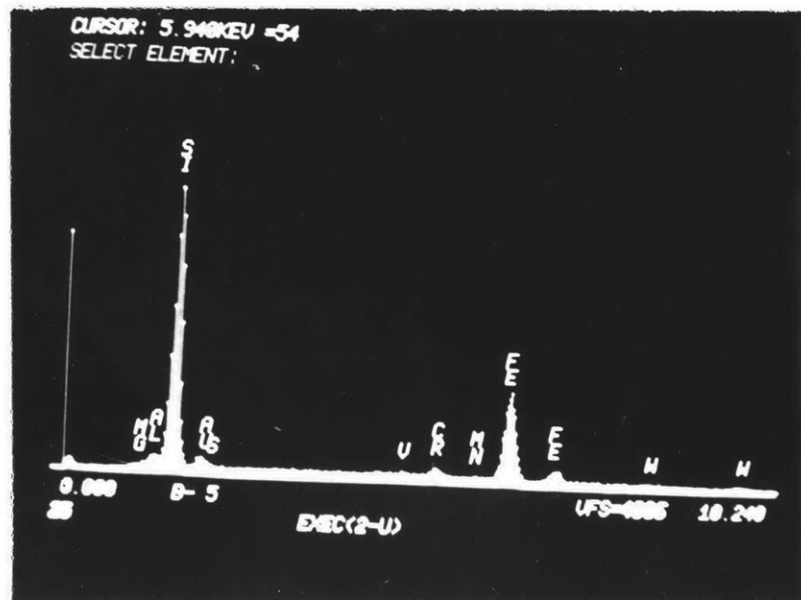
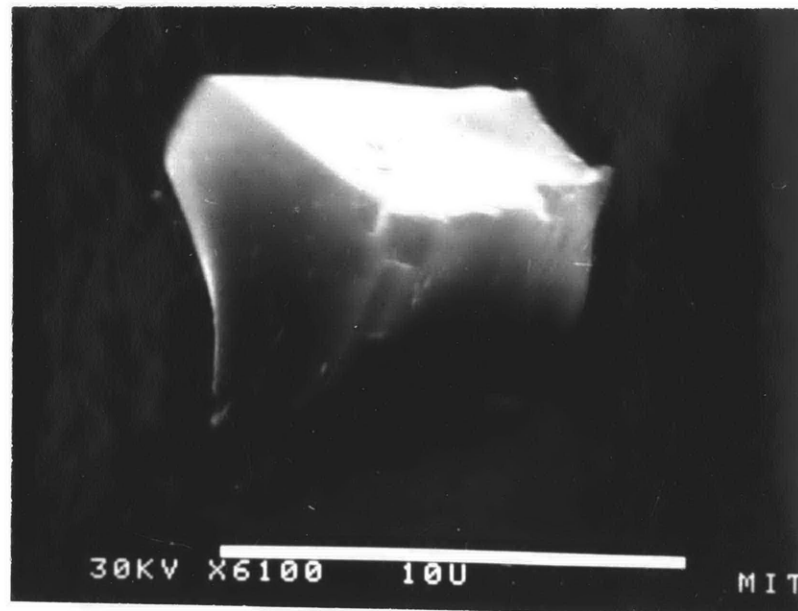


Figure 29. Scanning Electron Micrograph of the SiO_2 Morphology in the Conventional (VAR) Matrix Steels, Austenitized at 1260°C for One Hour.

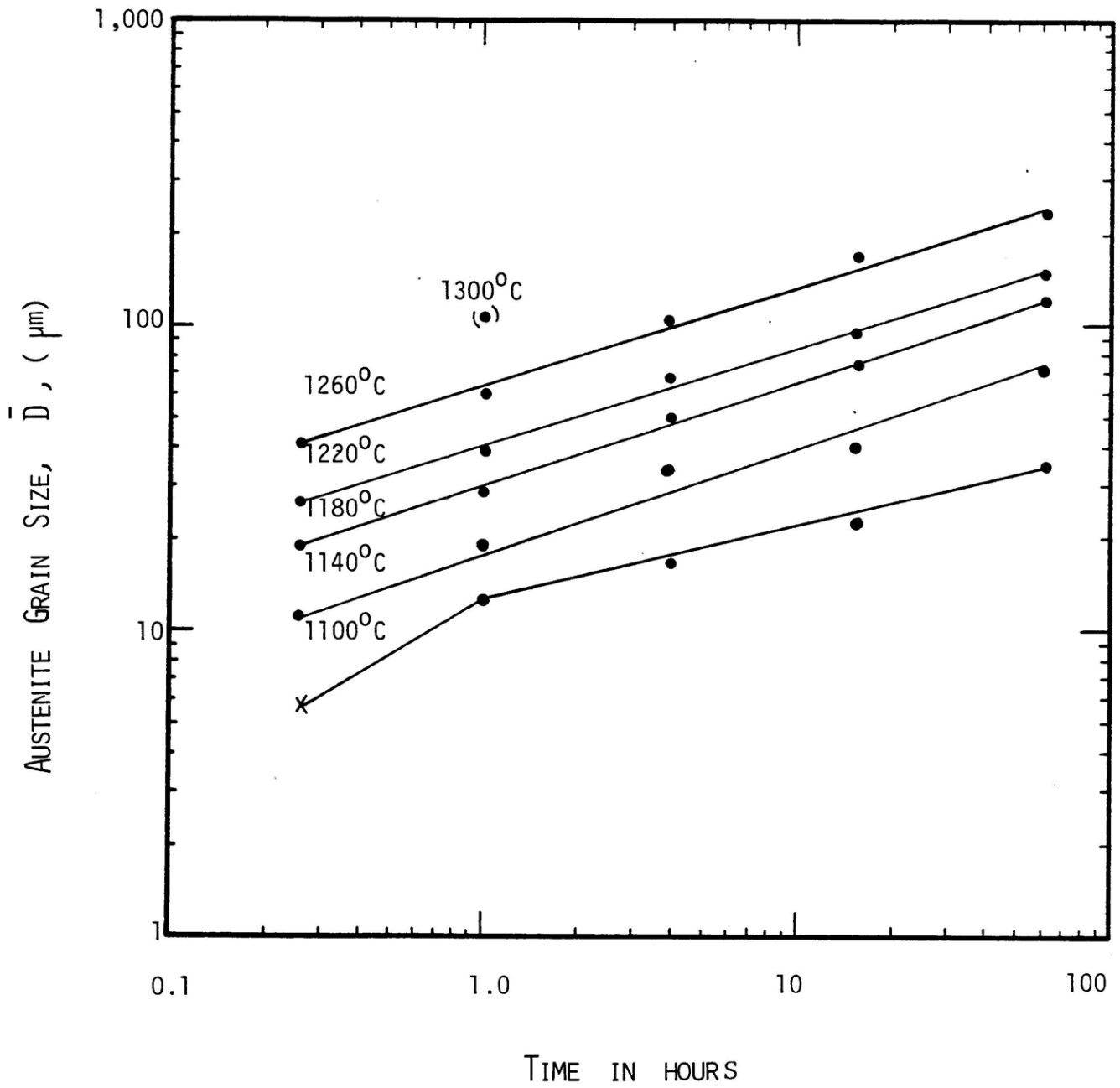


Figure 30: Isothermal Grain Growth Behavior of RSP M-2 Matrix Steel.

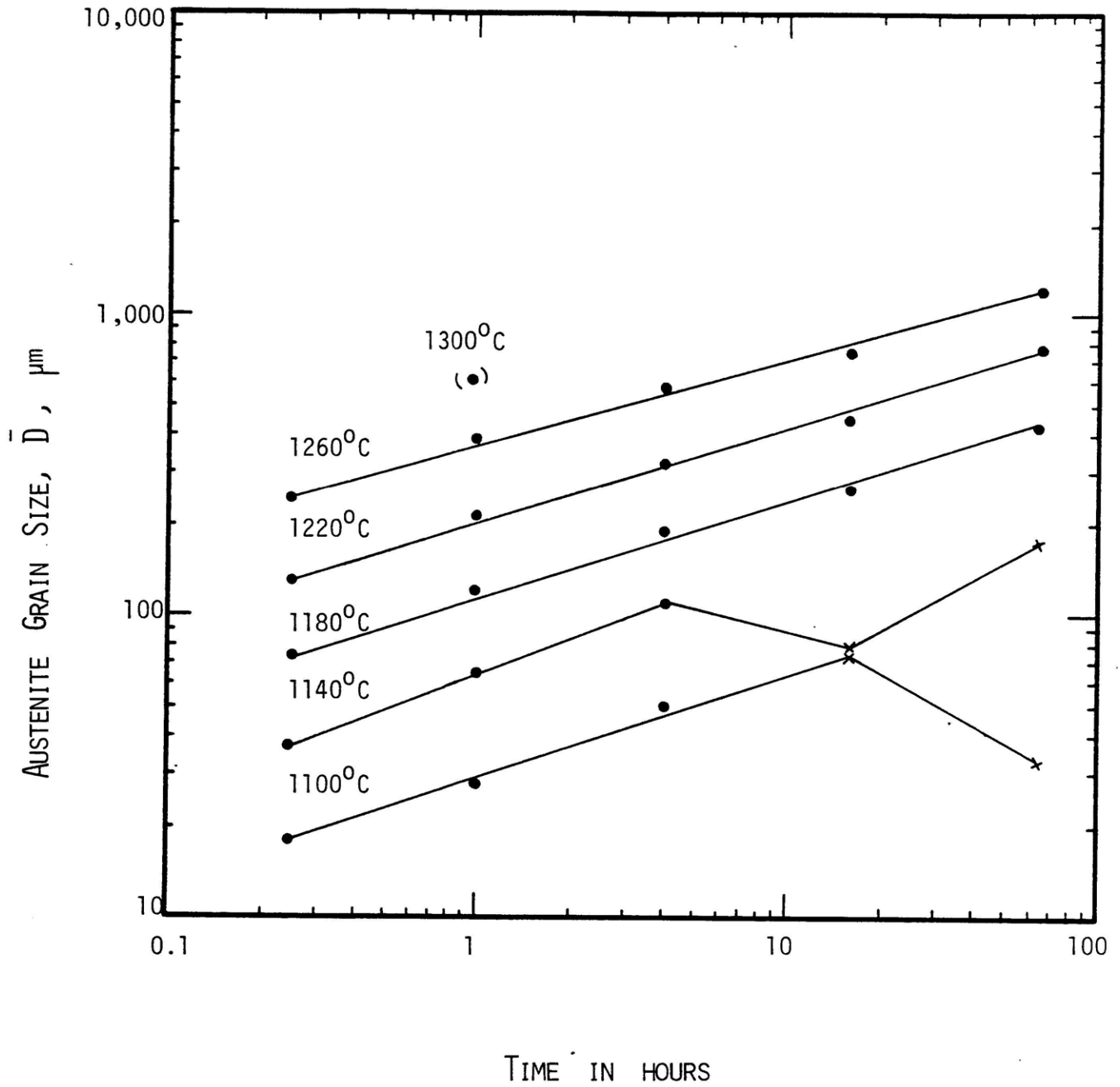


Figure 31. Isothermal Grain-Growth Behavior of VAR M-2 Matrix Steel.

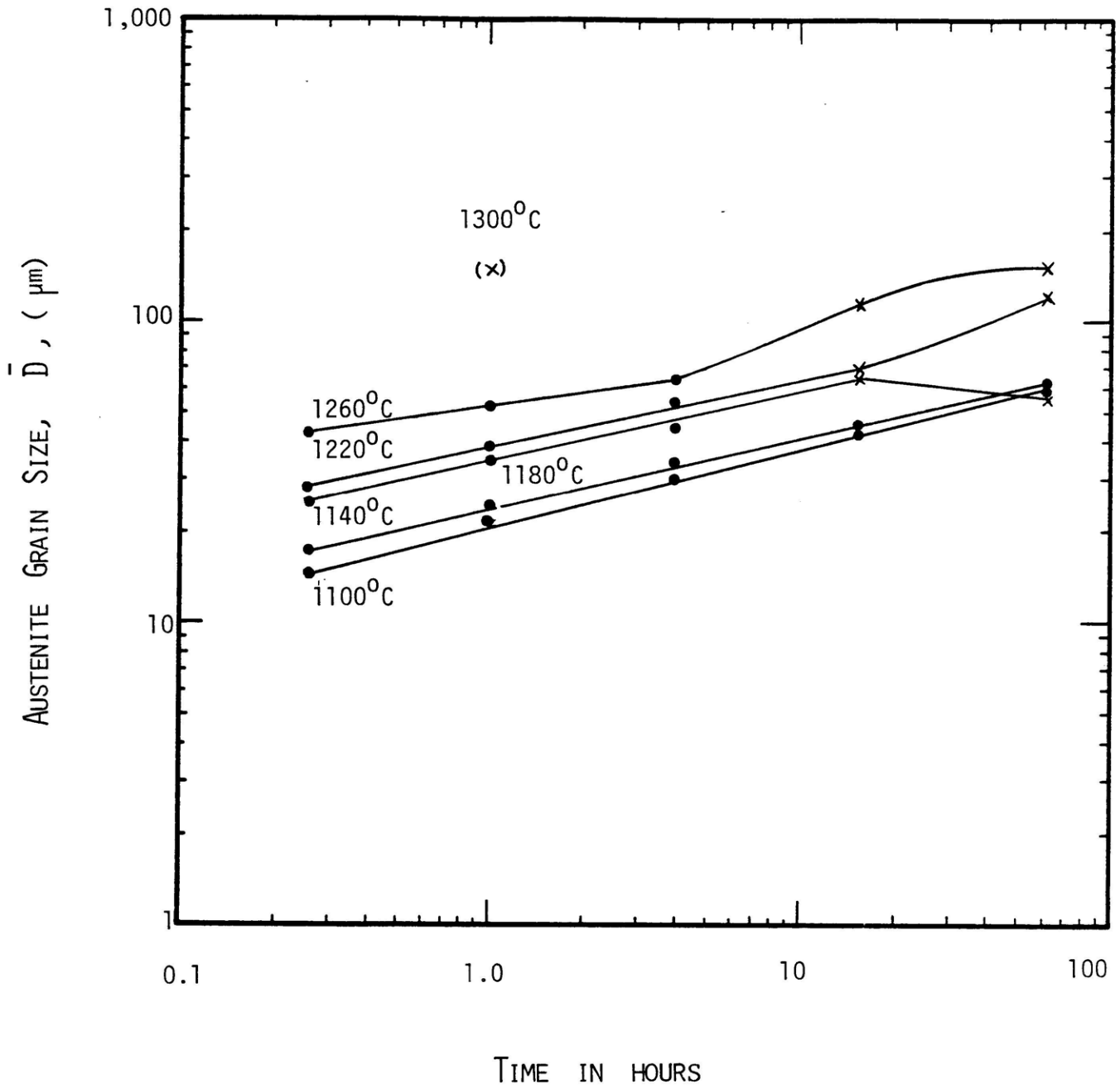


Figure 32 : Isothermal Grain-Growth Behavior of RSP M-50 Matrix Steel.

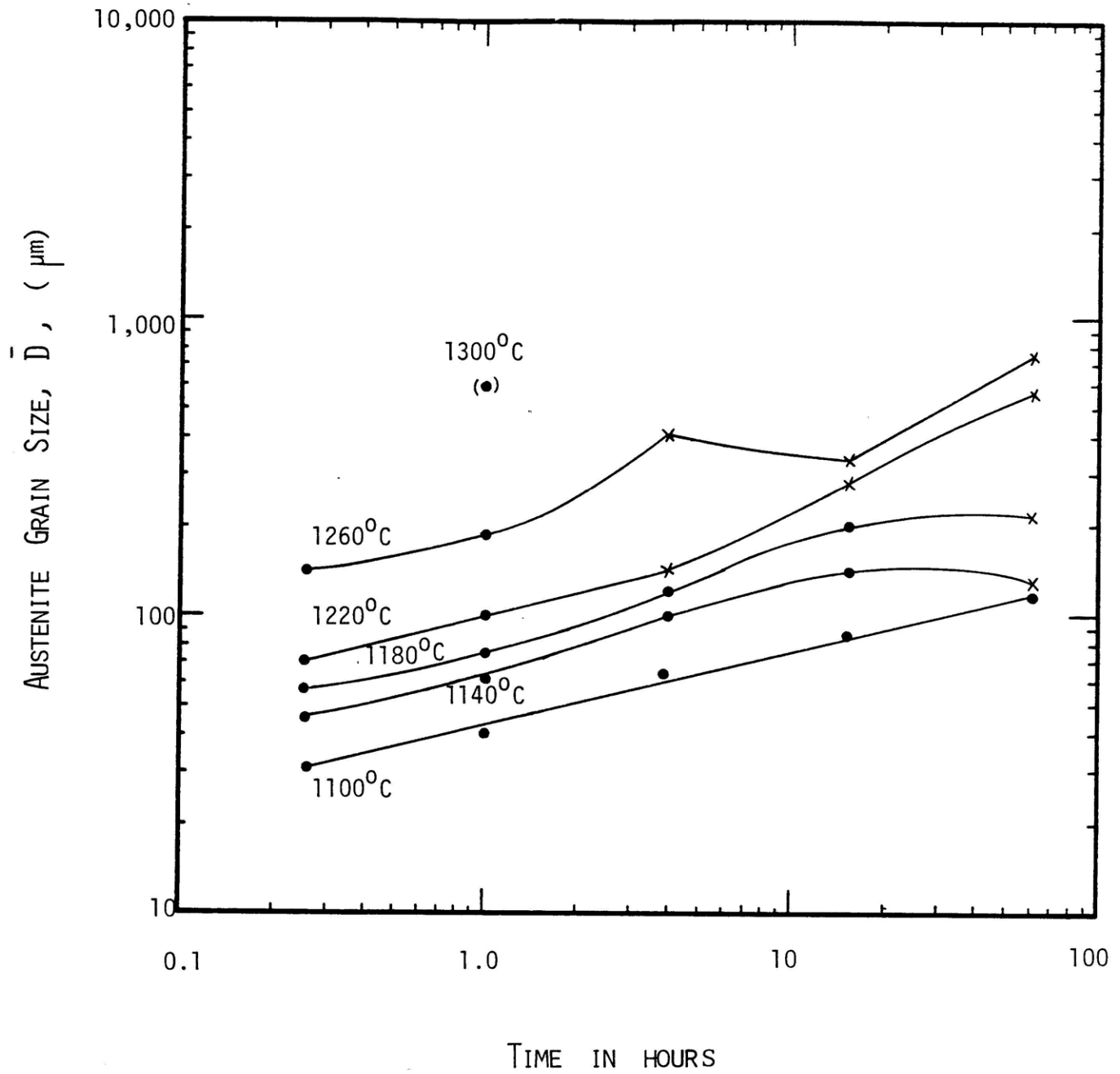
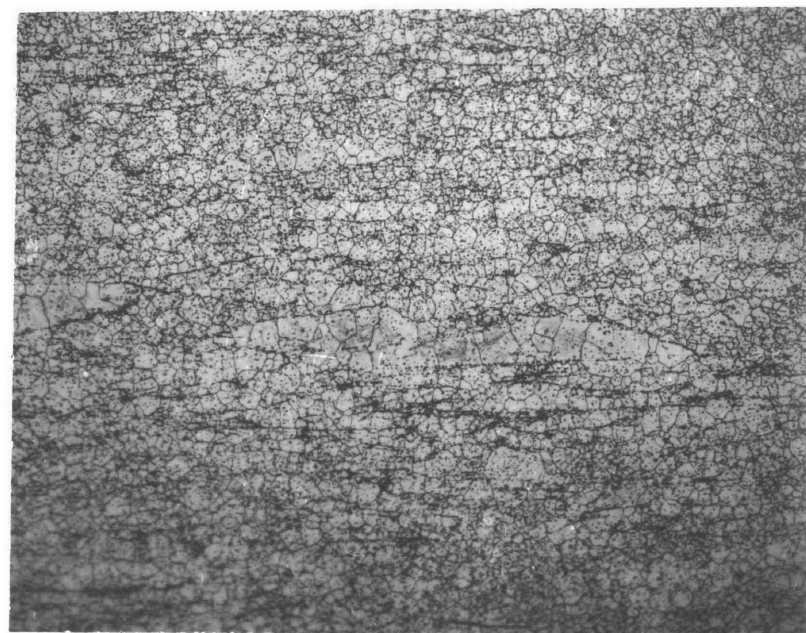
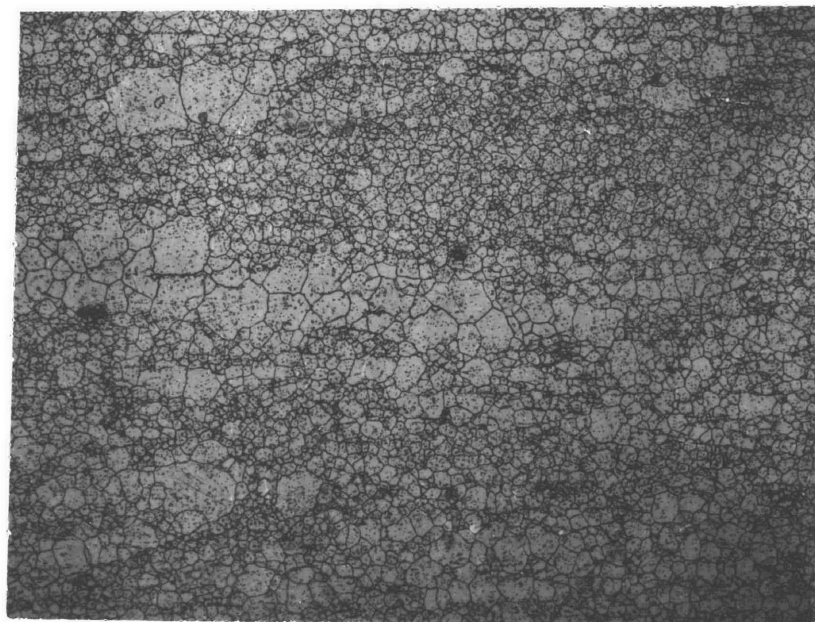


Figure 33. Isothermal Grain-Growth Behavior of VAR M-50 Matrix Steel.



20 μm



20 μm

Figure 34. Optical Micrograph of the Prior Powder-Particle Boundaries in the RSP M-2 Matrix Steel, Austenitized at 1100°C for 15 Minutes.

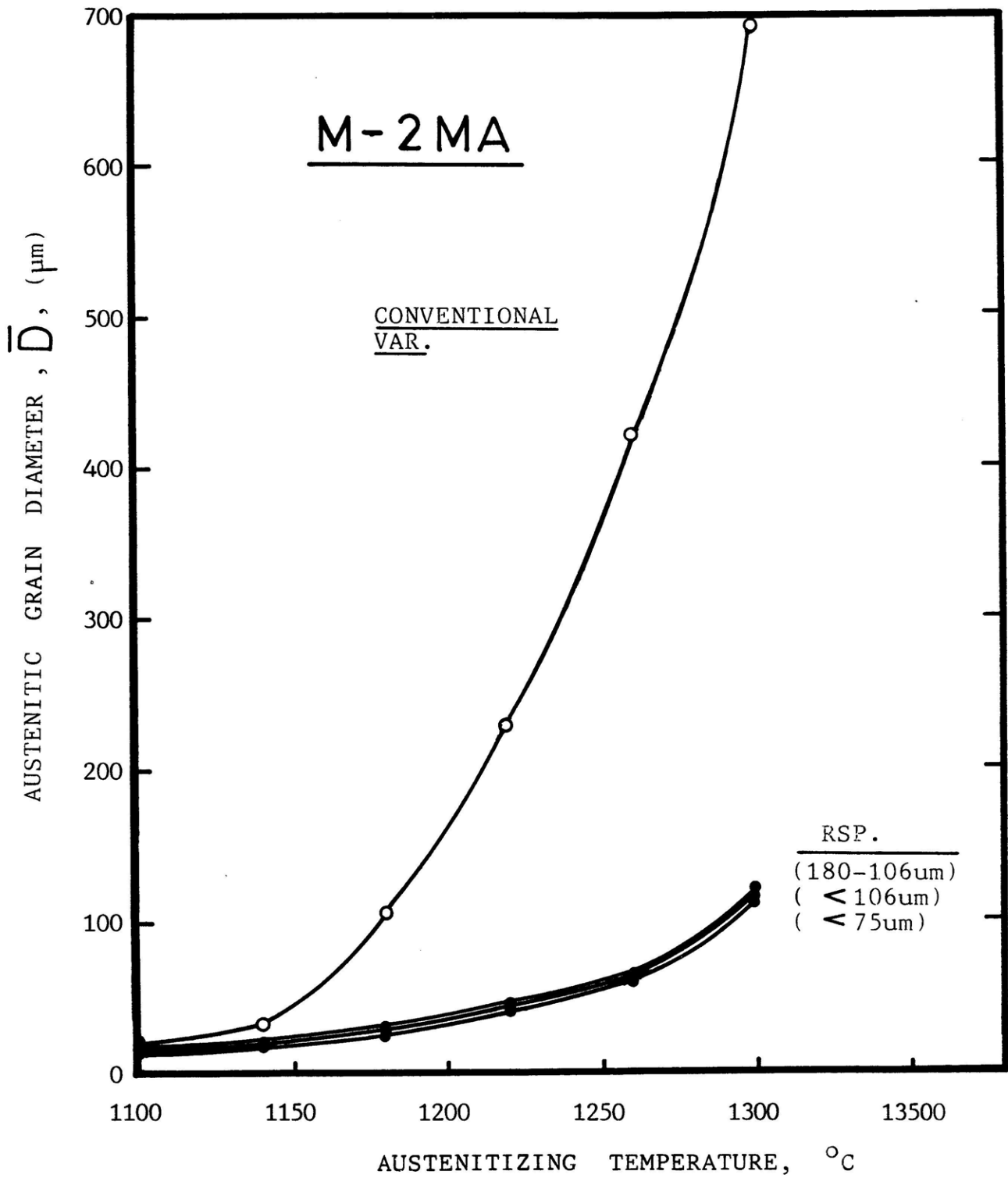


Figure 35 . Austenitic Grain Growth of Conventional(VAR) and RSP M-2 Matrix Steels, Austenitized at Various Temperatures for One Hour.

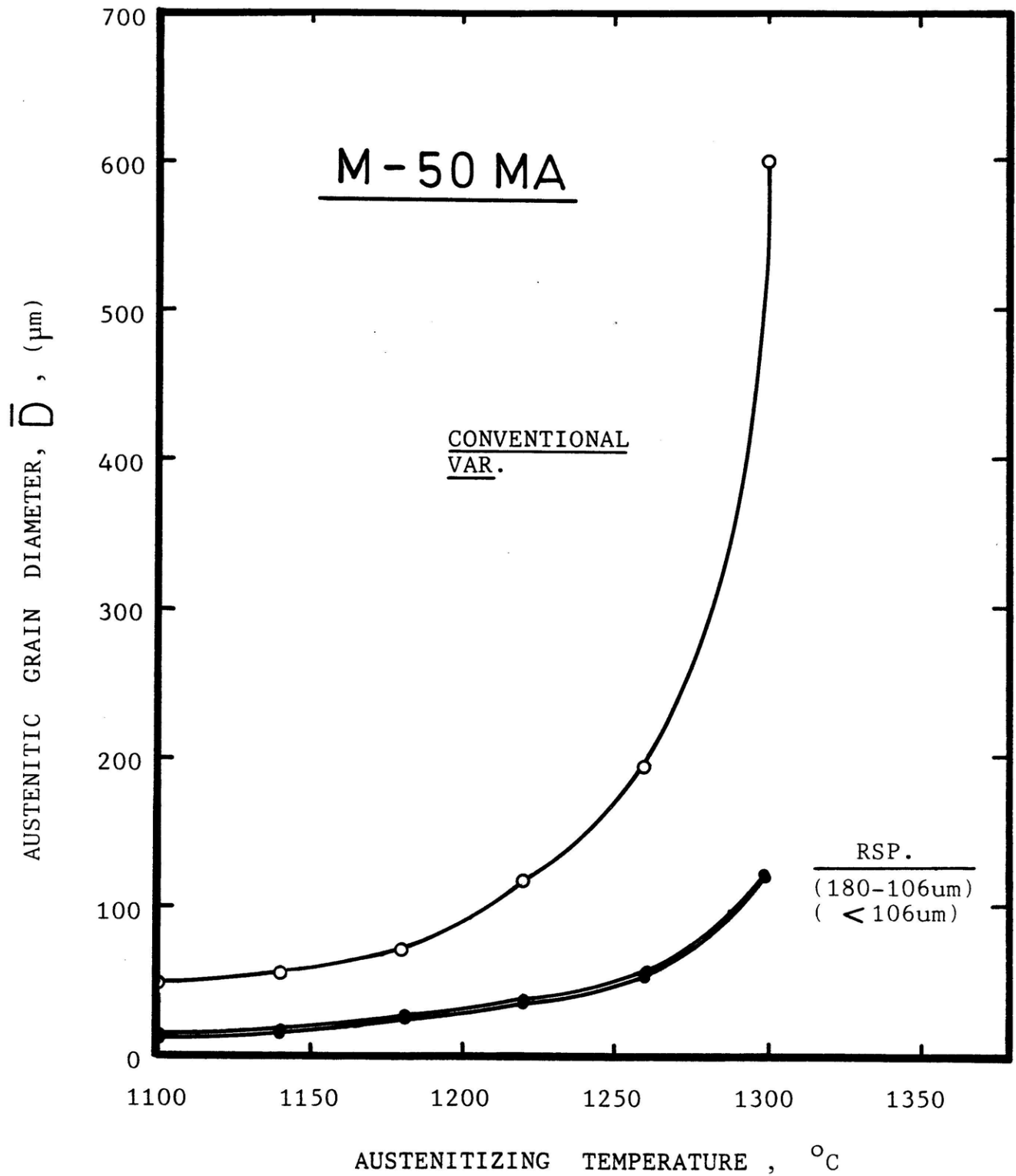


Figure 36. Austenitic Grain Growth of the Conventional(VAR) and RSP M-50 Matrix Steels, Austenitized at Various Temperatures for One Hour.

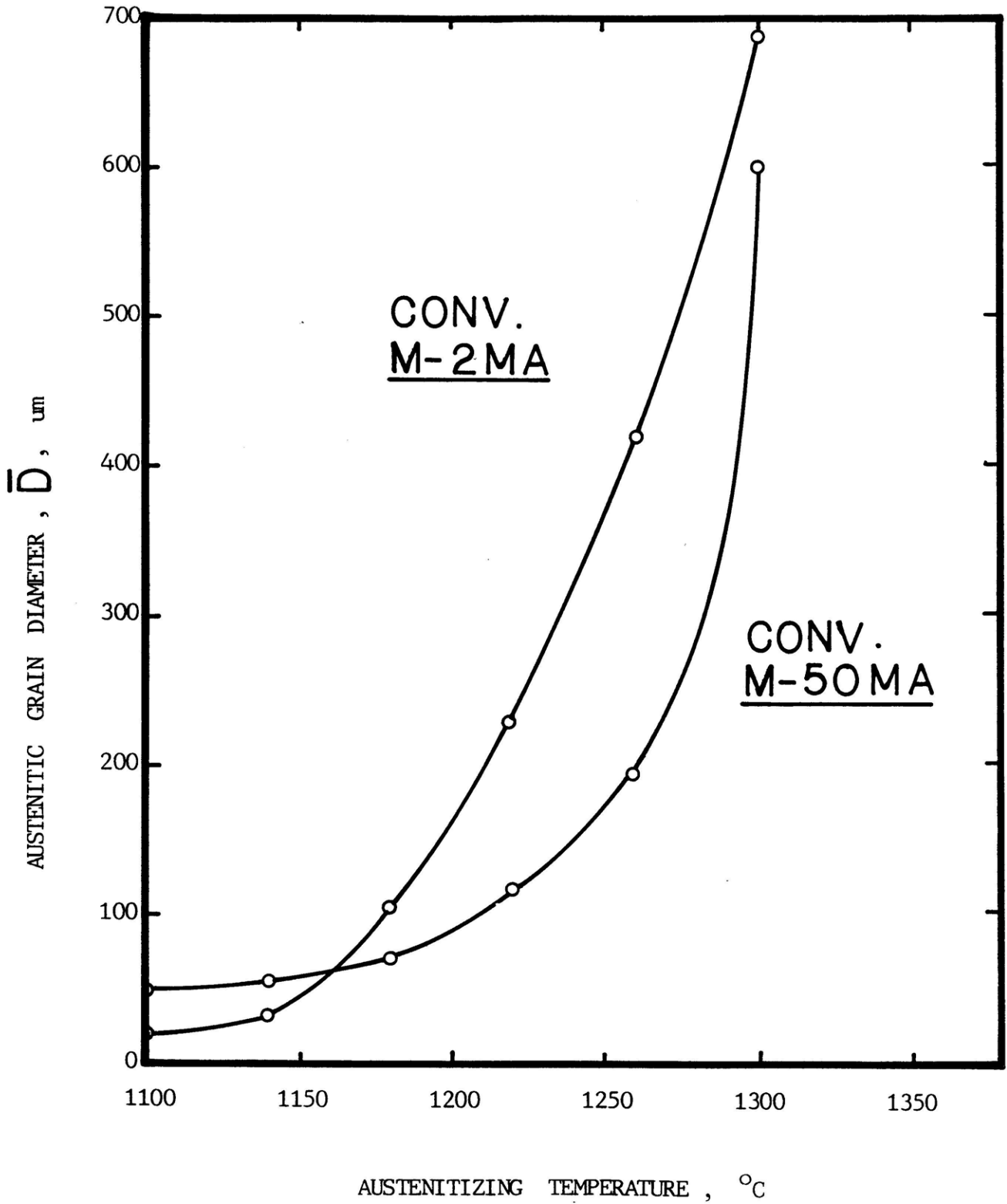


Figure 37. Comparison of Grain-Growth Behavior Between the Conventional M-2 and M-50 Matrix Steels at Various Austenitizing Temperatures for One Hour.

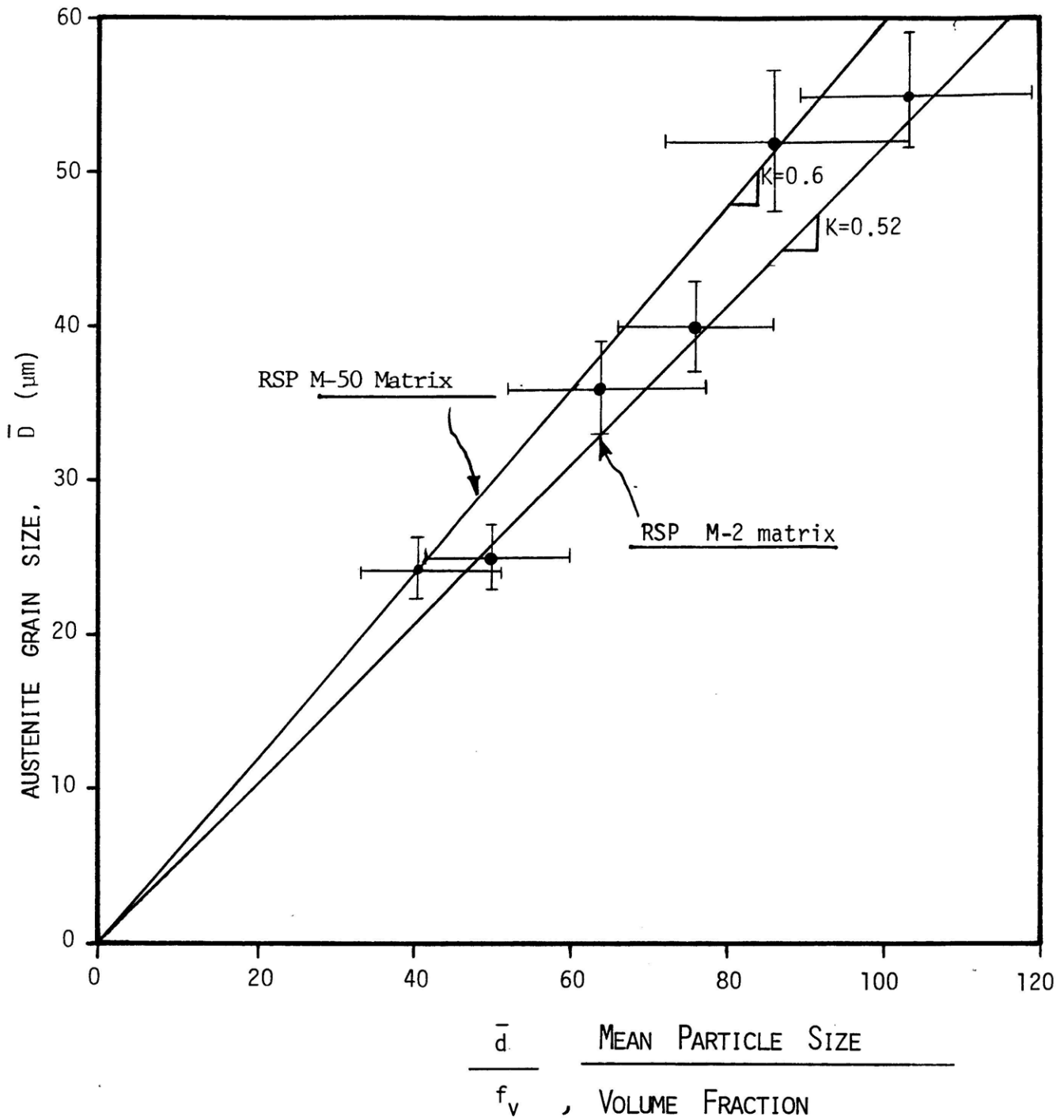


Figure 38: Linear Relationship Between \bar{D} And $\frac{\bar{d}}{f_v}$ In The RSP M-2 Matrix And M-50 Matrix Steels, Austenitized at 1180°C , 1220°C , and 1260°C For One Hour.

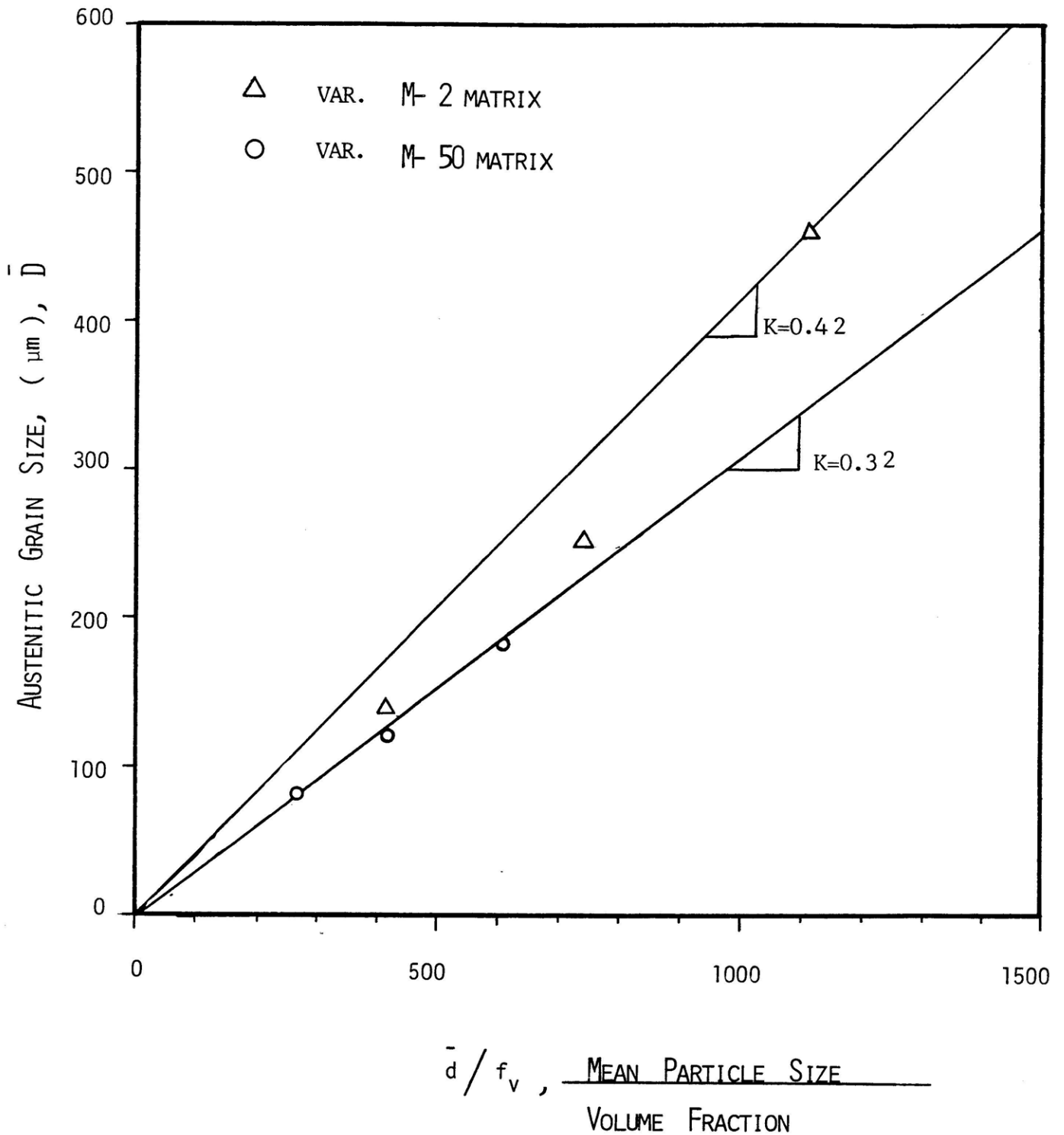


Figure 39: Relationship Between \bar{D} and \bar{d} / f_v in the VAR M-2 and M-50 Matrix Steels, Austenitized at 1180°C, 1220°C, and 1260°C for One Hour.

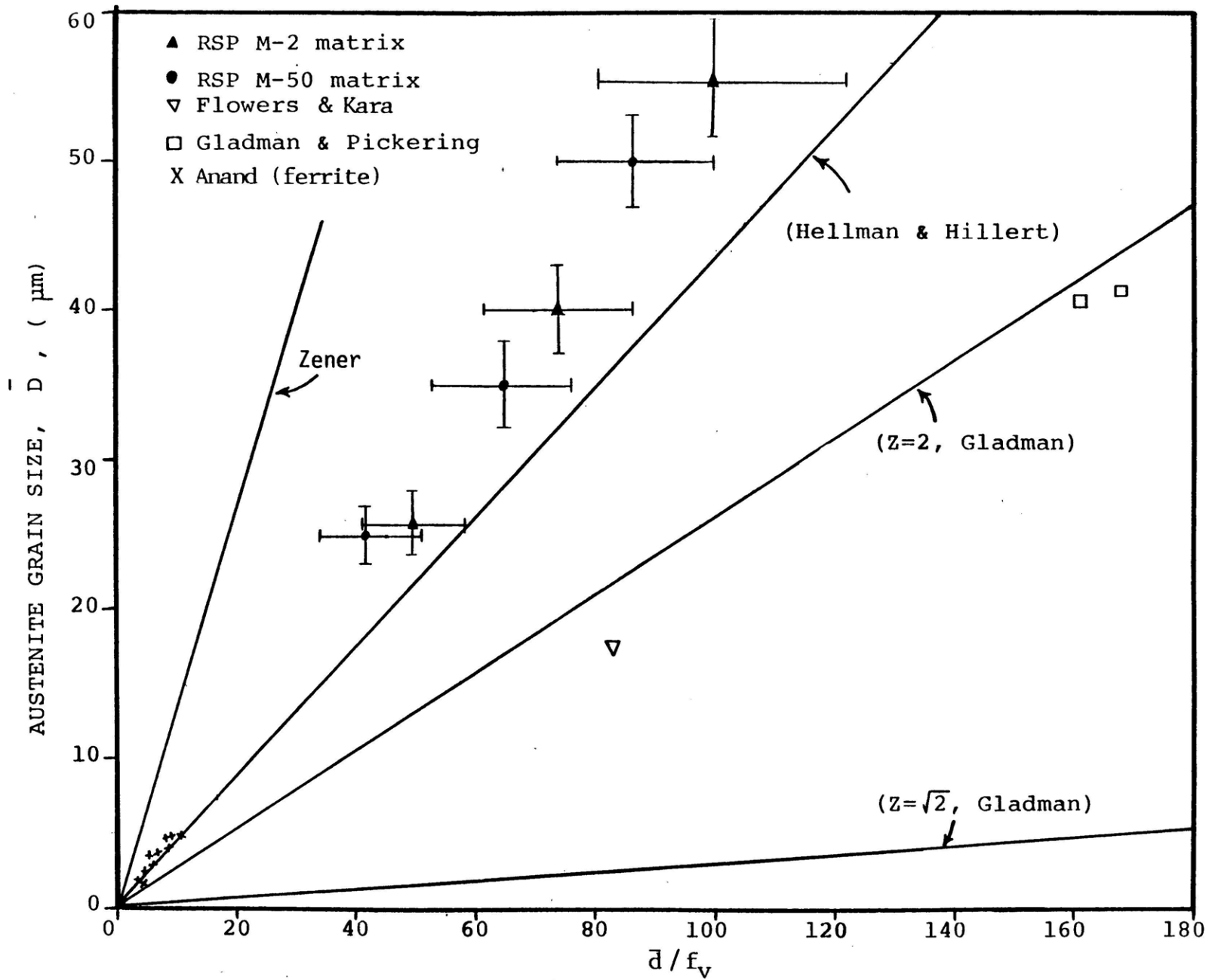


Figure 40. The Discrepancy Between the Current Grain-Boundary Pinning Models and Experimental Results.

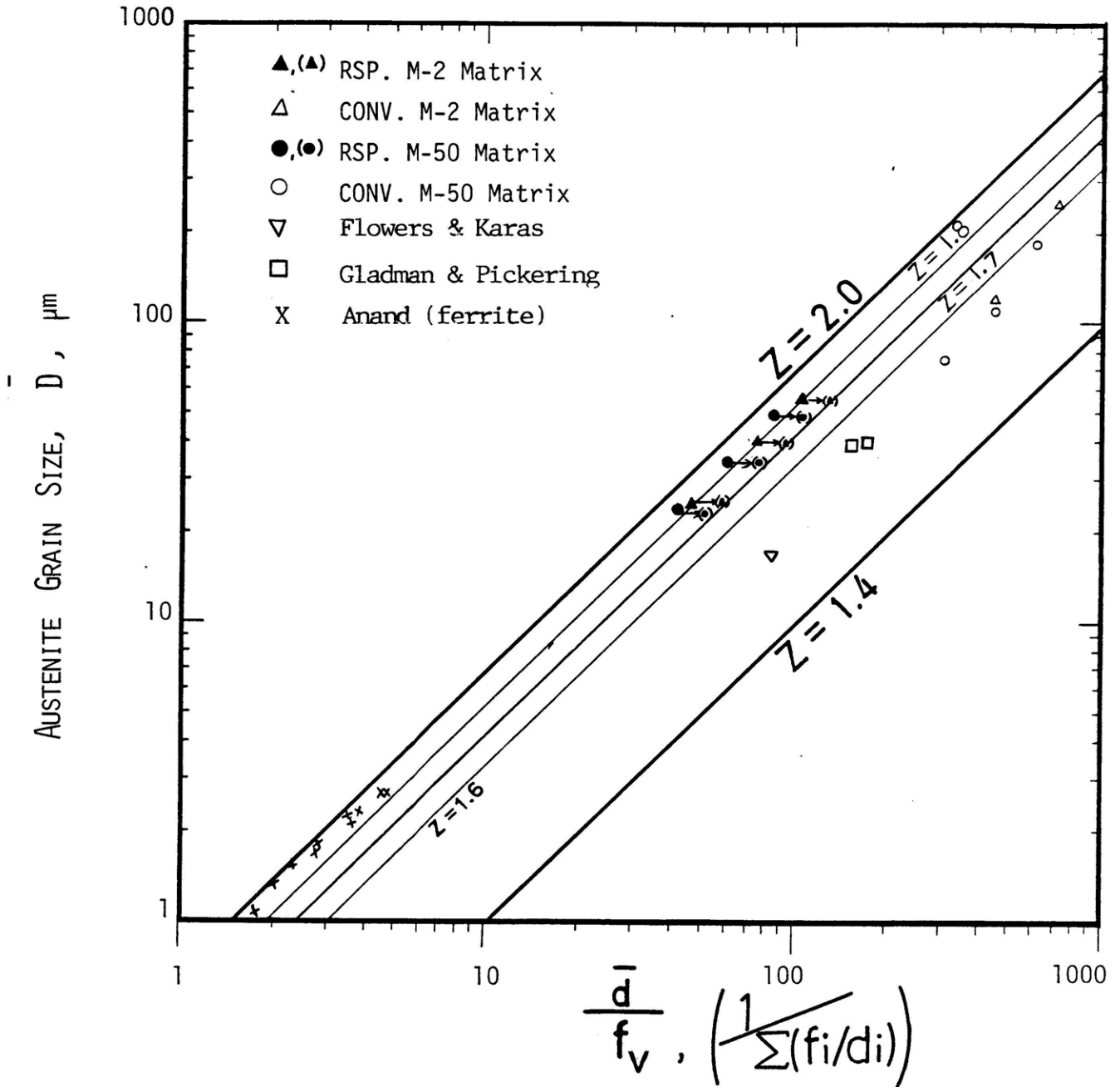


Figure 41. Comparison of Proposed Model and Experimental Results, Arrows Indicate the Change of the Ratio of \bar{d} / f_v When Equation (34) is Applied.

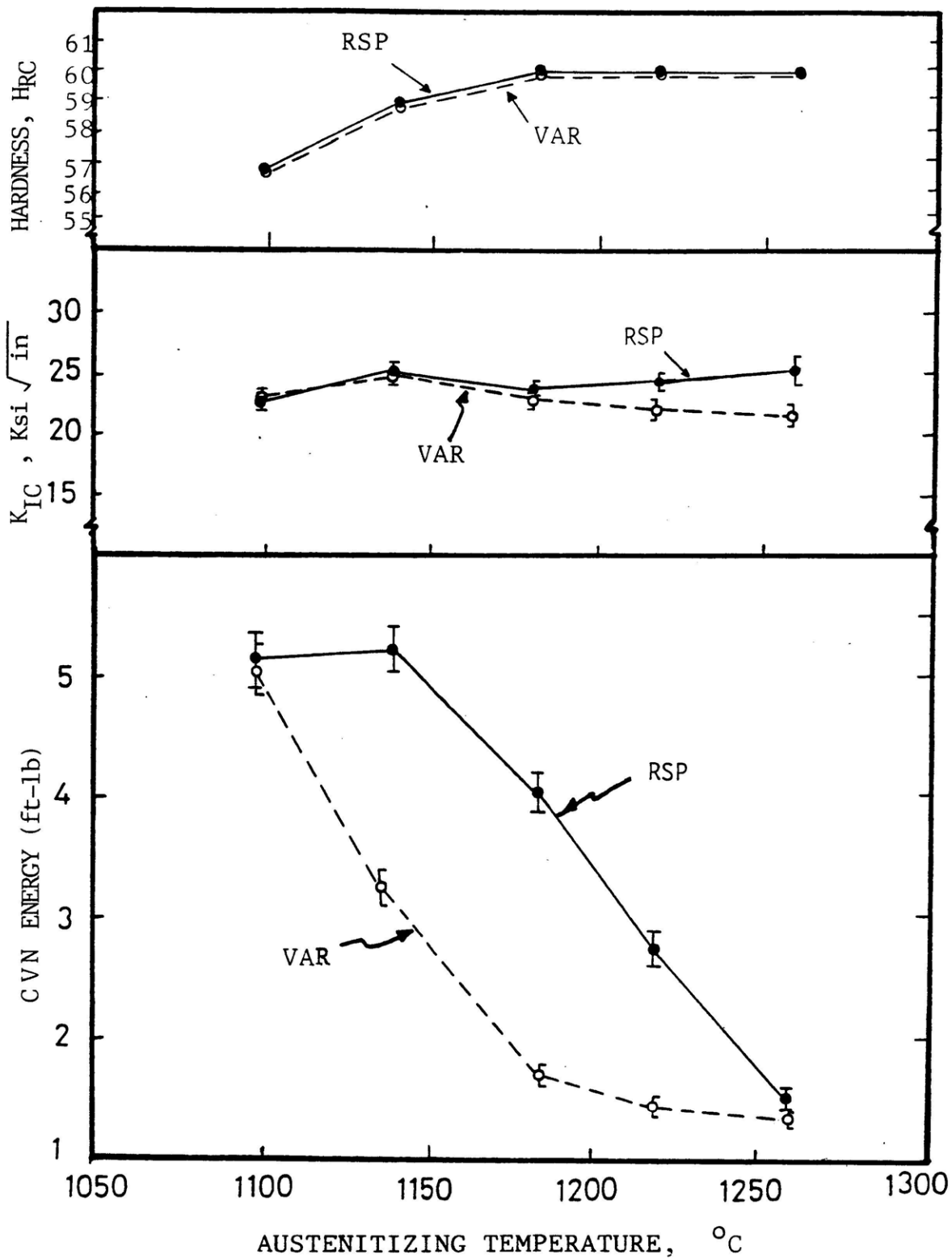


Figure 42. Comparison of Mechanical Properties of VAR and RSP M-2 Matrix Steels After One-Hour Austenitizing and Double Tempering at 565°C for 2+2 Hours.

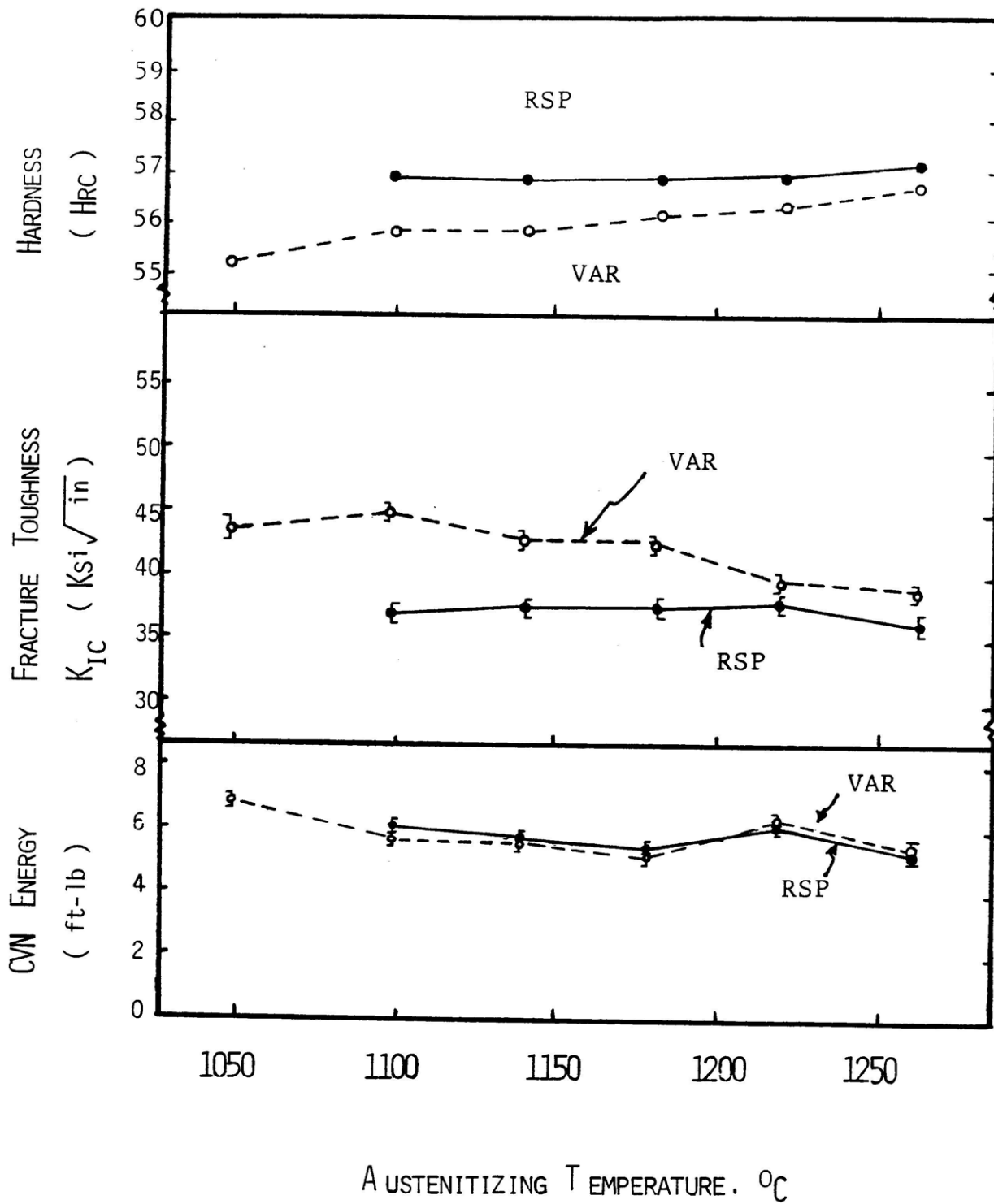


Figure 43 : Comparison of Mechanical Properties of VAR M-50 Matrix and RSP M-50 Matrix Steels after One-hour Austenitizing and Triple Tempering at 540°C for 2+2+2 hrs.

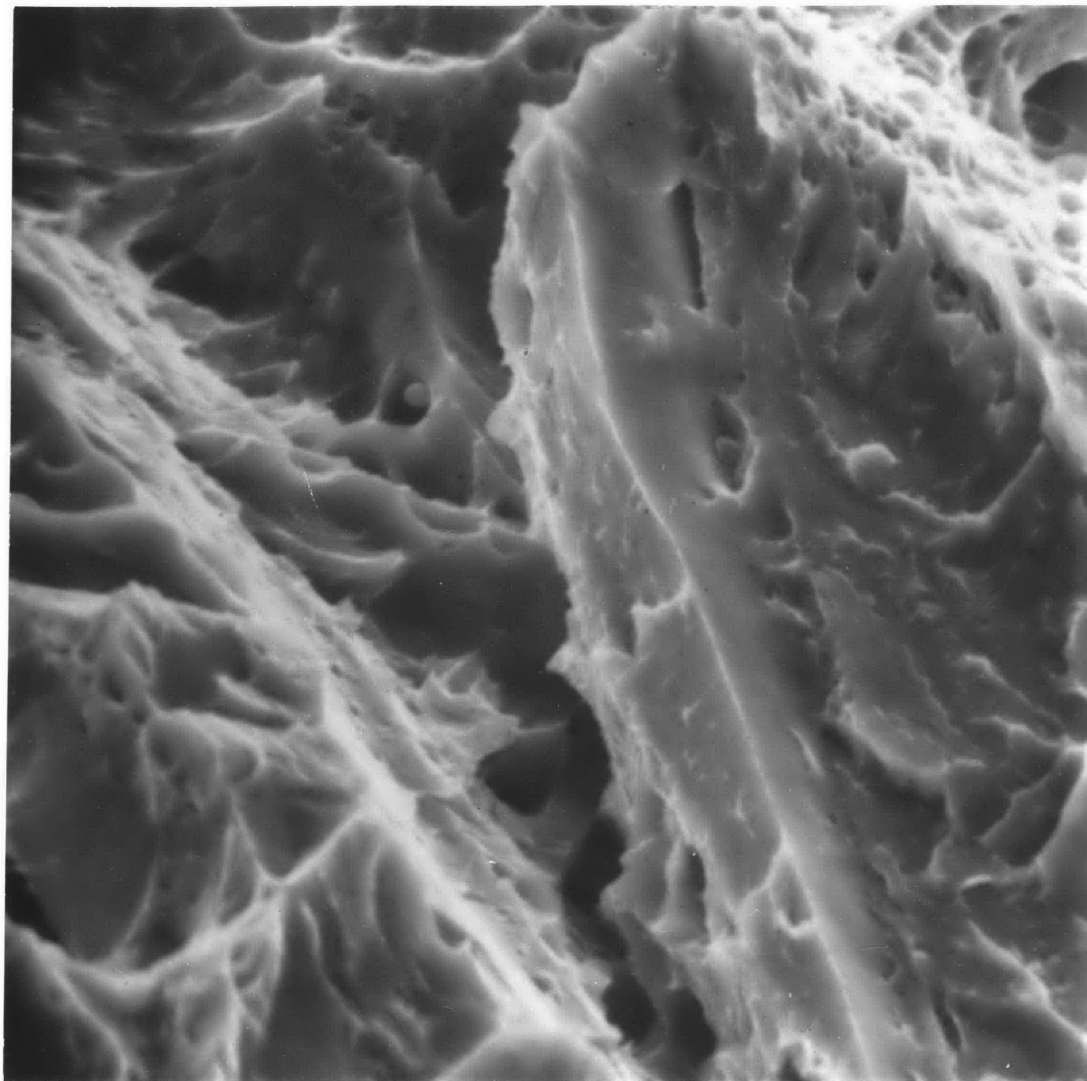


Figure 44. Fractograph of the VAR M-50 Matrix Steel, Austenitized at 1100°C for One Hour and then Triple Tempered at 540°C for 2+2+2 Hours.

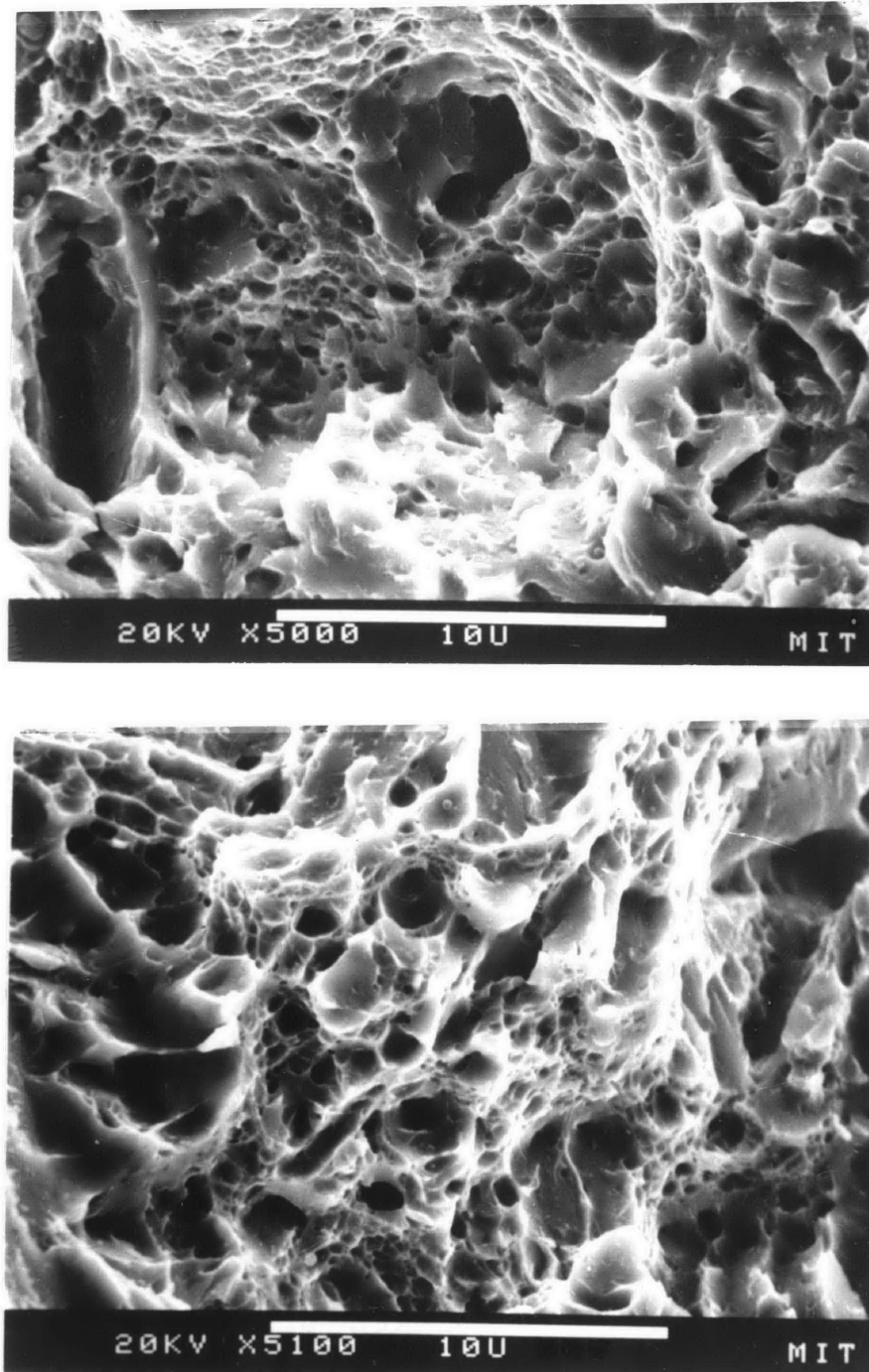


Figure 45. Fractograph of the RSP M-50 Matrix Steel (After HIPping at $1100^{\circ}\text{C}/3\text{hrs}$, 30Ksi), Austenitized at 1100°C for One Hour and then Triple Tempered at 540°C for 2+2+2 Hours.

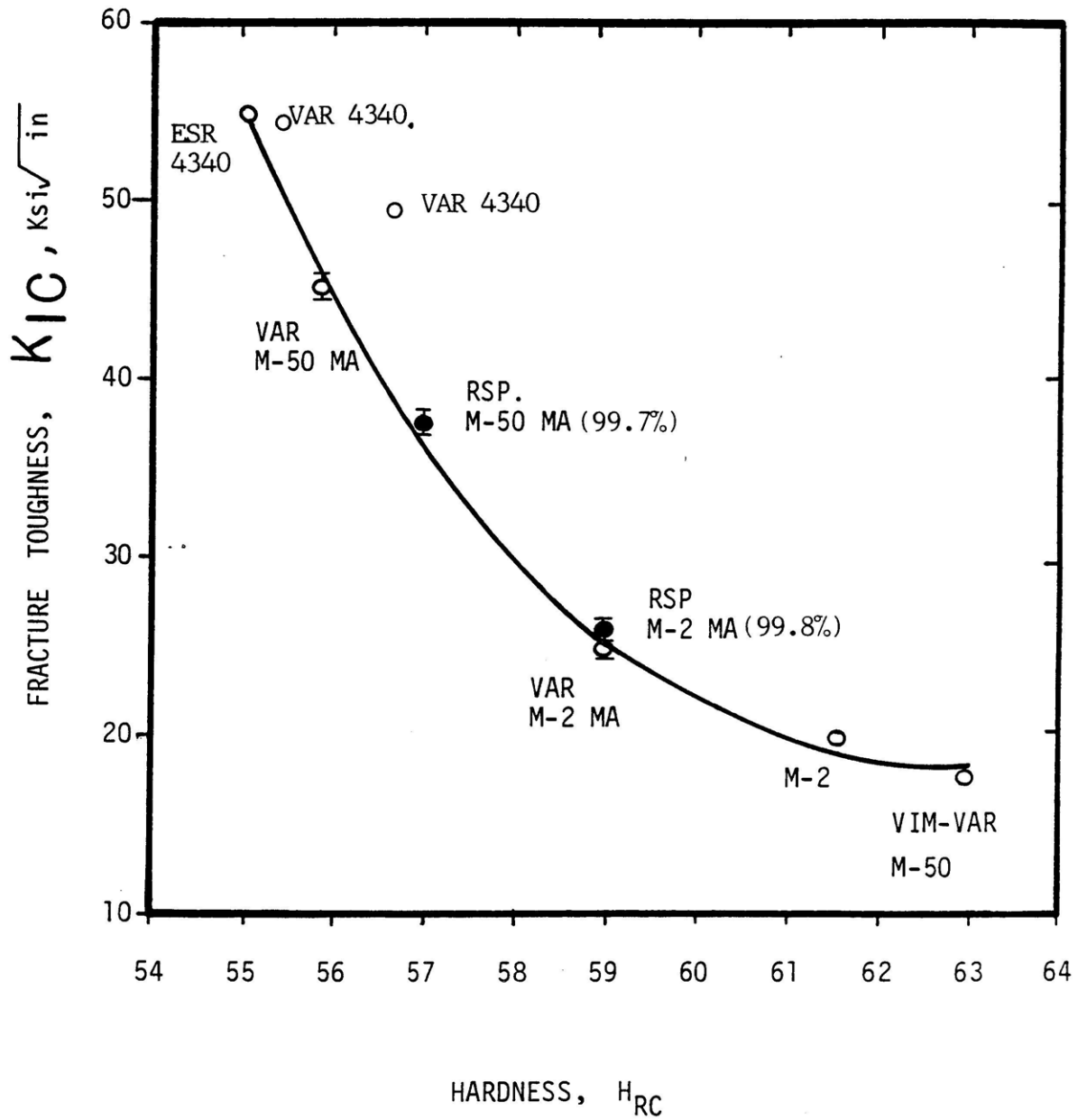


Figure 46: K_{IC} Sharp-Crack Fracture Toughness vs. Hardness in the Tempered Martensitic Steels.

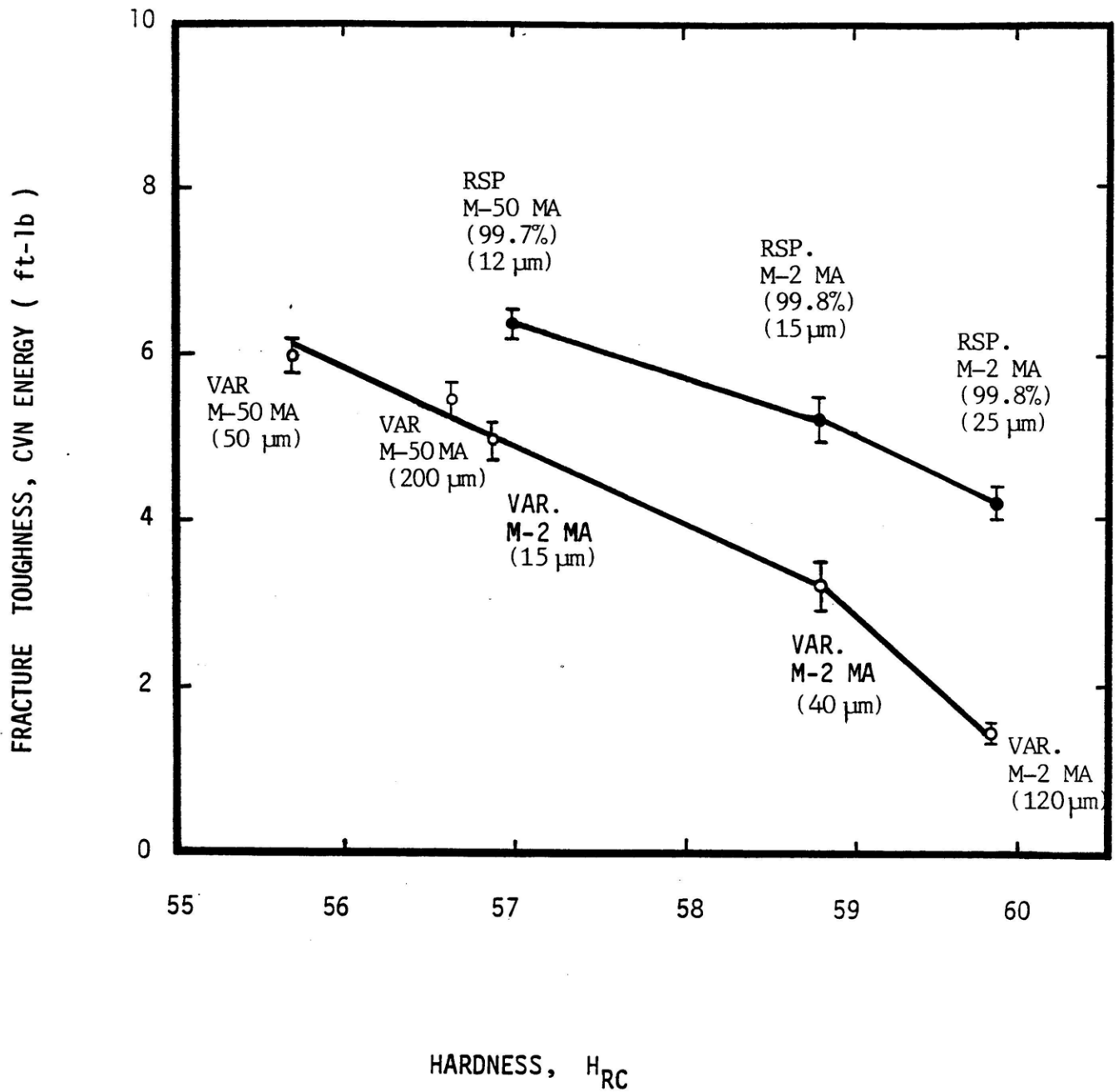


Figure 47. Comparison of Blunt-notch Fracture Toughness (CVN Energy) vs. Hardness for VAR and RSP Matrix Steels.

7. SUGGESTIONS FOR FUTURE WORK

- (1) The nominal compositions of the second-phase particles were identified based on the qualitative analysis of their energy-dispersive x-ray spectra. Further work on the quantitative chemical analysis and x-ray microdiffraction should permit determination of the exact compound (formula) of the second-phase particles in the RSP matrix steels.
- (2) RSP can achieve a low ratio of \bar{d} / f_v even for a small volume fraction of second-phase particles. High-melting second-phase particles with low solubility in the matrix phase can maintain the benefit of RSP. Application of the most potential grain-growth inhibitors, such as rare-earth sulfides (Ces, Las, Lus) to the RSP steels deserves considerable exploration, but care must be taken in the melting process.
- (3) The triggering of abnormal grain growth is not simply controlled by the grain-coarsening temperature, but is rather a complex function of temperature, \bar{d} , f_v , particle coarsening, spacial distribution of particles, and initial microstructure. The understanding of the onset of abnormal grain growth deserves further investigation.

- (4) The optimal processing conditions for rapid solidification processing should be investigated starting from atomization to the hot consolidation in order to obtain fully dense RSP alloys. Higher-consolidation temperatures should be explored in this connection.
- (5) Nitrogen atomization may reduce the extent of undesirable thermally-induced porosity, but it may raise another problem because of the solubility of nitrogen in steel. An alternative approach to accomplish RSP powder is suggested here. Alloys can be rapidly solidified by melt spinning to achieve a higher cooling rate of 10^6 K/sec (and a much more uniform quench rate in ribbons). The brittle thin ribbon can be pulverized into powder particles by hammer mills. The powder particles may likely form as platelet shapes which could provide improved flowability in the consolidation step.
- (6) Prior annealing treatments appear to influence the subsequent grain growth characteristics of RSP matrix steels, and should be studied in more detail.
- (7) Fine oxide particles present in the RSP matrix steel may form by precipitation during rapid solidification and/or by oxidation during the subsequent hot-consolidation processing of RSP powders. Application of STEM microanalysis to the as-solidified RSP powders can clarify the origin of these oxides.

BIOGRAPHICAL NOTE

The author was born on June 27, 1951 in Taiwan, Republic of China and raised in its traditionally cultured environment. When he finished his 9th grade course, he was admitted to a special five-year program in the Department of Metallurgical Engineering at National Taipei Institute of Technology in 1967. Immediately upon his graduation in 1972, he successfully won the nation-wide examination of professional degree in Metallurgical Engineering, sponsored by the Ministry of Examination of the Republic Of China.

From 1972 to 1974, he served as Reserved Engineering official in the military and ranked as lieutenant when he retired. Later, he joined an Engineering Consultant Corp. and worked as professional engineer in the field of Foundry for two years. In 1976, he went back to his college and was appointed as technical instructor of metallography and materials testing.

He came to United States in 1978 for graduate studies and received an M.S. degree in Metallurgy with highest honors from New Mexico Institute of Mining and Technology in 1980. He crossed country to the Massachusetts Institute of Technology, Cambridge, Massachusetts to begin his doctoral program in the Department of Materials Science and Engineering. He was married to Joyce M.C. Chen prior to the completion of his Ph.D. work here.